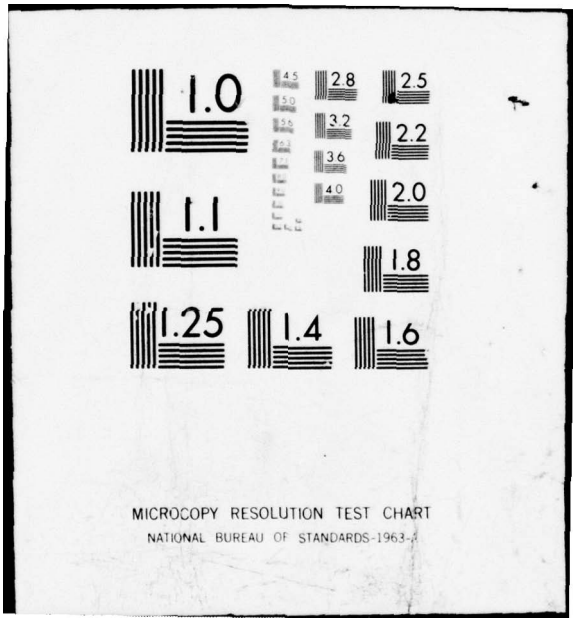
AD-A038 471 MISSOURI UNIV-COLUMBIA RESEARCH REACTOR FACILITY F/G 20/12
SILICON DETECTOR COMPENSATION BY NUCLEAR TRANSMUTATION.(U)
FEB 77 J M MEESE F33615-76-C-5230
UNCLASSIFIED NL




1.0
1.1
1.25
1.4
1.6
1.8
2.0
2.2
2.5
2.8
3.2
3.6
4.0
4.5
5.0
MICROCOPY RESOLUTION TEST CHART
NATIONAL BUREAU OF STANDARDS-1963-A

AD A038471

UNIVERSITY OF MISSOURI

SILICON DETECTOR COMPENSATION BY NUCLEAR TRANSMUTATION

UNIVERSITY OF MISSOURI
RESEARCH REACTOR FACILITY (MURR)
COLUMBIA, MISSOURI 65201

(11) FEB 77

(12) 108 p.

(9) INTERIM TECHNICAL REPORT, 30 JUN 76 - 31 DEC

(15) CONTRACT NO. F33615-76-C-5230

(16) PROJECT NO. 7371

AIR FORCE MATERIALS LABORATORY
AIR FORCE SYSTEMS COMMAND
UNITED STATES AIR FORCE
WRIGHT-PATTERSON AFB, OHIO 45433

PROJECT ENGINEER: DR. ROBERT J. SPRY
PRINCIPAL INVESTIGATOR: J. M. MEESE

(10)

AD NO.
DDC FILE COPY

440149

DISTRIBUTION STATEMENT A
Approved for public release;
Distribution Unlimited

DDC
APR 1

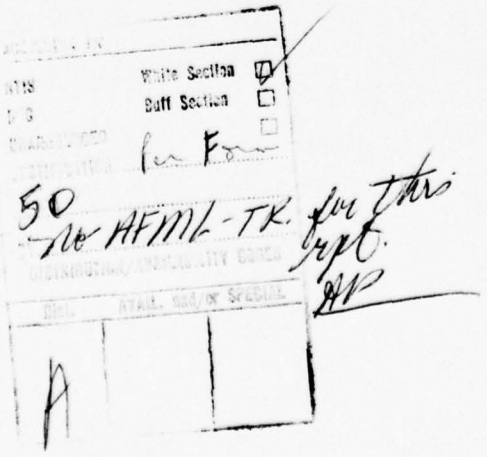
RESEARCH

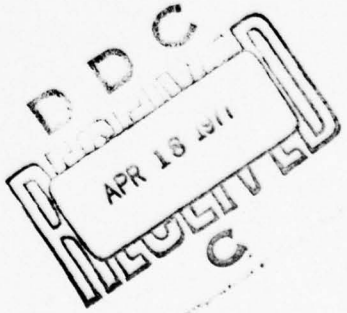
410149

Missouri Univ-Columbia Research Reactor
Facility.

TABLE OF CONTENTS

		Page
I.	INTRODUCTION	1
II.	THEORETICAL ANALYSIS	3
III.	EXPERIMENTAL TECHNIQUES AND APPARATUS	19
	A. Reactor Description	19
	B. Bulk Pool Variable Flux Irradiation Facility	24
	C. Neutron Flux Detection and Integration System	28
	D. Neutron Activation Analysis Systems	30
	E. Four-point and Thermal Probes	31
	F. Minority Carrier Lifetime Apparatus	37
	G. High Impedance Van der Pauw and Resistivity System (Electronics, Vacuum System, Helitran)	42
	H. Photoconductivity System	47
	I. Miscellaneuous: Sample Preparation Equipment, Annealing System, Irradiation of Silicon, Post-Irradiation Handling	48
IV.	EXPERIMENTAL RESULTS AND DISCUSSION	49
	A. Materials Evaluation Before Irradiation	50
	B. Neutron Activation Analysis	62
	C. Irradiation and Annealing Experiments	67
V.	PROGRESS AND ACCOMPLISHMENTS	98
	REFERENCES	101





DISTRIBUTION STATEMENT A
Approved for public release;
Distribution Unlimited

LIST OF TABLES

Table		Page
1	Nuclear Data	3
2	^{31}P - Theoretical Production Rates	4
3	Typical Experimental Mobility Values in Si	5
4	Integrator System Calibration Data	28
5	A Comparison of Four-point Probe Resistivity Measurements Made at Rockwell and MURR	35
6	Summary of Undoped Sample Characterization Before Irradiation	51
7	Summary of Minority Carrier Lifetimes	53
8	Summary of Drift Mobilities	55
9	Summary of Analytical Conditions and Detection Limits for Neutron Activation Analysis of Silicon	64
10	Elemental Concentrations Measured in Four Silicon Ingots	65
11	Number of Displacements per Phosphorus Produced	72
12	Summary of Irradiations	74
13	Summary of Prominent Annealing Features	97

LIST OF ILLUSTRATIONS

Figure		Page
1	Resistivity and carrier concentration vs. fluence	11
2	Expanded fluence scale plot of Figure 1	12
3	Resistivity vs. fluence	15
4	Hall mobility vs. fluence	16
5	Hall coefficient vs. fluence	17
6	Actual carrier coefficient p, n, and Hall coefficient carrier concentration p_H, n_H, vs. fluence	18
7	Comparison of research reactor peak flux values in the United States	20
8	Flux trap, beamports, reflector and bulkpool facilities . . .	21
9	Thermal neutron flux profile in I-2 reflector position. . . .	22
10	Movable box detail for bulk pool irradiation facility	25
11	Support rods for variable flux facility	26
12	Detector holder for variable flux facility	27
13	Current vs. voltage for four point probe. . . . . resistivity measurement (top of VZ-072-#5	33
14	Current vs. voltage for bottom of VZ-072-#5	34
15	Typical photoconductive decay curves for determining minority carrier lifetime	38
16	Minority carrier lifetime measurement apparatus	40
17	Exponential decay generator	41
18	Switching circuit for resistivity and Hall effect measurements	43
19	Analog voltage amplifier and current source for digital Gauss-meter	44
20	Analog to digital converter circuitry for digital Gaussmeter	45
21	Axial resistivity and axial lifetime of ingot VZ-072.	54
22	Radial resistivity of VZ-072-1-top	56
23	Radial resistivity of VZ-072-2-top	57

LIST OF ILLUSTRATIONS (CONT.)

Figure		Page
24	Radial resistivity of VZ-072-3-top	58
25	Radial resistivity of VZ-073-4-top	59
26	Radial resistivity of VZ-072-5-top	60
27	Radial resistivity of VZ-072-5-bottom	61
28	Concentration of gold vs percent of sample weight removed . .	66
29	A comparison of isochronal annealing of transmutation doped float zone and Czochralski silicon	76
30	Isochronal annealing of two float zone samples irradiated to produce $\sim$ 100 Ω-cm n-type	79
31	Semilog plot of the log of the reciprocal of the fraction of phosphorus not electrically active vs. reciprocal annealing temperature for the Topsil sample shown in Figure 30.	81
32	Isochronal annealing of resistivity and minority carrier lifetime of Rockwell float zone (argon anneal) bulk sample. .	84
33	Argon isochronal anneal of resistivity of Rockwell float zone wafer.	85
34	Argon isochronal anneal of Topsil wafer	86
35	Argon isochronal anneal of T.I. Lopex wafer	87
36	Vacuum isochronal anneal of Wacker wafer.	88
37	Vacuum isochronal anneal of T.I. Lopex wafer.	89
38	Vacuum isochronal anneal of Rockwell wafer.	90
39	Vacuum isochronal anneal of Topsil wafer	91
40	Comparison of vacuum and argon isochronal anneals for Topsil wafers	92
41	Comparison of vacuum and argon isochronal anneals for T.I. Lopex wafers.	93
42	Argon isochronal anneal of Topsil wafer irradiated to $\Phi = 1.02 \Phi_c$.	95

PREFACE

This interim report describes work performed by personnel of the University of Missouri Research Reactor Facility, Columbia, Missouri 65201 during the period from 30 June 1976 to 31 December 1976, under Contract F33615-76-C-5230, Project 7371. The program was monitored by Dr. Robert J. Spry, Air Force Materials Laboratory, Air Force Systems Command, Wright-Patterson Air Force Base, Ohio.

The program was directed toward the compensation of residual boron in infrared detector grade silicon by nuclear transmutation doping. This investigation was conducted by Dr. J. M. Meese, principal investigator, Dr. D. M. Alger, Mr. S. L. Gunn, Mr. W. F. Richardson, Mr. P. J. Glairon, Dr. D. M. McKown, and Dr. J. Steven Morris.

I. INTRODUCTION

The primary objective of this program is to devise, through the research to be discussed, an optimum set of techniques capable of compensating the residual boron always found in detector grade silicon by the process of nuclear transmutation doping. The material to be developed by this program is intended for use in infrared detector systems such as those of the Air Force LADIR (Low Cost Arrays for the Detection of Infrared) program.

The best silicon available today contains residual boron, a shallow acceptor, in concentrations of the order of 10^{12} B/cm^3. This is because the segregation coefficient of this impurity is close to unity and, therefore, will not be substantually removed by successive passes in a zone refiner. This residual boron concentration has several adverse effects on the operation of extrinsic photoconductor IR detectors fabricated from Ga or In doped silicon. Since the B ionization energy is less than those of Ga or In, the B levels thermally ionize at temperatures below those impurities of interest forcing the detectivity out of the background limited condition at prematurely low temperatures. This effect requires these detectors to be cooled by liquid helium rather than by a helium gas closed cycle refrigerator. As a result, system size and cost increase unless these boron levels can be populated by carriers from compensating donor levels. Furthermore, the shallow boron optical transition is beyond the atmospheric transmission windows through which the IR data information is obtained. Therefore, these boron optical transitions can respond to undesirable background thermal radiation to produce a type of nonuseful background noise.

Both of these problems can be eliminated with a minimum degradation in theoretical detector gain if nearly exact compensation of the boron acceptors is accomplished by the addition of shallow donors. Greatly overcompensating the boron, however, is undersirable because the additional donor carriers fill the Ga or In levels once all the B levels are compensated. This reduces detector gain by reducing the number of desirable optical transitions from which signal information is gained. Additionally, the extra impurities from over-compensation represent additional charged impurity scattering centers reducing the carrier mobility which is dominated by charged impurity scattering at the low temperatures at which these detectors operate. This lowering of carrier mobility reduces the gain of the detector which is proportional to the product

of mobility times lifetime.

Nuclear transmutation doping of silicon appears to offer several advantages over conventional doping techniques for producing the desired compensating donor concentration. Briefly, the transmutation doping process is based on the conversion of the isotope ^{30}Si to ^{31}Si through an (n, γ) reaction induced by thermal neutron capture during reactor irradiation. The ^{31}Si isotope is unstable and decays through β^- emission to ^{31}P, the desired donor impurity. Since the production rate of ^{31}P is 3.355 ppb/10^{18} n/cm^2, the production of donors is slow enough to provide careful control of the dopant concentration. Furthermore, the donors added by transmutation doping are distributed uniformally throughout the lattice because the microscopic abundance ratios of the Si isotopes are uniform and the thermal neutron diffusion length is very long compared to typical ingot dimensions.

The two major advantages of NTD-Si, tight control over doping concentration and uniformity of dopant distribution, are somewhat offset by the radiation damage effects which occur during irradiation. These effects cause no difficulty for float zone Si neutron doped to a resistivity of 100 Ω-cm or lower. For higher final resistivity material, the success or failure depends intimately on residual impurity defect interactions and their annealing properties. One of the major goals of the present research is to define the limits over final resistivity which can be achieved relative to the properties of the starting material.

The balance of this report is contained in five major sections as follows:

- Section II develops the theoretical tools to understand the expected electrical properties resulting from transmutation doped Si as a function of neutron fluence. A discussion of the transmutation doping process is also presented.
- Section III is a description of the experimental techniques and apparatus employed throughout this work.
- Section IV gives a discription of the experimental results and a discussion of possible interpretations.
- Section V discusses the significant accomplishments achieved during the program and discusses areas of difficulty where further research will be required.

II. THEORETICAL ANALYSIS

The basic physics of transmutation doping in Si has been discussed by Tanenbaum and Mills.[1] Although they discuss all possible nuclear reactions with all the silicon and oxygen isotopes such as (n, γ), (n, 2n), (n, p), and (n, α), we will confine our attention to the (n, γ) reactions with Si as being the only significant reactions in a thermal neutron flux. This viewpoint has been verified experimentally.[1]

The natural abundance, thermal neutron absorption cross section (n, γ) and half-lifes of the relevant isotopes of silicon and phosphorus are listed in Table 1.

TABLE 1. NUCLEAR DATA

Natural Abundance	Isotope	σ(n, γ)	$T_{1/2}$
92.27%	^{28}Si	0.08 $\pm$ 0.03 b	stable
4.68%	^{29}Si	0.28 $\pm$ 0.09 b	stable
3.05%	^{30}Si	0.11 $\pm$ 0.01 b	2.62h
100%	^{31}P	0.20 $\pm$ 0.02 b	14.3d
At. Wgt. Si = 28.086, N(Si) = 5×10^{22} atoms/cm^3			
Density Si = 2.33 gm/cm^3			

The nuclear reactions of interest are the following:

$$^{28}\text{Si}\ (n, \gamma)\ ^{29}\text{Si} \qquad (1)$$

$$^{29}\text{Si}\ (n, \gamma)\ ^{30}\text{Si} \qquad (2)$$

$$^{30}\text{Si}\ (n, \gamma)\ ^{31}\text{Si} \longrightarrow {}^{31}\text{P} + \beta^- \qquad (3)$$

$$T_{1/2} = 2.62\text{h}$$

$$^{31}\text{P}\ (n, \gamma)\ ^{32}\text{P} \longrightarrow {}^{32}\text{S} + \beta^- \qquad (4)$$

$$T_{1/2} = 14.3\text{d}$$

The first two reactions redistribute the natural abundance of the silicon isotopes but do not lead to any doping effects or radioactivity. Reaction (2)

is quite fortunate in that it serves to replace the ^{30}Si isotope approximately as it is burned up in reaction (3) which produces the dopant ^{31}P. Reaction (4) transmutes the stable isotope ^{31}P to the unstable isotope ^{32}P which β^- decays to ^{32}S. Since reaction (4) is a second order effect, the doping is thought to be negligible compared to the doping from ^{31}P (see Ref. 1). This reaction is important, however, as the primary source of radioactivity for times which are long compared to the half-life of reaction (3).

From the data given in Table 1, we can calculate the production rate of the desired dopant. The total number of Si atoms/cm^3 is found to be

$$N(Si) = \frac{2.33\ (6.023 \times 10^{22})}{28.086} = 4.996 \times 10^{22}\ \text{atoms/cm}^3.$$

The density of ^{30}Si isotopes is then found to be

$$N(^{30}Si) = 0.0305\ N(Si) = 1.524 \times 10^{21}\ \text{atoms/cm}^3.$$

The theoretical production rate for phosphorus is then found from the expression

$$\frac{d[^{31}P]}{d\Phi} = N(^{30}Si)\ \sigma[^{30}Si\ (n, \gamma)\ ^{31}Si]$$

$$= 1.676 \times 10^{-4}\ \ ^{31}P\ \text{atoms/cm}^3/\text{n/cm}^2$$

where Φ is the irradiation fluence of thermal neutrons (n/cm^2). Table 2 lists the theoretical production of donors in Si in several useful sets of units.

TABLE 2. ^{31}P THEORETICAL PRODUCTION RATES

Production Rate (K)	Units
1.676×10^{-4}	P atoms/cm^3 per n/cm^2
1.676×10^{14}	P atoms/cm^3 per 10^{18} n/cm^2
3.355	ppb per 10^{18} n/cm^2

Knowing the concentration of donors added per unit fluence, it is now possible to calculate the final resistivity after irradiation and annealing from the starting resistivity if the mobility of the majority carrier is known. To this end an analysis of mobility data for Si has been performed on data taken

from two review papers.[2,3] Since these authors quote the same references but give different values, we have averaged when this has occurred. We have also discarded three values which differed abnormally from the mean, $\mu_{Hn} = 1345$, $\mu_{Dn} = 1590$ and $\mu_{Dp} = 356$ cm^2/V-sec.

The result of the average of all other data is summarized in Table 3.

TABLE 3. TYPICAL EXPERIMENTAL MOBILITY VALUES IN Si

$\mu_{Dp} = (494 \pm 11)$ cm^2/V-sec
$\mu_{Dn} = (1396 \pm 64)$ cm^2/V-sec
$r_p = \mu_H/\mu_D = 0.77 \pm 0.06$
$r_n = 1.3 \pm 0.1$
$b = \mu_n/\mu_p = 2.826$
$p = \dfrac{[e\mu_p]^{-1}}{\rho} = \dfrac{(1.265 \pm 0.29) \times 10^{16}\ \text{cm}^{-3}}{\rho} = \dfrac{(253 \pm 5.7)\ \text{ppb}}{\rho}$
$n = \dfrac{[e\mu_n]^{-1}}{\rho} = \dfrac{(4.477 \pm 0.197) \times 10^{15}\ \text{cm}^{-3}}{\rho} = \dfrac{(89.54 \pm 3.94)\ \text{ppb}}{\rho}$

These expressions will be useful expressions for estimating the ppb added by neutron irradiation in the sections to follow.

If the initial and final carrier concentrations are large at room temperature compared to the number of intrinsic carriers, then the following expressions for the carrier densities in terms of donor and acceptor concentrations are

$$p_o = N_A - N_{D_o}, \qquad \text{p-type starting material}$$

$$n_o = N_{D_o} - N_A, \qquad \text{n-type starting material}$$

$$p_f = N_A - N_{D_f}, \qquad \text{p-type ending material}$$

$$n_f = N_{D_f} - N_A, \qquad \text{n-type ending material}$$

then,

$$n_f - n_o = N_{D_f} - N_{D_o}, \qquad \text{n-type to n-type}$$

$$n_f + p_o = N_{D_f} - N_{D_o}, \qquad \text{p-type to n-type}$$

$$p_o - p_f = N_{D_f} - N_{D_o}, \qquad \text{p-type to p-type.}$$

But $N_{D_f} - N_{D_o}$ is just the concentration of donors added by transmutation which we will call $N_P = K\,\Phi$ where K is the production rate given in Table 2 and Φ is the fluence (number of neutrons /cm^2). Therefore, we see that in all cases for which n_i can be neglected, the concentration of phosphorus added can be determined by the concentrations of uncompensated carriers and the material type.

We can determine the concentration, N_P, of phosphorus atoms added either from the fluence Φ or the initial and final resistivities and types using the following expressions,

$$N_P = K\,\Phi = 3.355 \times 10^{-18} \frac{\text{ppb}}{\text{n/cm}^2}\ \Phi \qquad (5)$$

$$N_p = \begin{cases} \dfrac{K_n}{\rho_{n_f}} - \dfrac{K_n}{\rho_{n_o}} & \text{n-type} \longrightarrow \text{n-type} \\ \dfrac{K_n}{\rho_{n_f}} + \dfrac{K_p}{\rho_{p_o}} & \text{p-type} \longrightarrow \text{n-type} \\ \dfrac{K_p}{\rho_{p_o}} - \dfrac{K_p}{\rho_{p_f}} & \text{p-type} \longrightarrow \text{p-type} \end{cases} \qquad (6)$$

where K_n = 89.54 ppb Ω-cm and K_p = 253 ppb Ω-cm. The conversion between ppb and atoms/cm^3 is 1 ppb = 5 x 10^{13} atoms/cm^3.

By equating the two expressions above, the fluence necessary to obtain a desired final resistivity can be determined from the initial resistivity and type as

$$\Phi = \begin{cases} \frac{K_n}{K}\left(\rho_{n_f}^{-1} - \rho_{n_o}^{-1}\right) & \text{n-type} \longrightarrow \text{n-type} \\ \frac{K_n}{K}\rho_{n_f}^{-1} + \frac{K_p}{K_3}\rho_{p_o}^{-1} & \text{p-type} \longrightarrow \text{n-type} \\ \frac{K_p}{K}\left(\rho_{p_o}^{-1} - \rho_{p_f}^{-1}\right) . & \text{p-type} \longrightarrow \text{p-type} \end{cases} \qquad (7)$$

The resistivity after irradiation and annealing as a function of fluence can also be calculated for those cases where n_i is not negligible compared to the majority carrier concentration.

The resistivity vs fluence has been calculated for transmutation doped samples using the following assumptions:

1. 100% electrical activity is obtained by annealing.
2. The mobilities remain constant.
   (μ_n = 1500 cm^2/V-sec, μ_p = 600 cm^2/V-sec) in the following figures.
3. The shallow donors and acceptors are completely ionized at room temperature.
4. The production rate of phosphorus is given by K = 3.355 ppb/10^{18} n/cm^2, which is obtained from the cross-section.
5. The number of intrinsic carriers at room temperature is
   n_i = 1.391 x 10^{10} cm^{-3}.

From charge conservation, the complete ionization assumption, and the relation

$$np = n_i^2$$

we obtain

$$p = 1/2\left[N_A - N_D + \sqrt{(N_A - N_D)^2 + 4n_i^2}\right] .$$

For a production rate of donors given by K, this equation becomes for p-type material

$$p = 1/2\left[(N_A - N_D - K\phi) + \sqrt{(N_A - N_D - K\phi)^2 + 4\, n_i^2}\right] . \qquad (8)$$

If we define the degree of initial compensation k_o by the expression

$$k_o = \frac{N_D}{N_A},$$

then the degree of compensation as a function of fluence is given by

$$k = \frac{N_D + K\phi}{N_A} \quad .$$

For complete compensation, k = 1; for no compensation k = o. We define one more quantity, a, the degree of compensation remaining by

$$a = 1-k = \frac{N_A - N_D - K\phi}{N_A} \cong \frac{p}{N_A} \quad .$$

For no irradiation, we assume that $p_o >> n_i$ so that

$$a_o = 1-k_o = \frac{N_A - N_D}{N_A} = \frac{p_o}{N_A} \quad . \tag{9}$$

It can be shown by substitution in Eq. (1) that

$$p = \frac{N_A}{2} \left[a + \sqrt{a^2 + \left(\frac{2n_i}{N_A}\right)^2} \right] . \tag{10}$$

We now define the fluence necessary for complete compensation as ϕ_c. This is obtained when k = 1 or a = o and is obtained from Eq. (9)

$$o = 1 - 1 = \frac{N_A - N_D - K\phi_c}{N_A}$$

or

$$\phi_c = \frac{N_A - N_D}{K} = \frac{p_o}{K} \quad .$$

It can now be shown that

$$a = \left(1 - \frac{N_D}{N_A}\right)\left(1 - \frac{\phi}{\phi_c}\right)$$

$$= a_o\left(1 - \frac{\phi}{\phi_c}\right) \quad .$$

Then, from Eq. (10)

$$p = \frac{N_A a_o}{2} \left[\left(1 - \frac{\phi}{\phi_c}\right) + \sqrt{\left(1 - \frac{\phi}{\phi_c}\right)^2 + \left(\frac{2n_i}{N_A a_o}\right)^2} \right] .$$

But from Eq. (9) with ϕ = o,

$$N_A a_o = p_o$$

therefore, we obtain

$$p = \frac{p_o}{2}\left[\left(1 - \frac{\phi}{\phi_c}\right) + \sqrt{\left(1 - \frac{\phi}{\phi_c}\right)^2 + \left(\frac{2n_i}{p_o}\right)^2}\right]. \tag{11}$$

It can similarly be shown for overcompensation (n-type produced)

$$n = \frac{p_o}{2}\left[-\left(1 - \frac{\phi}{\phi_c}\right) + \sqrt{\left(1 - \frac{\phi}{\phi_c}\right)^2 + \left(\frac{2n_i}{p_o}\right)^2}\right]. \tag{12}$$

It should be noted that the number of carriers is symmetrical with respect to the fluence on either side of $\phi = \phi_c$. It should also be noted that the number of free carriers as a function of fluence is independent of the degree of compensation. It can be shown that Eqs. (11) and (12) form a universal doping curve since doubling the initial concentration doubles the normalized flux coordinate $(1 - \phi/\phi_c)$, i.e., if $p_o = 2\,p_o'$, then

$$p = \frac{p_o'}{2}\left[2\left(1 - \frac{\phi}{\phi_c}\right) + \sqrt{\left[2\left(1 - \frac{\phi}{\phi_c}\right)\right]^2 + \left(\frac{2n_i}{p_o}\right)^2}\right].$$

An expression for the resistivity as a function of fluence can be obtained from the expression

$$P = \frac{1}{e(n\mu_n + p\mu_p)}$$

$$b = \mu_n/\mu_p$$

and

$$np = n_i^2$$

therefore,

$$\rho = \begin{cases} \dfrac{p}{e\mu_p\,(bn_i^2 + p^2)} & \text{p-type} \\[2ex] \dfrac{n}{e\mu_p(bn^2 + n_i^2)} & \text{n-type} \end{cases}. \tag{13}$$

By substituting n or p as a function of fluence from Eqs. (11) and (12) the resistivity, ρ, can be obtained as a function of fluence. This expression is plotted in Figures (1) and (2) for typical p-type float zone material (the parameters are given on the figures).

The sensitivity of resistivity to fluence should be noted near complete compensation. Furthermore, in the expanded scale in Figure 2, note that the maximum resistivity occurs at a fluence below that necessary for 100% compensation. This is a result of the fact that the carrier mobilities are not equal.

By differentiation of Eq. (13), it can be shown that

$$\rho_m = \frac{1}{2en_i\sqrt{\mu_n\mu_p}} \tag{14}$$

where

ρ_m is the highest resistivity obtainable.

It can similarly be shown that the fluence, ϕ_m, to obtain maximum resistivity, is related to the critical fluence to obtain 100% compensation by the expression

$$\phi_c - \phi_m = \frac{\left(\frac{\mu_n}{\mu_p} - 1\right)}{\sqrt{\frac{\mu_n}{\mu_p}}} \frac{n_i}{K} \tag{15}$$

which depends only on material parameters n_i, the mobility ratio, and the phosphorus production rate K. This difference, therefore, represents a universal constant for a particular type of material. It is interesting to note that since n_i and K can be measured independently, an experiment to generate Figure 2 gives a new technique for measuring the drift mobility ratios independent of any direct mobility measurement.

This model can be extended to include mixed conduction effects due to compensation on the Hall factor, R_H, the Hall mobility, μ_H, and the apparent number of free carriers, $\pm 1/R_H e$.

From equations (11) and (12), we found that

$$\begin{Bmatrix} p \\ n \end{Bmatrix} = \frac{p_o}{2}\left[\pm\left(1 - \frac{\phi}{\phi_c}\right) + \sqrt{\left(1 - \frac{\phi}{\phi_c}\right)^2 + \left(\frac{2n_i}{p_o}\right)^2}\right] \tag{16}$$

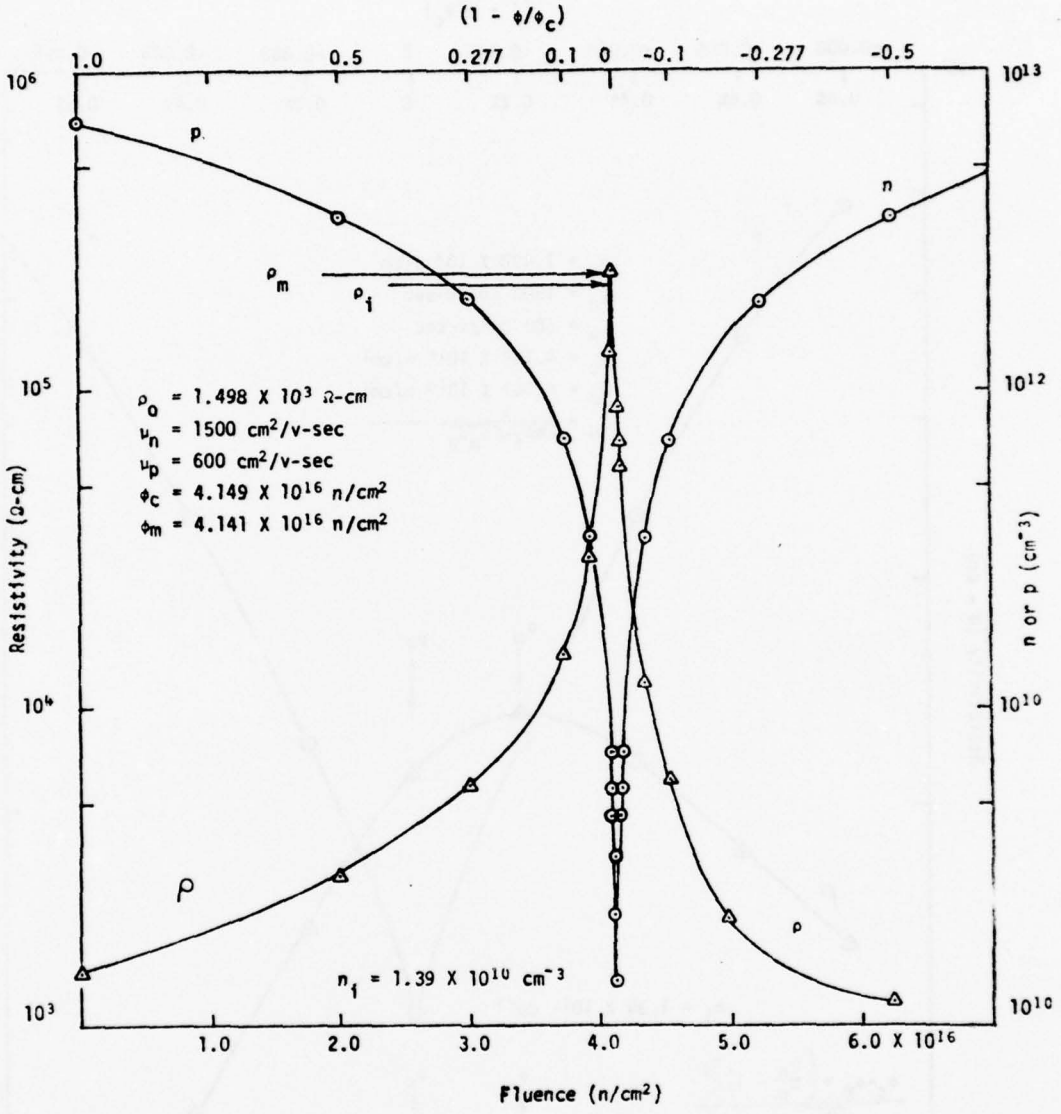


Figure 1. Resistivity and carrier concentration vs. fluence.

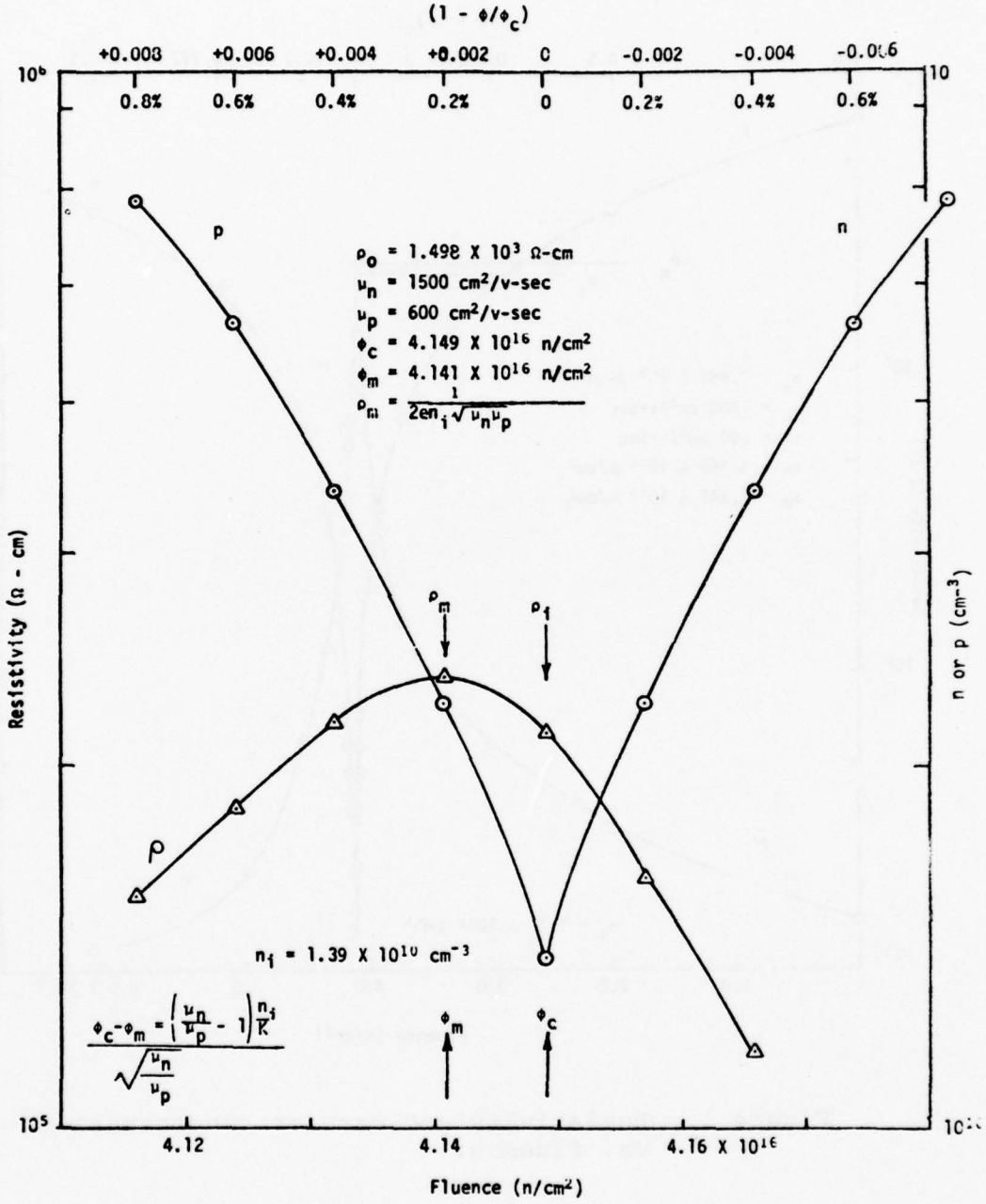


Figure 2. Expanded fluence scale plot of Figure 1.

where (+) is for p>n and (-) is for n>p. This equation represents the actual number of carriers as a function of fluence, ϕ, and the critical fluence, ϕ_c, required for exact compensation.

Because of mixed conduction effects near exact compensation, the Hall coefficient, R_H is suppressed. A simple extension of conventional theory[4] after using the relation $np = n_i^2$ gives

$$R_H = \begin{cases} \dfrac{p(p^2 - n_i^2 b^2)}{e\,(p^2 + n_i^2 b)^2} & , p>n \\ \dfrac{n(n_i^2 - n^2 b^2)}{e(n_i^2 + n^2 b)^2} & , n>p \end{cases} \qquad (17)$$

where $b = \mu_n/\mu_p$ is the ratio of drift mobilities. Using the usual relation between Hall mobility and R_H,

$$\mu_H = \pm \frac{R_H}{\rho} \qquad \begin{cases} (+)\ R_H>o \\ (-)\ R_H<o \end{cases}$$

and equation (13)

$$\rho = \begin{cases} \dfrac{p}{e\mu_p(bn_i^2 + p^2)} & \text{for } R_H>o \\ \dfrac{n}{e\mu_p(bn^2 + n_i^2)} = \dfrac{bn}{\mu_n e(bn^2 + n_i^2)} & \text{for } R_H<o \end{cases}$$

we obtain

$$\mu_H = \begin{cases} \dfrac{\mu_p(p^2 - n_i^2 b^2)}{(p^2 + n_i^2 b)} & \text{for } R_H>o \\ \dfrac{\mu_n(n^2 b^2 - n_i^2)}{b(n^2 b + n_i^2)} & \text{and for } R_H<o \end{cases} \qquad (18)$$

Note that near complete compensation, the Hall mobility is considerably suppressed as $p \to n_i b$ or $n \to n_i/b$.

The apparent free carrier concentration obtained from the Hall coefficient

is, near compensation, larger than the actual carrier concentration since

$$p_H = \frac{1}{R_H e} = \frac{(p^2 + n_i^2 b)^2}{p(p^2 - n_i^2 b^2)} \qquad (19)$$

$$n_H = -\frac{1}{R_H e} = \frac{(n^2 b + n_i^2)^2}{n(n^2 b^2 - n_i^2)} \quad .$$

These equations are now in a form from which μ_H, R_H, and n_H or p_H can be obtained as a function of fluence by direct substitution of Eq. (16) into Eqs. (17), (18), and (19). Programs have been written to generate these variables as a function of fluence. Data calculated from the code is shown for a typical case in Figures (3), (4), (5), and (6).

Note that as $p \to n_i b$; $R_H \to o$, $\mu_H \to o$, $p_H \to \infty$. This is not the same condition as obtained for the resistivity which reaches a maximum at $p = b^{\frac{1}{2}} n_i$.

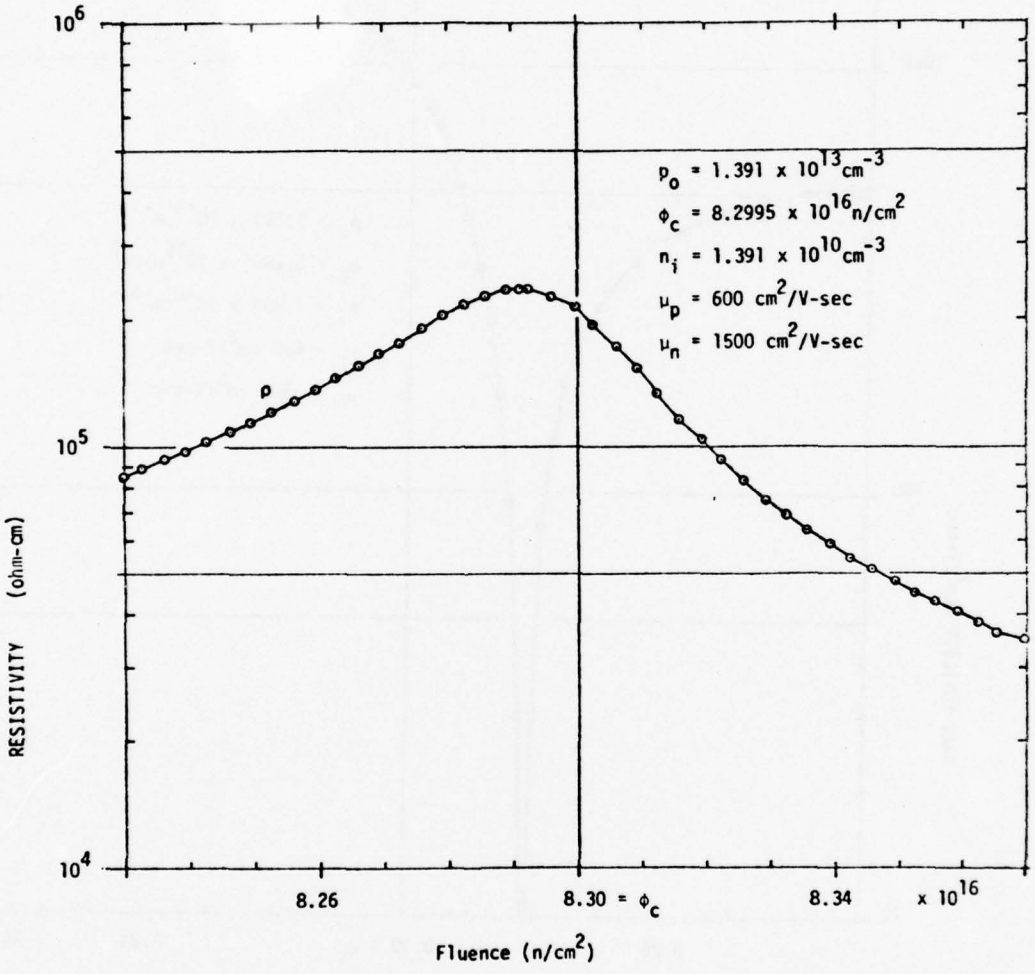


Figure 3. Resistivity vs. fluence.

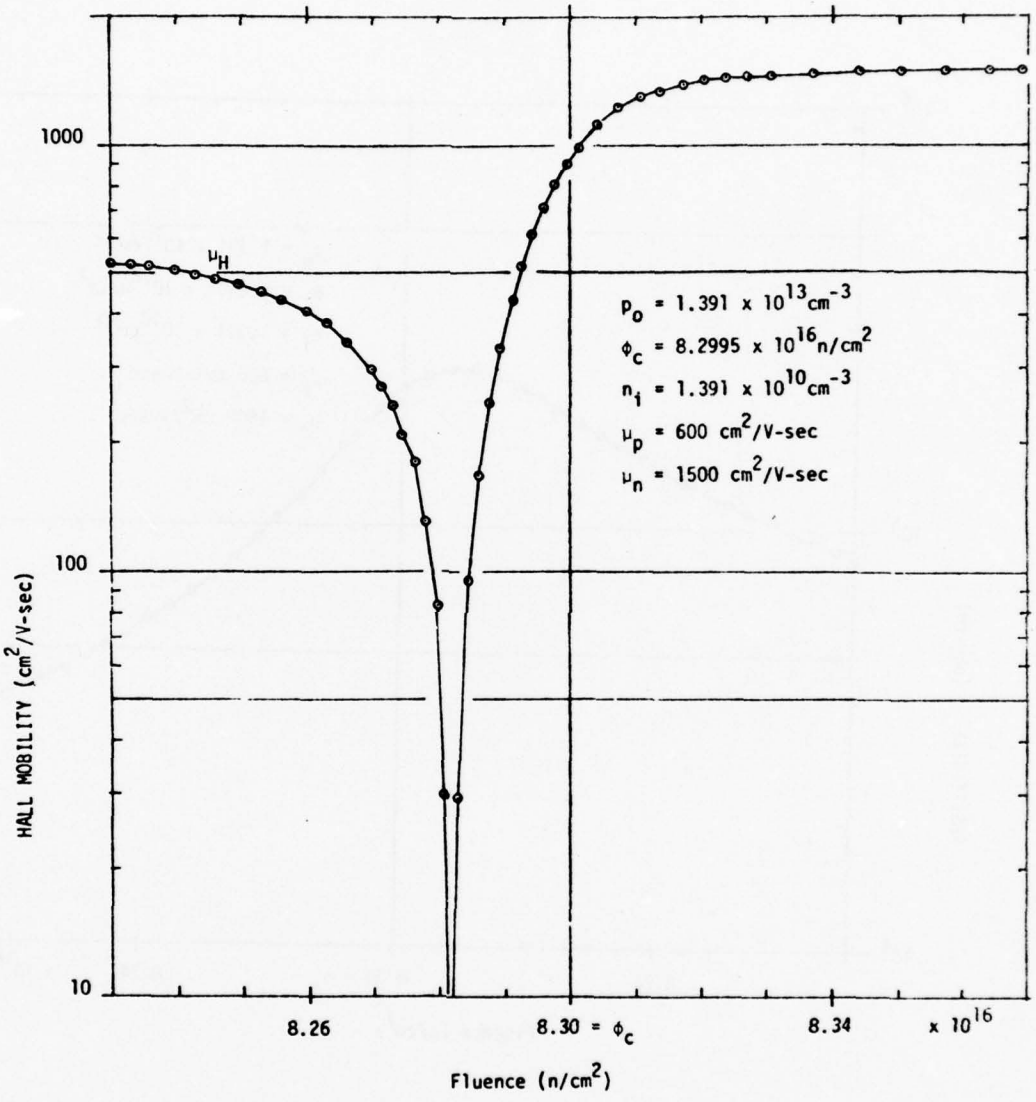


Figure 4. Hall mobility vs. fluence.

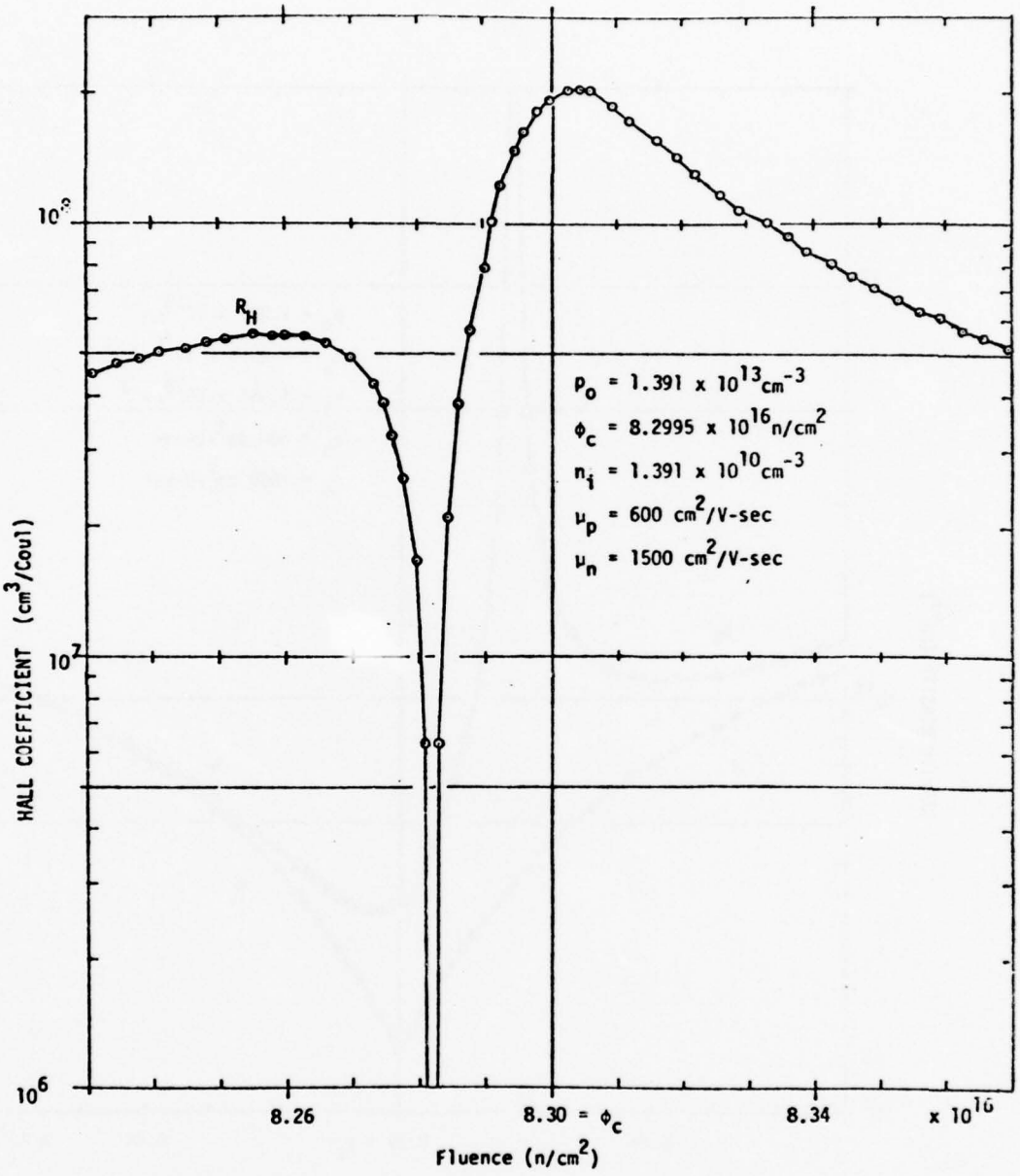


Figure 5. Hall coefficient vs. fluence

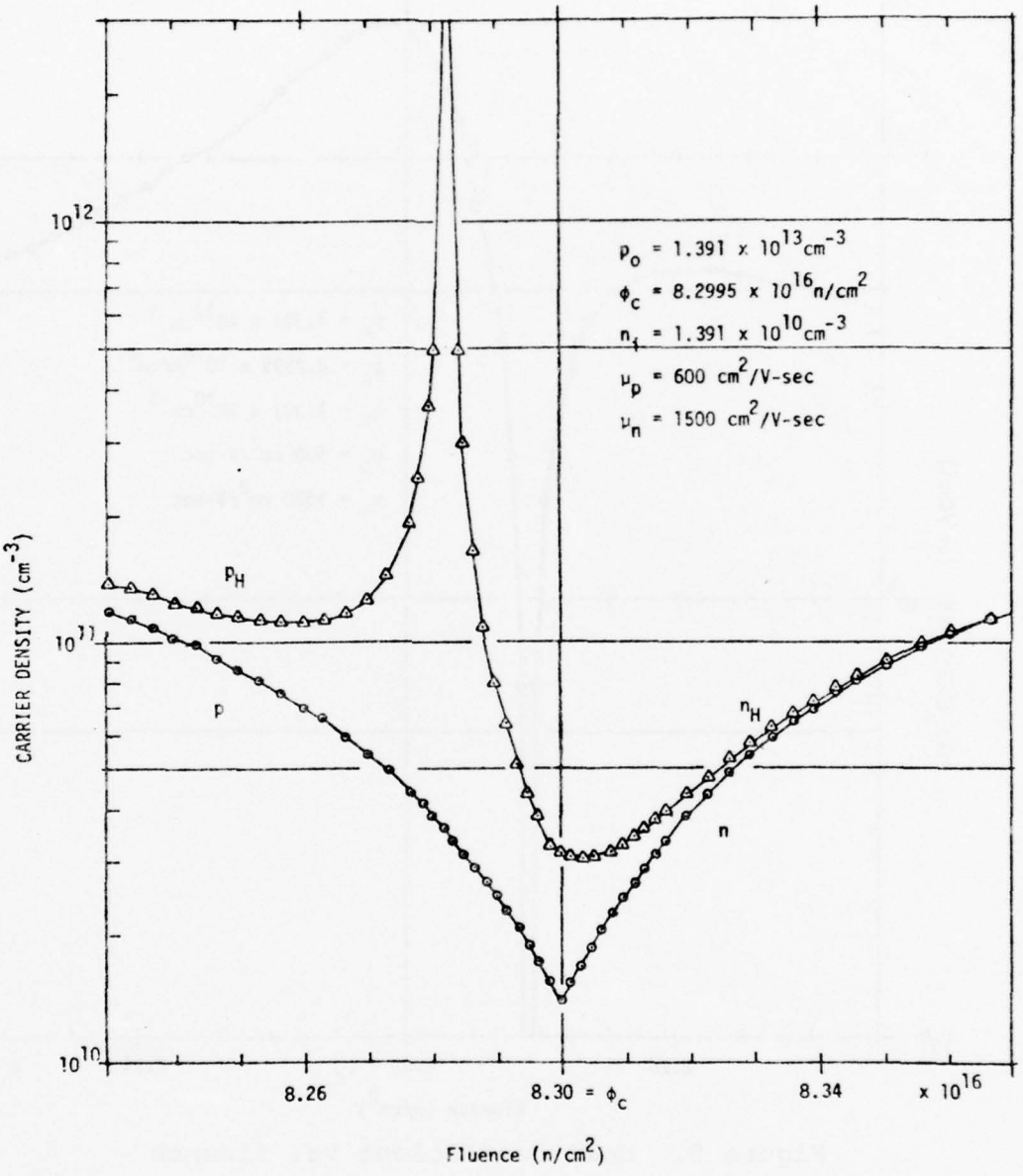


Figure 6. Actual carrier concentration, p, n, and Hall coefficient carrier concentration p_H, n_H, vs. fluence.

III. EXPERIMENTAL TECHNIQUES AND APPARATUS

In this section, a description of the apparatus and techniques required to irradiate the Si and to evaluate the material before and after irradiation is described.

A. Reactor Description

The reactor at the University of Missouri is a high flux, light water moderated research reactor designed to operate on highly enriched fuel. It has a beryllium reflector, a graphite moderator and forced cooling system for pool and core. The reactor is operated at a power level of 10 MW. The reactor runs routinely at 10 MW for 90-100 hours per week, 52 weeks per year. A comparison of the peak flux of the MURR reactor with other research reactors in the United States is shown in Figure 7.

A cross-sectional view of the reactor core and various experimental stations is shown in Figure 8. One of the major advantages of the MURR reactor for Si irradiation is the easy access to the sample positions in the pool and reflector.

At present, two 2" dia. x 30" long silicon sample irradiation positions with sample rotators are located in the graphite reflector in positions I-2 and H-2 in Figure 8. The average flux at these positions is about 3×10^{13} $n/cm^2/sec$. The pneumatic tubes used for activation analysis rapid sampling handling are also shown in Figure 8.

Beyond the graphite positions is the S-basket with seven 3" dia. Si holes which can be rotated manually or mechanically. The flux in the S-basket varies from $10^{13} n/cm^2/sec$ to $10^{12} n/cm^2/sec$.

For the very low fluences required for the exact compensation of detector Si, a variable flux pool facility was developed and constructed. The samples in this position are also mechanically rotated. The flux in this facility is a maximum in the present close-in position and is about $7 \times 10^{11} n/cm^2/sec$. This flux can be reduced considerably by moving the facility further out in the pool. The approximate position of the bulk pool Si facility is shown in Figure 8.

A typical flux profile for the I-2 position is shown in Figure 9. Silicon ingots up to 10" length are positioned in the linear portion of this flux and flipped end for end at precisely 50% of the total fluence.

SOME RESEARCH REACTORS IN THE UNITED STATES

#	REACTOR	LOCATION	POWER (MW)	PEAK FLUX (n/cm^2-sec $\times 10^{14}$)	NO. BEAM TUBES	PEAK BEAM SOURCE FLUX (n/cm^2-sec $\times 10^{14}$)
1	ILL*	Grenoble	57	120	25+	12
2	HFIR	ORNL	100	50	4+	9
3	HFBR	BNL	40	56	9	6
4	MURR	Columbia, Mo.	10	7	7+1	1.2
5	GETR	Pleasanton, Calif.	50	4	(1)	1.0
6	NBSR	NBS	10	2	13	0.9
7	MITR	Boston, Mass.	5	2.2	11	0.8
8	ORR	ORNL	30	4	6	0.8
9	GTRR	Atlanta, Ga.	5	1	10	0.7
10	CP-5	ANL	5	2	8	0.3
11	ALRR	AMES	5	1.2	9	0.3
12	Mich.	Ann Arbor, Mich.	2	0.2	10	0.3
13	RIR	Rhode Island	2	0.2		0.2

*added for comparison

Figure 7. Comparison of research reactor peak flux values in the United States.

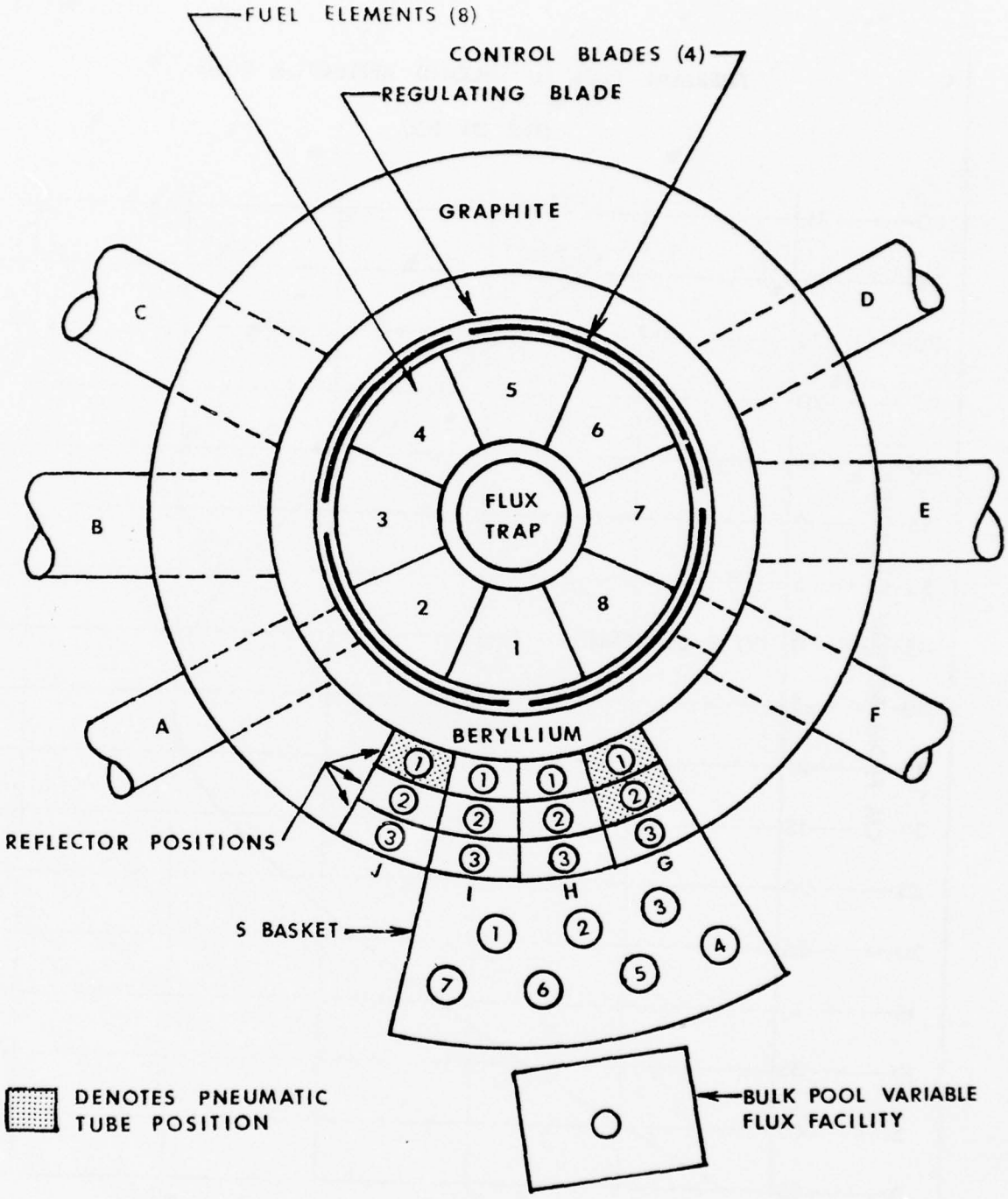


Figure 8. Flux trap, beamports, reflector and bulkpool facilities.

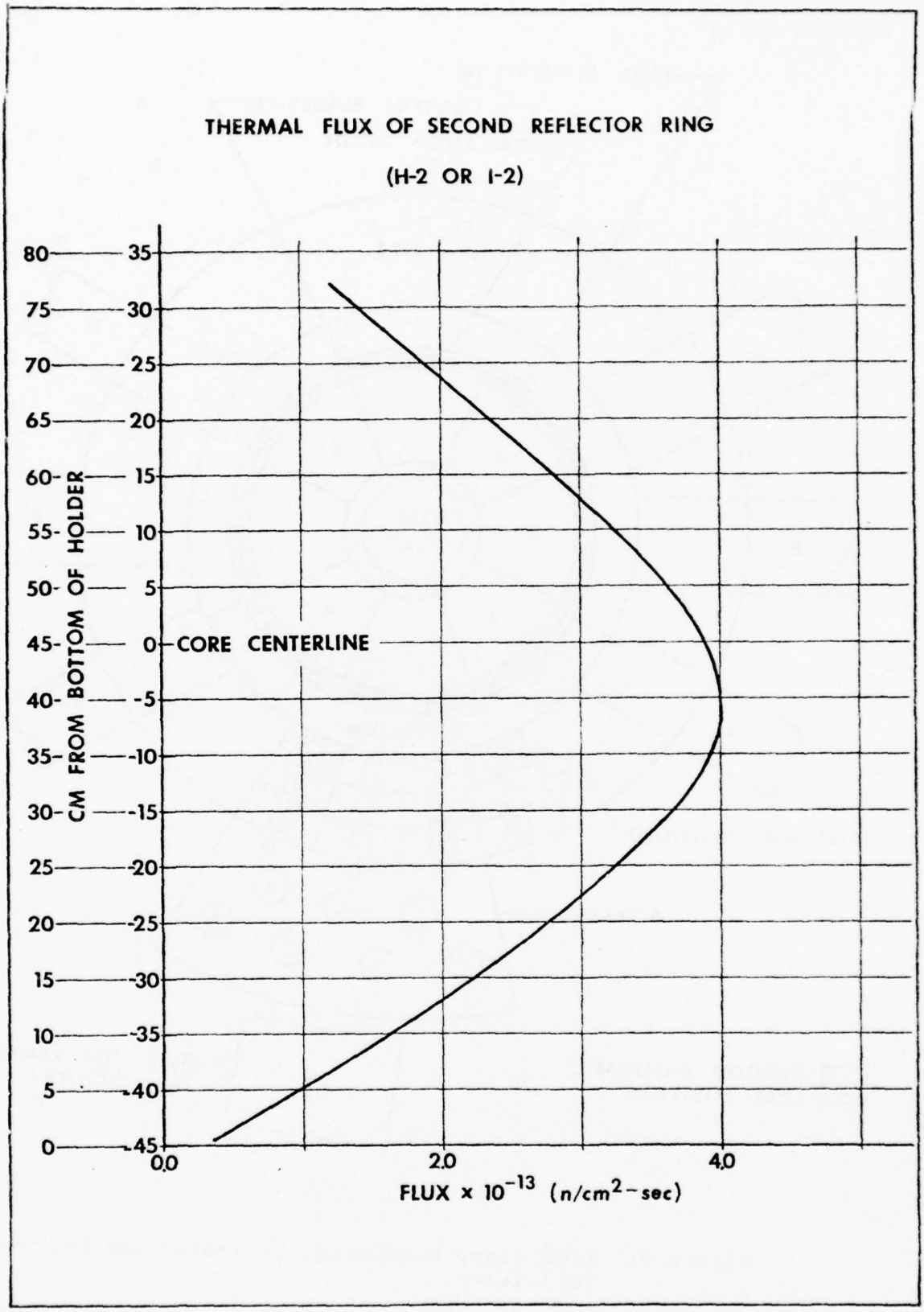


Figure 9. Thermal neutron flux profile in I-2 reflector position.

The flux profiles in the other positions is approximately the same shape but tends to flatten at the peak at positions further from the core. In the variable flux facility, the peak is sufficiently flat to make the peak of the flux profile useful over a 5" length.

B. Bulk Pool Variable Flux Irradiation Facility

A calculation of the fluence required to compensate a typical residual boron concentration of about 3×10^{12} atoms/cm^3 yields a fluence of 1 to 2×10^{16} n/cm^2. A typical loading or unloading time of five minutes and a fluence accuracy of $\pm$ 0.5% restricts the irradiation flux to a value between 1×10^{11} to 1×10^{12} n/cm^2/sec. Since this flux is an order of magnitude lower then that obtained in the S-Basket, a special irradiation facility was constructed for this project. The general location of this "Bulk Pool Variable Flux Facility" is shown in Figure 8.

Figure 10 shows the construction details of the moveable box which is held onto the S-Basket by two rigid rods which pass through holes A. (The sample holding tube is horizontal in this diagram but vertical in the pool). Figure 10 shows a detail of the support rods while Figure 11 shows the detector holder which inserts into the main cylinder in Figure 10. The sample holder is a cylinder which rotates inside the detector hole in Figure 12. It should be noted that the neutron detector spirals concentrically around the sample position so that a very accurate representation of the flux on the sample is continuously monitored. The thermal to fast flux in this facility is estimated to be better then 30:1.

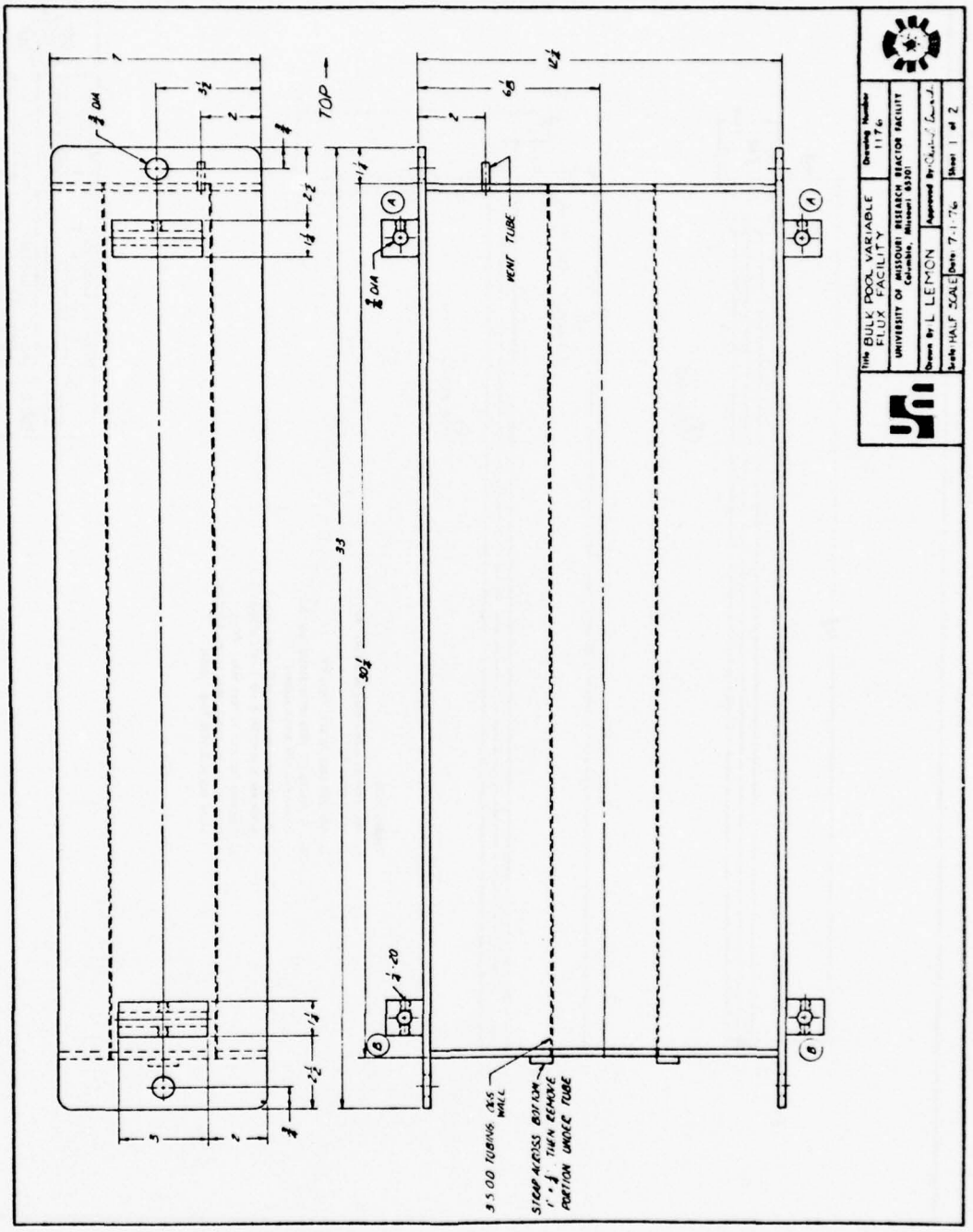


Figure 10. Movable box detail for bulkpool irradiation facility.

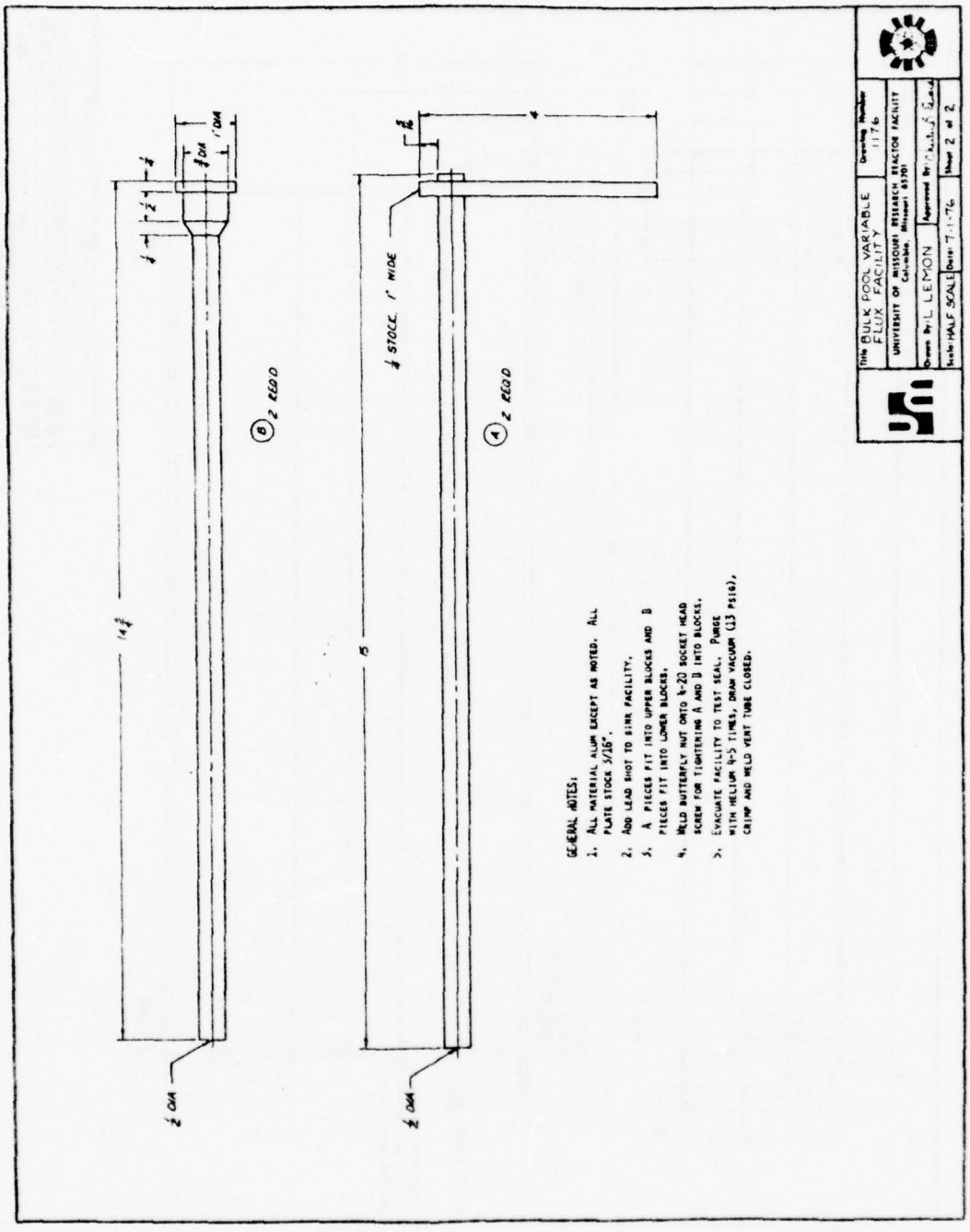


Figure 11. Support rods for variable flux facility.

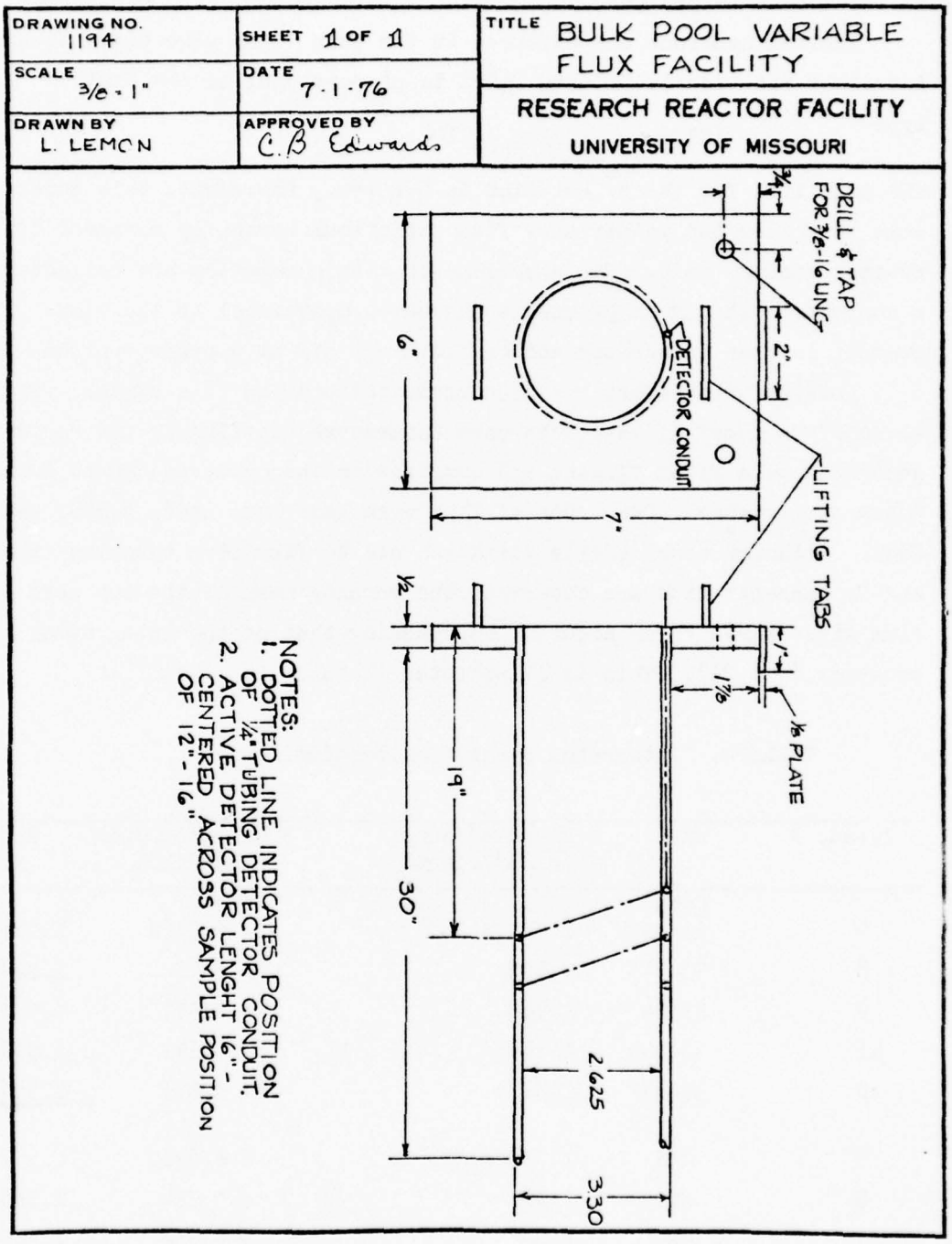


Figure 12. Detector holder for variable flux facility.

C. Neutron Flux Detection and Integration System

The detector discussed in the last section is a self powered detector of the thin wire design.

Thermal neutrons are captured in the thin ^{103}Rh wire (100% abundance). A nuclear reaction is induced which is proportional to the flux of the type

$$^{103}Rh(n, \gamma)\ ^{104}Rh \rightarrow\ ^{104}Pd + \beta^-.$$

The half life for the β^- emission is 4.2 sec., therefore, this detector is able to follow the rather slow flux variations caused by movement of the reactor control rods. The electrons from this reaction are collected on a concentric shield to produce a current proportional to the flux. This current is then integrated and an alarm set off at a predetermined preset.

Considerable effort has been spent calibrating this system. Flux wires of Co doped Al have been used to measure the flux by the radioactivity generated by a given fluence and compared to the observed counts from the integrator system. Two types of flux wire have been used, N.B.S. and Cohn. Although considerable variation due to flux wire counting statistics and Co concentration are observed, the running mean of the two sets of flux wires agree to an accuracy approaching that of the integration system accuracy ($\pm$ 0.2%). This is illustrated in Table 4.

TABLE 4. Integrator System Calibration Data

Irrad. #	Wire	Fluence/Count (n/cm^2/count)	%Deviation from Last Mean	Running Mean
	Cohn			
4	33-34	1.557×10^{12}	- 0.128%	1.557×10^{12}
8	33-34	1.610	+ 3.27	1.594
9	33-34	1.568	+ 0.577	1.578
11	33-34B	1.549	- 0.641	1.576
12	33-34	1.511	- 3.079	1.559
5	NBS	1.553×10^{12}	- 0.830%	1.553×10^{12}
8	NBS	1.482	- 5.364	1.518
11	NBS	1.664	+ 6.258	1.566

$$100 \times \frac{\overline{NBS} - \overline{Cohn}}{(\overline{NBS} + \overline{Cohn})/2} = - 0.449\%$$

We believe we have demonstrated that the fluence as determined by the integration system is accurately known and reproducible to about $\pm$0.5%.

D. Neutron Activation Analysis System

Existing neutron activation analysis (NAA) facilities were employed for measuring elemental impurities in the silicon ingot starting materials. Two NAA irradiation facilities are available: a pneumatic tube transfer system into a neutron flux of about 8×10^{13} n/cm^2-sec which permits the measurement of relatively short-lived activation products; and an outer reflector position at approximately 1×10^{14} n/cm^2-sec for long term irradiations. The gamma-ray spectroscopy instrumentation consists of a lead shielded 50 c.c. high resolution Ge(Li) detector coupled to a 4096 channel MCA with computer compatible magnetic tape output. An I.B.M. 370 computer is used for data reduction. These facilities provide "state of the art" capability and reliability for neutron activation analysis of trace element impurities in silicon.

E. Four-point and Thermal-probes

As discussed in Section II, considerable information can be obtained about the nature of the compensation process by measuring resistivity and majority carrier type after typical majority carrier mobility is established for the ingot or wafer.

Thermal probe measurements of majority carrier type are made in a conventional manner using a variable temperature soldering pencil tip for the hot probe and a steel tip cold probe. The temperature gradient generated signal is fed into a Keithley Model 602 electrometer[5] operated in the center zero current measuring mode usually on a range of 10^{-8} to 10^{-7}A. The hot probe is connected to the electrometer low while the cold probe is connected to the high so that a positive deflection denotes p-type and a negative deflection denotes n-type. The type of the unknown sample is also compared with two standard samples obtained from a multipass zone refined ingot (p-type) and a neutron transmuted and annealed sample (n-type). Agreement of the thermal-probe with Hall effect measurements has been excellent up to resistivities approaching 100,000 Ω-cm once experience is gained with the standard samples. Beyond this resistivity, mixed typing is often encountered suggesting that nonuniform doping is observed before the disappearance of the thermoprobe signal is observed.

Several four point probe heads of different probe spacing and probe pressure have been tried with excellent results in resistivity ranges usually inaccessible to four-point probe measurement. The system consists of a Keithley Model 225 constant current source[5], a Hewlett Packard Model 3465A digital multimeter[6], and an Alessi Industries ATP-1 Test Probe Fixture[7] which has been modified to have a 12" vertical travel and a sample translation stage. Two types of four-point probe heads have been tried, an Alessi Model A4P-25 with a probe spacing of 0.025", a probe load of 70-180 gm; and a Signatone[8] probe with a spacing of 0.065," a tip radius of 0.1 mil and a probe load of 180 gms. Both probe heads have tungsten carbide tips. Although both probe heads work well, the larger probe spacing is more forgiving in current selection and care of measurement as has been used except for very small samples where edge effects become a problem. The usual probe correction factors have been applied to obtain the resistivity from the measured resistance.[9, 10]

To account for nonuniform probe spacing, the probes were lowered onto an aluminized microscope slide and the spacing measured with a traveling microscope. This procedure was repeated several times and a correction term generated from theory.[9] This correction factor was also checked by measuring the resistivity of a transmutation doped and annealed sample which had been calibrated by the Van der Pauw technique.[12] Agreement was found to be better than 1% for a 5 Ω-cm sample. All samples are measured in a dark box.

Since the A.S.T.M. Standard for resistivities over 2000 Ω-cm suggested that measurements could not be made to an accuracy of better than $\pm$15% , extreme care was taken to check the probe calibration factor periodically for high resistivity measurements.

An ingot which had been cut into five bulk samples ($\rho \sim 2500$ Ω-cm) and characterized by four point probes at Rockwell International was measured at MURR. Care was taken to use a current sufficiently low that sample heating did not affect the measurements. The results of I-V plots for two sides of sample VZ-072-#5 are shown in Figures 13 and 14. The nonlinearity in these measurements at high currents is due to sample heating.

Note that the linear portions of the curves do not go through the origin. This offset voltage can be measured on the voltmeter in the absence of current and is observed to vary with probe pressure, surface condition of the sample and position of the probes on the sample. Although this effect is negligible for 5 Ω-cm material, the offset voltage can become an appreciable part of the signal voltage for high resistivity samples. It was also noticed that the slope near the origin is independent of the offset. This fact allows us to make correct measurements up to very high resistivities if proper data handling is used. The problem is overcome by measuring both the positive and negative voltages resulting from positive and negative supply currents to determine the effective resistance. This resistance is then equal to $[\, V(+) - V(-) \,] \,/\, [I(+) - I(-) \,]$. This resistance determines the slope of the lines in Figures (13) and (14) and the product of this slope times the probe factor determines the resistivity.

Results of a series of measurements on the five bulk samples, VZ-072-#1 through #5, are compared to results obtained by Dr. Arst at Rockwell and

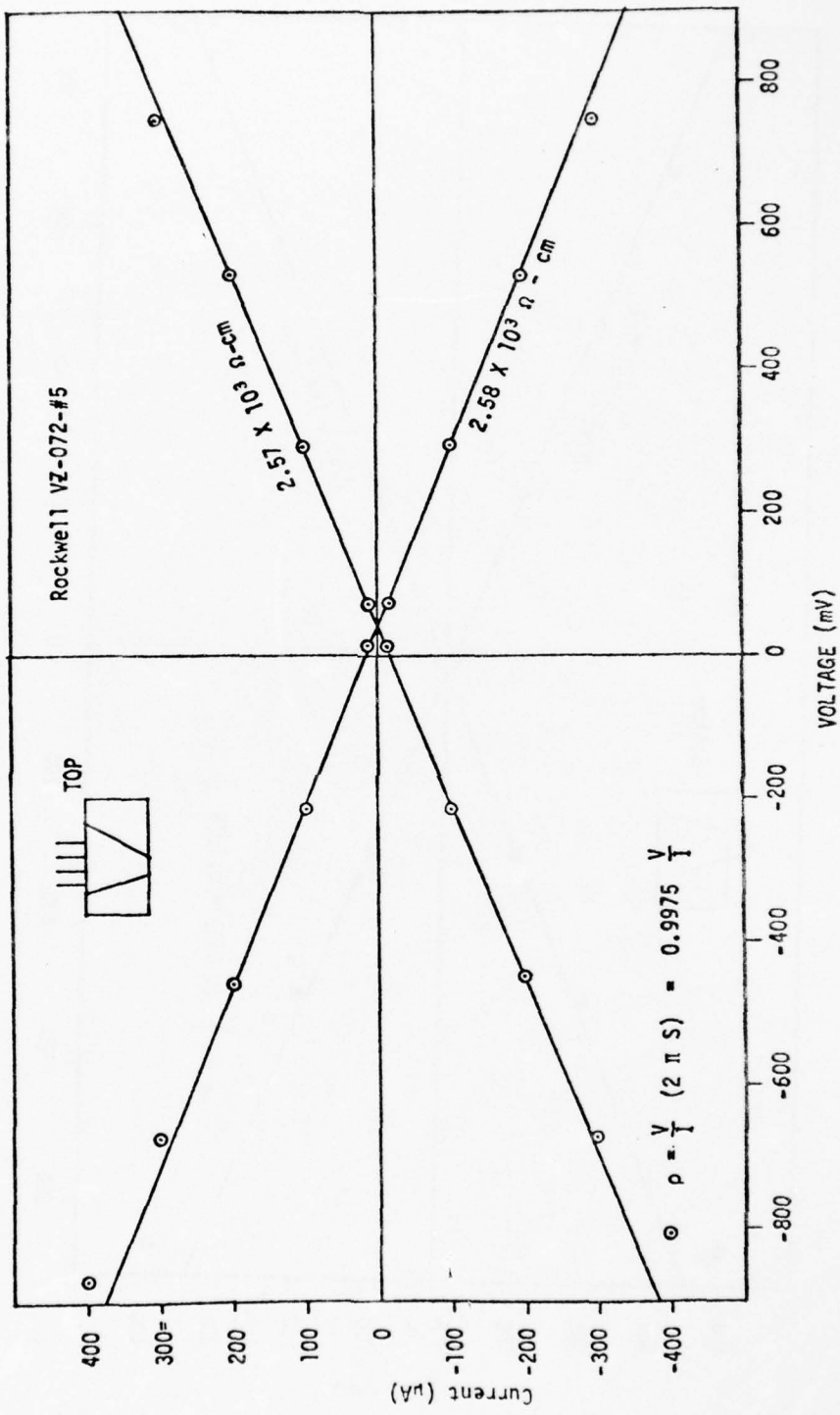


Figure 13. Current vs. voltage for four point probe resistivity measurement (top of VZ-072-#5.)

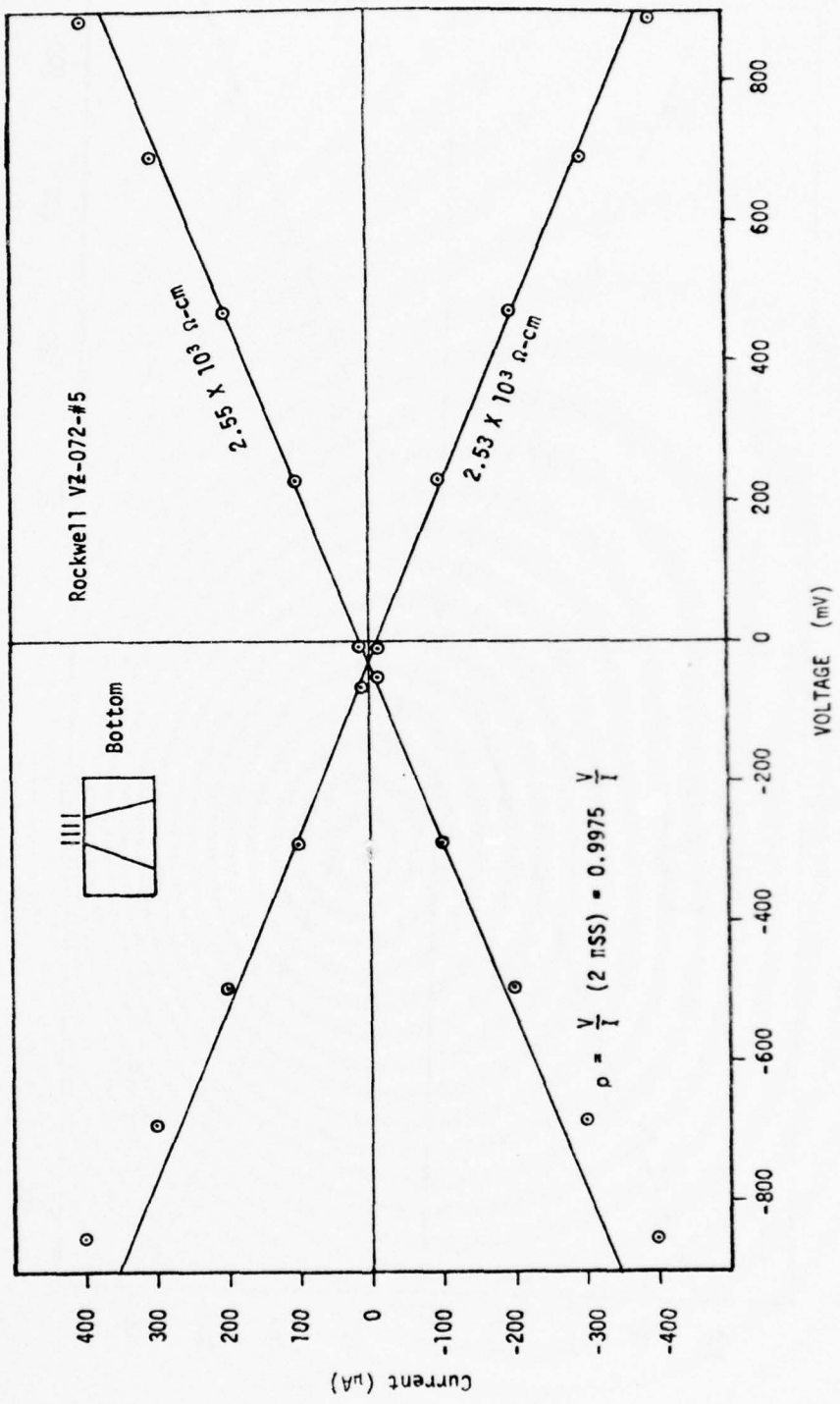


Figure 14. Current vs. voltage for bottom of VZ-072-#5.

are shown in Table 5.

TABLE 5. A comparsion of four point probe resistivity measurements made at Rockwell and MURR.

Sample	Rockwell Data Resistivity (Ω-cm)	MURR Data Resistivity (Ω-cm)	$100\frac{\rho_r-\rho_m}{\rho_m}$
#1(T)	2.29×10^3	2.27×10^3	+0.88
#1(B)	2.42	2.43	-0.41
#2(T)	2.43	2.45	-0.82
#2(B)	2.53	2.53	0.00
#3(T)	2.50	2.52	-0.99
#3(B)	2.57	2.58	-0.39
#4(T)	2.57	2.58	-0.39
#4(B)	2.55	2.56	-0.39
#5(T)	2.55	2.55	0.00
#5(B)	2.53	2.49	+1.61

It is seen that the agreement between the two laboratories is quite good for this resistivity range the average deviation being about $\pm$ 0.6%. The agreement between the four point probe measurements has been observed to decrease with further increases in resistivity. On comparing both laboratories' four point probe measurements with Van der Pauw measurements on samples with resistivities in the 7000-8000 Ω-cm range we find the deviation at MURR from Van der Pauw to be $\pm$ 1.5% while the deviation of the Rockwell measurements is $\pm$ 5%.

This increased error with resistivity seems to be following a power law dependence given by the expression

$$100\frac{\Delta\rho}{\rho} = K\rho^n .$$

Although the constant K is smaller for our data than for that given by the A.S.T.M., the value for n is in reasonable agreement. We find the following to hold for the two sets of data:

$$100 \frac{\Delta\rho}{\rho} = 0.1\ \rho^{0.71} \qquad \text{(A.S.T.M.)}$$

$$100 \frac{\Delta\rho}{\rho} = 0.001\ \rho^{0.81} \qquad \text{(MURR).}$$

The physical meaning of these equations is obscure, however, a similar power law is observed for the calibration curves for spreading resistance measurements. The difference between the A.S.T.M. and MURR values for K are not known, however, the A.S.T.M. data is taken for both n- and p-type Si in various orientations while the MURR data is taken on p-type only on a (111) face. The upper expression is useful for estimating the maximum expected error for intrinsic material at 230,000 Ω-cm. We find an expected value of about $\pm$ 22% at this resistivity value. This estimated error is in reasonable agreement with deviations in resistivity for samples neutron irradiated to the same fluence but before annealing (nearly intrinsic but slightly p-type).

F. Minority Carrier Lifetime Apparatus

The minority carrier lifetime of all ingots before irradiation and some after irradiation and annealing have been measured by the photoconductive decay technique. Ingots are coated with Aquadag solution on each end and held in a small lab vise to which braided copper shielding wire has been flattened and attached to the vise jaws for contacting. The contacting area is shielded from the light to prevent photovoltaic effects from the contacts. This effect can be detected if observed as a linear decay of the junction capacitance of a blocking contact.

A small power supply supplies the bias voltage across the sample and a variable series load resistor. This resistor is adjusted for maximum signal before data is taken, an essential procedure for interpretation of the decay.[14] Optical excitation is provided by a General Radio Strobotac model 1531-AB[15] whose pulse time is short compared to the photoconductive decay time constant. The signal is observed with a Tektronix Type 547 oscilloscope with a dual trace plug-in unit.[16]

Typical decay voltage as a function of time are shown in Figure 15. It can be shown that the voltage signal as a function of time for the condition that R load = R sample is given by[17]

$$\frac{V(t)}{V_{bias}} = \frac{\left(\frac{\Delta n}{n_o}\right)_o e^{-t/\tau}}{\left\{1 + \left[1 + \left(\frac{\Delta n}{n_o}\right)_o e^{-t/\tau}\right]^{\frac{1}{2}}\right\}^2} \qquad (20)$$

where $(\Delta n/n_o)_o$ is the maximum change in minority carrier concentration and τ is the carrier lifetime. For times long compared to the optical excitation decay

$$\frac{V(t)}{V_{bias}} \rightarrow \left(\frac{\Delta n}{n_o}\right)_o e^{-t/\tau} .$$

Therefore, a semilog plot of $V(t)/V_{bias}$ has a slope of τ^{-1} where τ is the minority carrier lifetime.

Care has been taken not to optically overmodulate the samples since this is known to produce exaggerated lifetimes. The procedure we use is to reduce the light intensity until the observed decay time constant becomes a minimum. It is also important that the carrier sweep out time given by

$$t = \frac{L^2}{\mu V_{bias}}$$

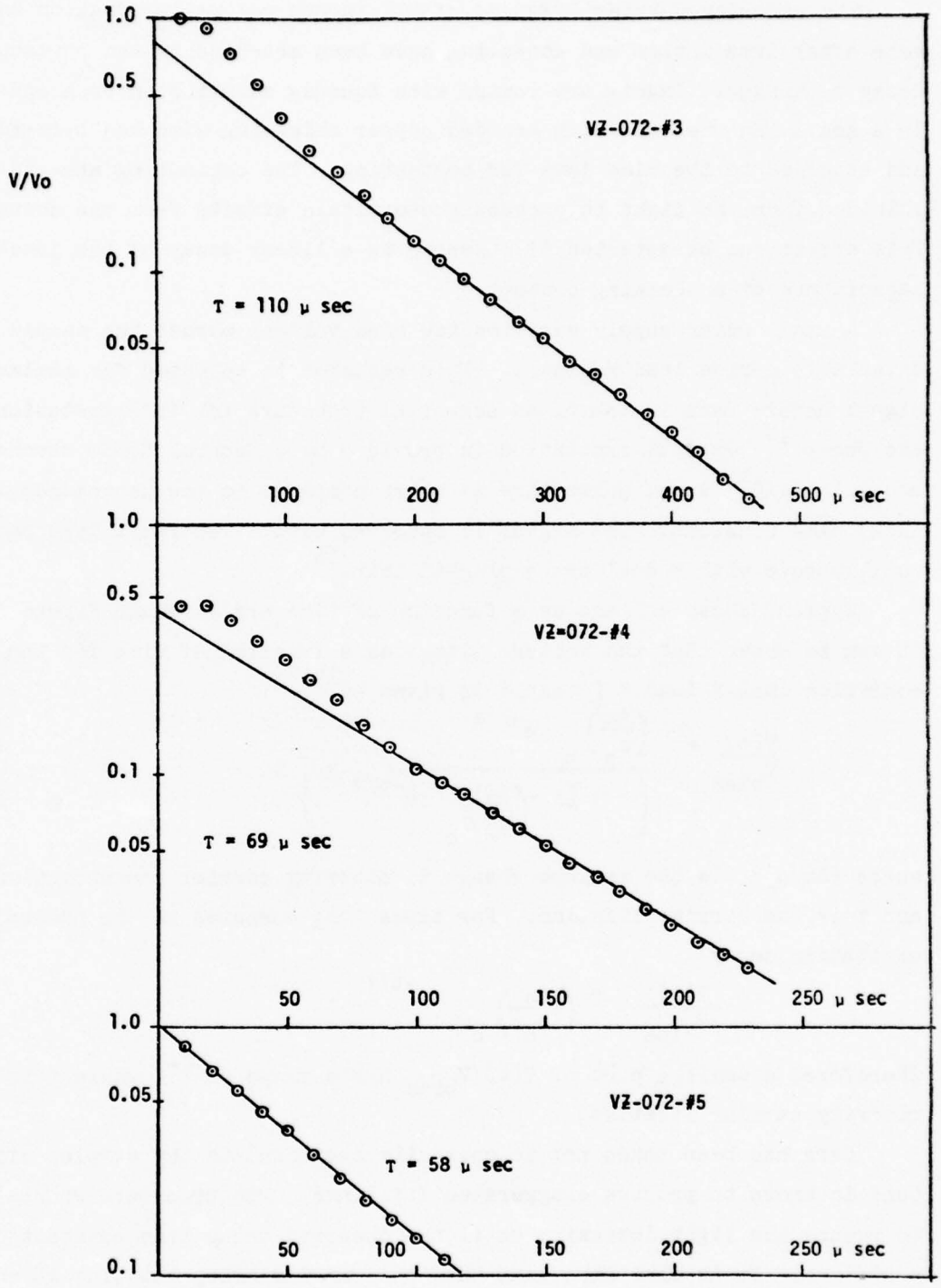


Figure 15. Typical photoconductive decay curves for determining minority carrier lifetime.

where L is the sample length and μ the carrier mobility, be long compared to the decay time.

Trapping effects have been detected in some samples by observing a decrease in the decay time when the sample is simultaneously illuminated from a dc tungsten light source ($\hbar\omega<E_g$). In these cases, the lifetime is assumed to be that observed during dc illumination if the reduction in decay time saturates.

Circuitry has been developed to eliminate the need to take data from the exponential photoconductive decay displayed on the oscilloscope. A variable time constant, variable pulse height exponential generator has been constructed which provides a decay time constant whose value can be obtained from the setting of a ten-turn pot. This exponential pulse is triggered from the strobotac, inverted, and added to the photoconductive decay signal. The oscilloscope then functions as a null detector. A straight line signal indicates that the exponential generator has matched the photoconductive signal in both amplitude and time constant. Deviations from non-exponential decays and trapping effects are easily detected with this system. A schematic of the system is shown in Figure 16 while a circuit diagram for the exponential pulse generator is shown in Figure 17.

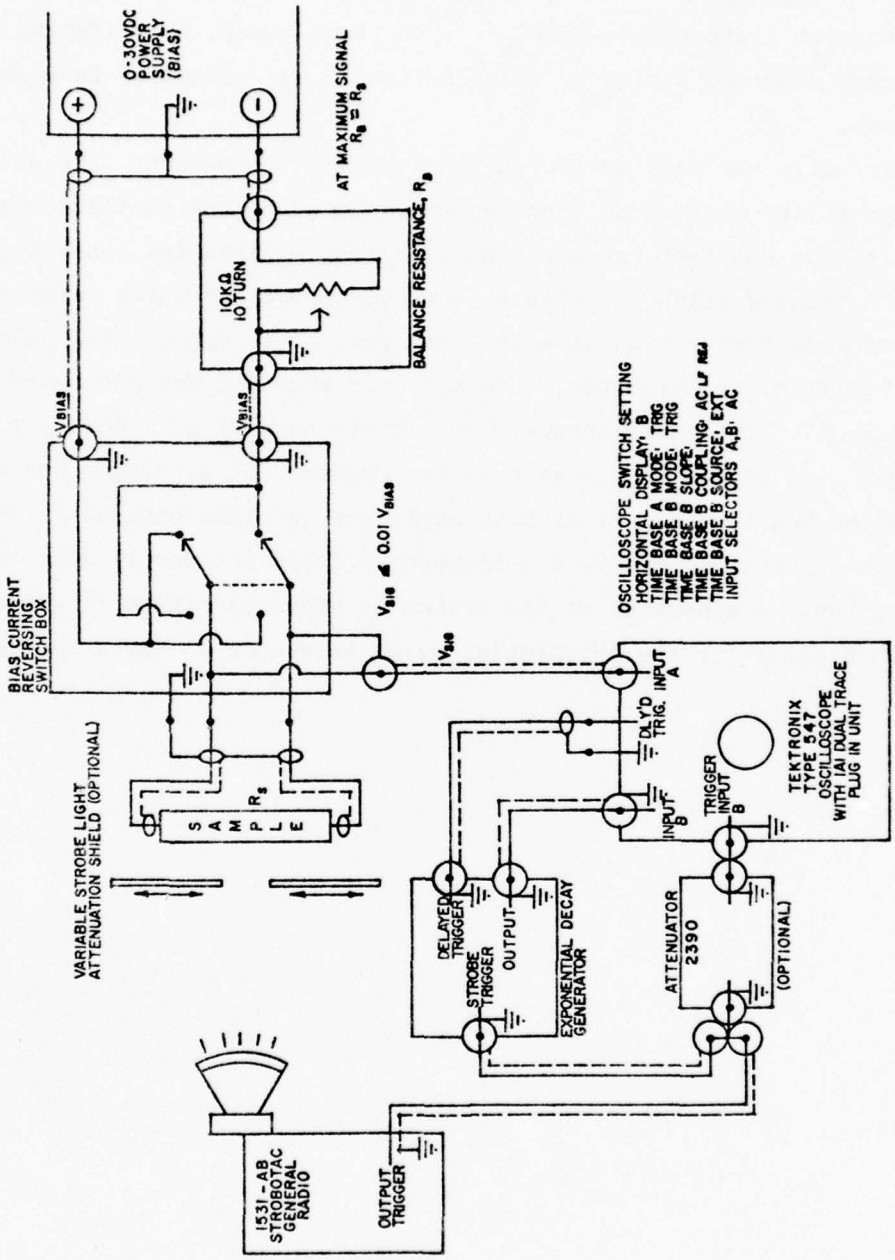


Figure 16. Minority carrier lifetime measurement apparatus.

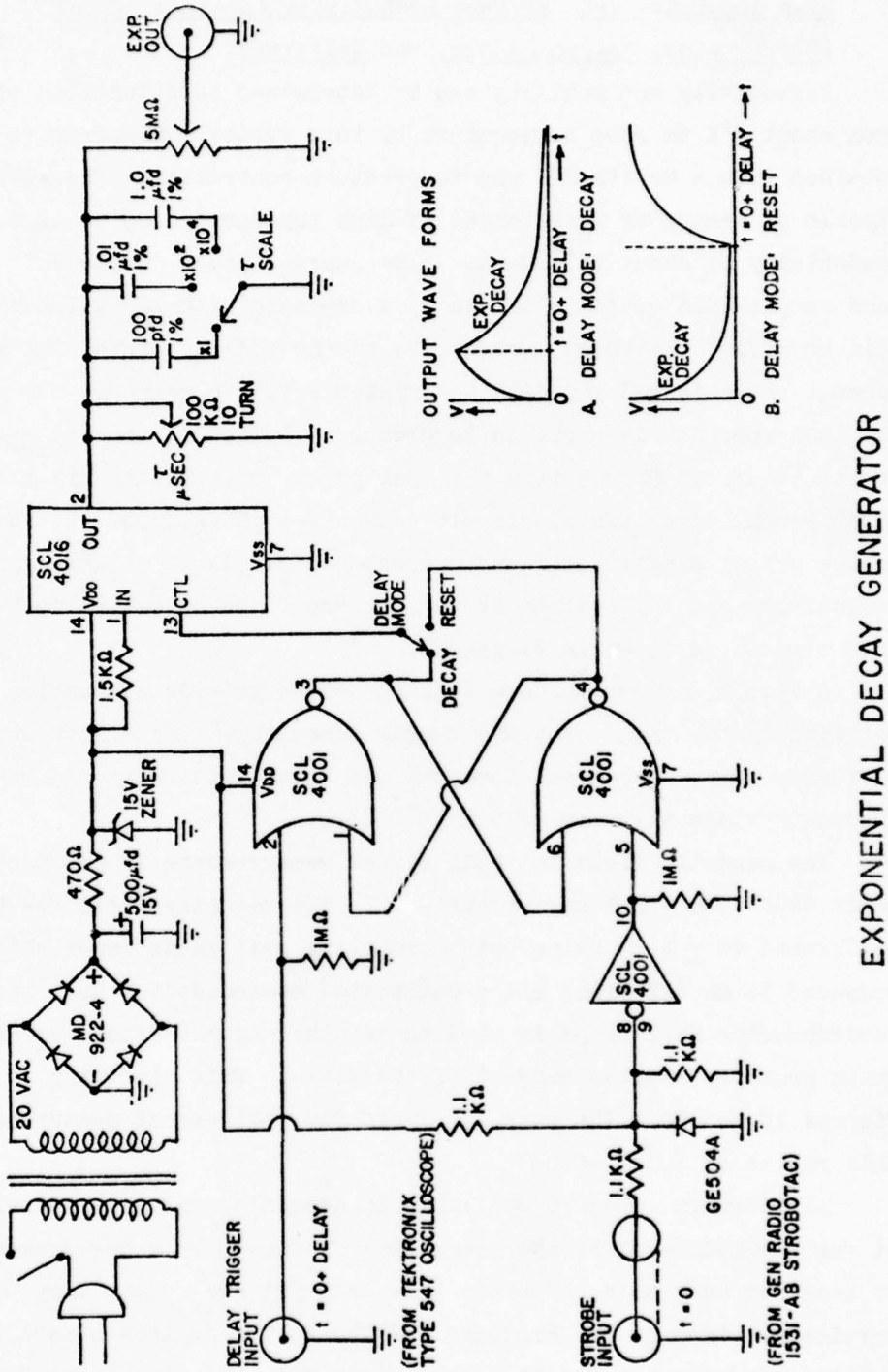


Figure 17. Exponential decay generator.

G. High Impedance Van der Pauw Resistivity and Hall System (Electronics, Vacuum System, and Helitran).

Resistivity and mobility can be determined as a function of temperature from about 8°K to room temperature by this system. Temperature control is obtained from a Helitran[18] and temperature controller. The system is capable of measuring resistances of high impedance samples up to a resistivity of about 10^{12} Ω-cm. A dc guarded lead approach[19] in which each sample lead guard is driven by a separate high imput impedance unity gain amplifier (Keithley[5] Model 602) to the voltage on the inner lead reduces leakage currents and improves the system's time constant. The circuitry for this approach is shown in Reference 19. The digital voltmeter and constant current source from the four point probe system are also used in this system. A switching circuit connecting the appropriate sample leads to the proper electrometer and current source allows either conventional resistivity and Hall effect or Van der Pauw[12] measurements to be made. This circuit is shown in Figure 18.

A vacuum system has been constructed to provide evacuation for the Helitran system and for the vacuum annealing. The system uses an oil diffusion pump, mechanical forepump and liquid nitrogen cold trap. This system provides a vacuum of 5×10^{-7} torr.

The magnetic field for Hall effect measurements is provided by a Varian Model V4004 four-inch magnet system.[20] The magnetic field has been calibrated to ± 1.3% using both a rotating coil gauss meter which has been compared to an NMR probe and a calibrated semiconductor Hall probe. The semiconductor Hall probe is used to set the magnetic field using circuitry which provides digital readout of the field. This circuitry is shown in Figures 19 and 20. The magnetic field for Hall effect measurements in this report is 6.195 kG.

Although it would be desirable to determine the dominate energy levels at various points along the annealing curves by a measurement of n vs T, we have not been able to obtain this data yet due to the very poor customer service provided by Air Products. Although the cryogenic part of the Helitran system has functioned properly from the time it was received, the whole system was delivered six weeks after the date promised. Furthermore, another six week delay resulted from improper Helitran wiring which required

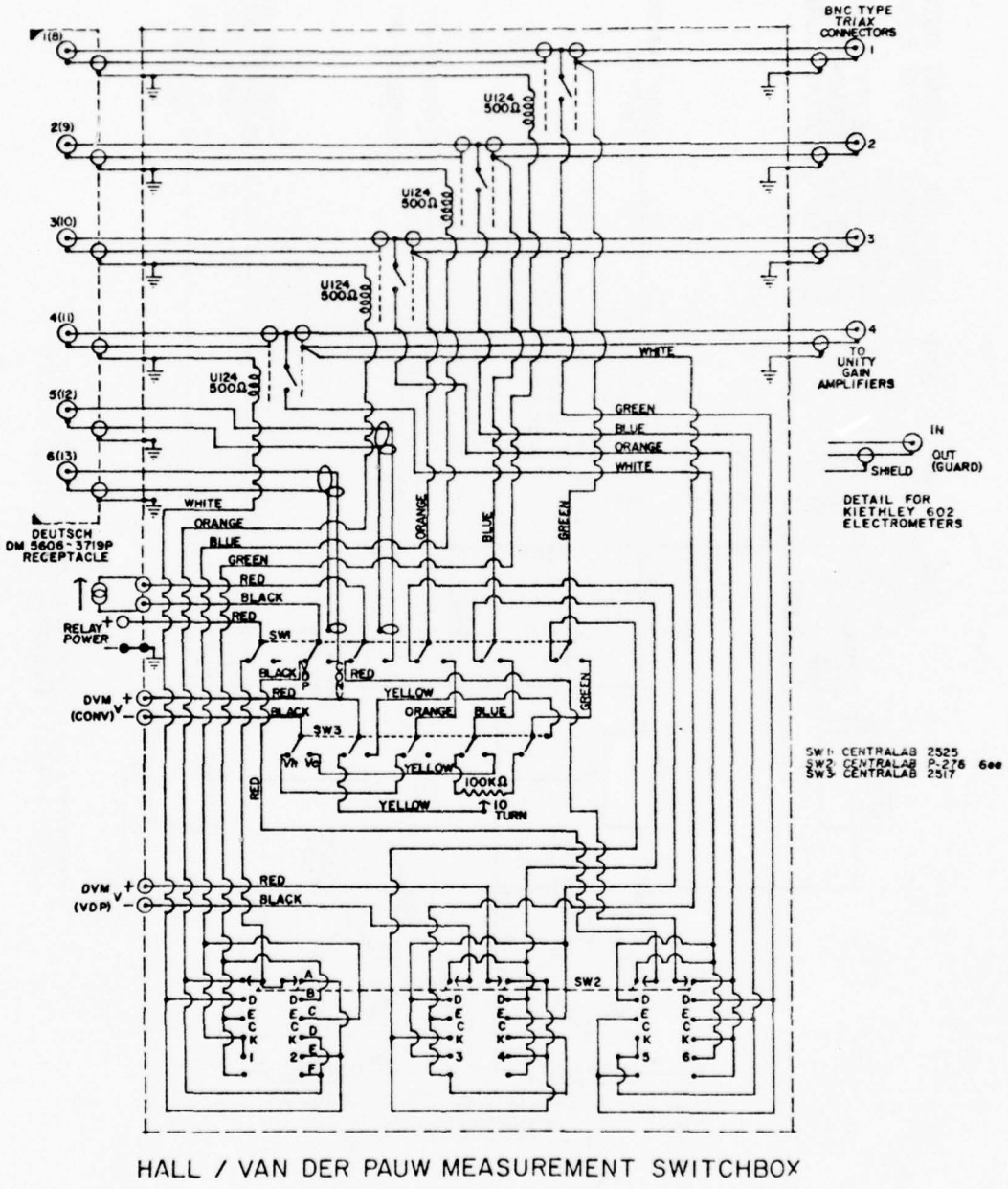


Figure 18. Switching circuit for resistivity and Hall effect measurements.

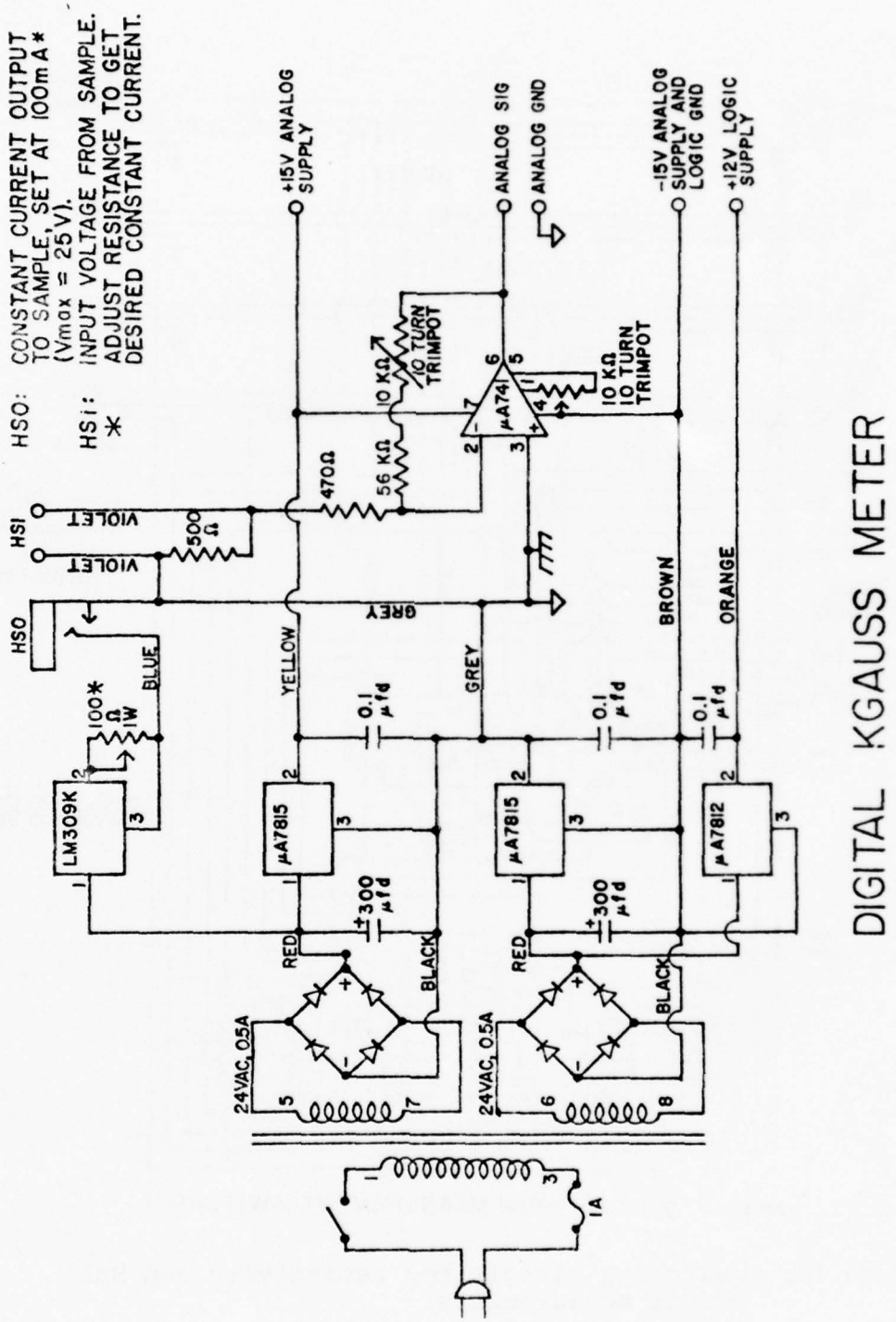
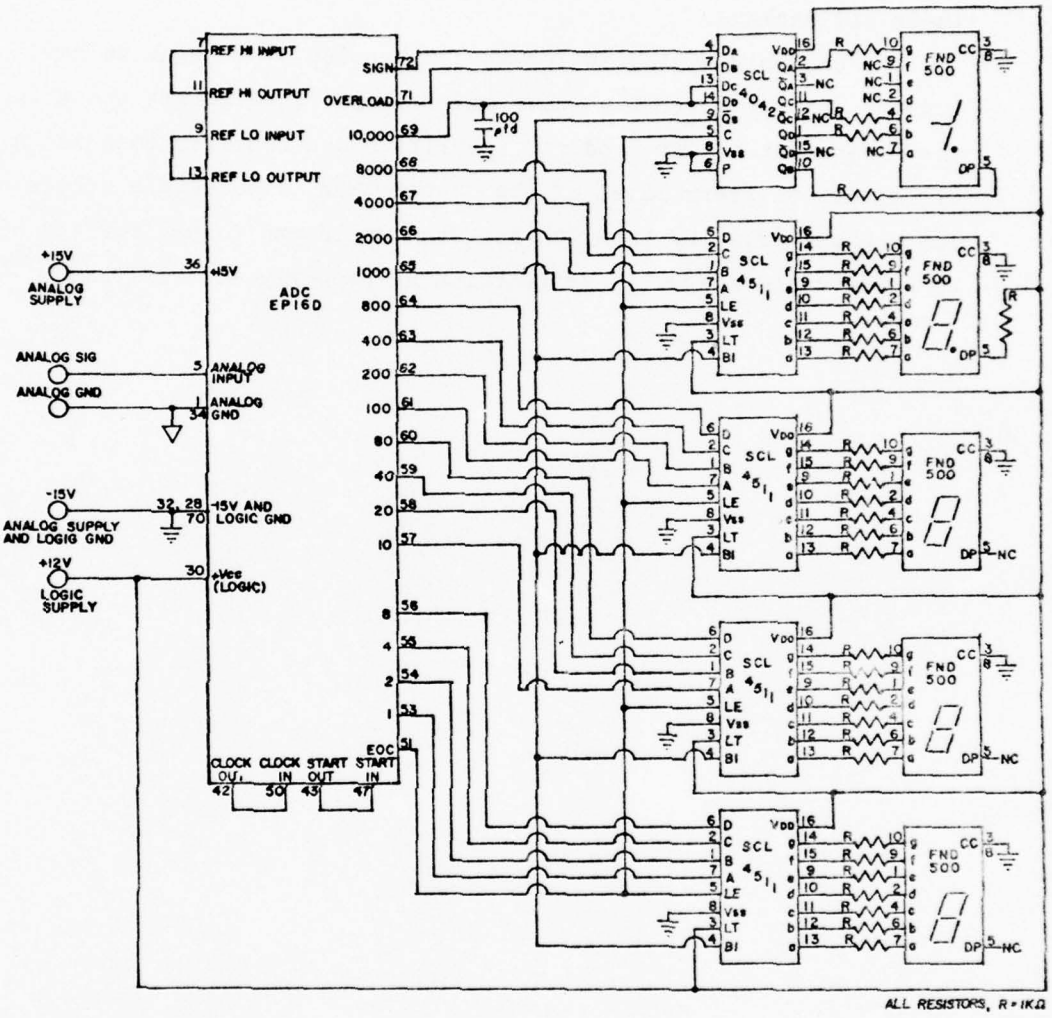


Figure 19. Analog voltage amplifier and current source for digital Gaussmeter.



DIGITAL KGAUSS METER

Figure 20. Analog to digital converter circuitry for digital Gaussmeter.

a return to the manufacturer. An additional three month delay was caused by late delivery of the temperature controller and its failure on the second cool-down. Finally, a heater short to a thermalcouple was discovered which caused heater failure and another two week delay; a total delay of nearly five months beyond the delivery date promised by Air Products in their bid package.

We can only apologize for this situation over which we have had little control and report that we have made every effort to get the attention of the management of Air Products (over 15 phone conversations and a series of letters to every level of the corporation) with little success except for a phone call, by them, to ask when we intend to pay for the Helitran! We believe the system to be functioning properly at this time.

H. Photoconductivity System

Because the transmutation doping studies have been performed thus far on undoped material, the necessity of performing photoconductivity studies to obtain the degree of compensation or the photoconductive spectral response have not been needed. This system has been developed in anticipation of work hopefully to be completed near the end of the contract. The system consists of a glow bar light source, a Perkin-Elmer double pass prism monochrometer and electronics, two thermocouple detectors and exit optics. The prism and windows are KRS-5 material (1-50 μm). The exit beam from the monochrometer which is diverging is intercepted by a spherical mirror to produce a parallel beam of light. Part of this parallel beam is interrupted by a diagonal plane mirror and focused on a reference thermocouple detector with a KRS-5 window. The other part of the beam is focused through a second window onto the photodetector sample mounted in the Helitran by another spherical mirror. By taking ratios of these two signals the spectral response of the photodetector can be obtained normalized to the light source and system response. The final construction of the output optics table is now underway and should be completed soon.

I. Miscellaneous: Sample Preparation Equipment, Annealing System, Irradiation of Silicon, Post-Irradiation Handling

Samples are cut into wafers either by a diamond wire saw or diamond disk cut-off saw. The latter has been found more suitable for silicon. Samples are heavily etched after cutting to remove surface damage in a conventional HF/HNO_3/acetic etch. Samples are then ground using various grades of SiC and Al_3O_4 grits and finally washed in deionized water, acetone, methanol, and trichloroethylene.

Samples are annealed in a tube furnace inside a Spectrasil quartz tube. The sample may be annealed in either a vacuum of 5×10^{-7} torr. or in a flowing inert gas atmosphere. Sample surfaces are protected on each side with a wafer of float zone silicon to prevent contamination by the quartz. The furnace is capable of temperatures of up to 1000°C. The temperature is regulated to $\pm$ 0.5°C.

Samples to be irradiated are placed between silicon spacers; the whole stack of samples and spacers is then wrapped in aluminum foil. The flux wires are now wrapped around the foil and the whole package is placed in an aluminum can which is welded shut to protect the silicon from the pool water. Radioactivity is monitored after a cool-off period in the reactor pool. For the very light irradiations in this project, radioactivity decays to background very quickly and has usually been attributed to surface contamination where encountered.

A considerable effort has been spent studying surface contamination after irradiation but before annealing. By careful handling, no surface contamination has been detected before annealing except for a Au contamination on one sample from sawing in another laboratory before our saws were operational. A few samples have also shown traces of Na from handling. This has been eliminated by a light HF cleaning after irradiation but before annealing. We are confident that our samples are extremely clean prior to annealing based on activation analysis.

IV. EXPERIMENTAL RESULTS AND DISCUSSION

In this section, the prior-to-irradiation material evaluation, irradiation and annealing experiments are discussed. We have noted several differences in our results from previously published work and will discuss these differences in the following subsections. A preliminary activation energy for the electrical activity of the irradiation produced donors has been measured. We have been able to determine that the best single annealing temperature for NTD-Si at above 800°C for one hour followed by a very slow cool down.

Although material from a variety of Si producers has been evaluated, we have found that control by compensation on the p-type side of type conversion from 5000 Ω-cm to intrinsic is impossible in the material we have investigated. We will present data which suggests that residual oxygen is the source of difficulty.

We have also demonstrated very good control of resistivity on the n-type side of type conversion. We have shown that the final resistivity can be controlled to at least $\pm 2\%$ using only a preliminary check of ingot mobility and four point probe measurements. We have sound experimental evidence at this point which suggests that it may be possible to achieve this degree of control up to n-type resistivities as high as 50,000 to 70,000 Ω-cm. This corresponds to an excess donor concentration of $\sim 2 \times 10^{-2}$ ppb or about 1×10^{12} donors/cm^3. It may thus be possible to compensate residual boron concentrations of about this order of magnitude or larger.

One of the more exciting possibilities to develop out of the present work is residual oxygen decoration by damage defects. Circumstantial evidence suggests that oxygen detection in Si can be pushed at least three orders of magnitude below present detection limits. If the preliminary results can be substantiated by EPR and optical measurements, considerable progress in Si purification can be made as a result of this technique.

A. Materials Evaluation Before Irradiation

All the material investigated has been multizone refined float zone silicon with resistivities from 2500 Ω-cm up to 25000 Ω-cm. The material is p-type and not intentionally doped. The dominant acceptor is undoubtably boron. All of the material is nominally dislocation free and pulled in a (111) direction except the Rockwell material which is dislocated and pulled in a (100) direction. Neutron reflection rocking curves show reflection line widths of about 1 sec of arc for the dislocation free material and about 1 min of arc for the dislocated material. Material investigated has come from Dr. Arst, Rockwell; Topsil, Wackers, Monsanto, and a Texas Instruments Lopex sample supplied by Dr. Spry of AFML. We have added an in-house number to each ingot or wafer (MURR #) and have cross-referenced these numbers with whatever sample designations have been assigned to the samples by the suppliers.

Much effort has been expended in trying to purchase float zone silicon which is doped with either In or Ga. Approximately thirty manufacturers of silicon were contacted by phone and requests for bids sent out to ten, however, no bids were received for this type of material. We have, however, received free, doped samples from a number of sources and greatfully acknowledge their help. We have received Czochralski grown Si:Ga doped to a variety of levels in the range of 10^{16} to 10^{18} cm^{-3} from Drs. M. Bressler and C. M. Parry, Aerojet ElectroSystems Co. We have also received a supply of Wacker's Ga doped vacuum float zone material from Dr. M. Schlacter, Aeronutronic Ford. Dr. Arst of Rockwell has also supplied us with Ga doped float zone.

Because of difficulties in obtaining doped material and because of the poor service supplied to us by Air Products, we have not as yet characterized the Ga doped material sufficiently to irradiate it, however, this phase of the program has now begun and hopefully will be completed by the end of the contract.

Table 6 summarizes sample characterization before irradiation. As discussed in a previous section, four point resistivity measurements have been compared with Van der Pauw resistivity measurements for calibration purposes. Mobility measurements have been taken from one slice of each ingot and the values are very near average values given in Table 3.

TABLE 6. Summary of Undoped Sample Characterization Before Irradiation

MURR #	Source	ρ(4 pt) (Ω-cm)	ρ (V.d.P.) (Ω-cm)	μ_D (cm^2/V-sec)	Type T.P.	Type Hall	τ (μsec)
0	Monsanto FZ	749.0			P		-
1	Rockwell VZ-072-3	2560.			P		110
2	VZ-072-3	2953.			P		110
3	VZ-072-3	3156.			P		110
4	VZ-072-3		2721.	464.75	P	P	110
5	Monsanto FZ		1690.	1383.4	N	N	-
6	Monsanto FZ		1037.5	1404.5	N	N	-
7	Rockwell VZ-072-2	2450-2530 (ingot)			P		112
8	Rockwell VZ-083-4	7630.	7729.	524.8	P	P	-
9	Rockwell VZ-083-5	8189.	8067.	527.8	P		-
10	Monsanto CZ	(after irrad & anneal)	3.222	1267.0	N	N	-
11	Monsanto FZ		1376.2	1473.5	N	N	-
14	Topsil 36-520-0-III				P		1200
15	Topsil 36-520-0-III	4710-6467	(1" ingot)		P		1200
16	Topsil 36-520-0-III	4742.			P		1200
17	Wackers 30661-6	66512. ?			P		530
18	T.I. Lopex L1092	4607			P		250
19	Topsil 36-520-0-III		4942.	460.	P	P	1200
20	T.I. Lopex L1092		5195.9	443.86	P	P	250
21	Wacker 30661-6	19370.			P		530 (trapping)
22	Wacker 30661-6	20420.		427.0	P	P	530

TABLE 6. Summary of Undoped Sample Characterization Before Irradiation (Cont.)

MURR #	Source	ρ (4 pt) (Ω-cm)	ρ(V.d.P.) (Ω-cm)	μ_D (cm^2/V-sec)	Type T.P.	Type Hall	τ (μsec)
23	Similar to MURR 10				N		-
24	Wacker 30661-6	For NAA			P		530
25	T.I. Lopex L1092	For NAA			P		250
26	Topsil 36-520-0-III	For NAA			P		1200
27	Topsil 36-520-0-III	5248			P		1200
28	Monsanto FZ	1540			N		-
29	Rockwell VZ-083-17	12509.			P		-
30	Rockwell VZ-083-18	12796			P		-
31	Rockwell VZ-083-19	13326			P		-
32	Rockwell VZ-083-20	13687			P		-
33	Rockwell VZ-083-21	14160			P		-
34	Rockwell VZ-083-22	14382			P		-
35	T.I. Lopex L1092	5895			P		-
36	T.I. Lopex L1092	5587.6			P		-
To Check Uniformity	VZ-072-1	2270-2430					
	VZ-072-2	2450-2530					
	VZ-072-3	2520-2580					
	VZ-072-4	2580-2560					
	VZ-072-5	2550-2490					

Note, however, the Wacker's sample is some 13% too low. This is probably due to the effect of mixed conduction in this very high resistivity sample.

Figure 21 shows the axial resistivity and minority carrier lifetime of ingot VZ-072 after cutting it into slices of approximately 1" thickness. Figures 22 through 27 show the radial uniformity of these samples as obtained from four point measurements.

The rise in resistivity is due to edge effects and is not real.[9]

Table 7 summarizes the minority carrier lifetime for the various ingots which have been measured.

TABLE 7. Summary of Minority Carrier Lifetimes

Source	Ingot No.	τ Measured	τ Specified by Manuf.
Rockwell	VZ-072	100 μsec	100 μsec
Topsil	36-520-0-III	1200 (trapping)	1700
T.I. Lopex	L 1092	250	500
Wacker	30661-6	530	3200

We believe that the lifetimes in this resistivity range are probably over exaggerated by the suppliers because of overmodulation in experimental set ups designed in general for lower resistivity material. It should be noted that our observed lifetimes for the Rockwell material are in general agreement with their measurements. The lifetime of the Topsil material indicates some evidence of trapping which does not saturate. It is, therefore, possible that the real lifetime is shorter. We would estimate, however, that it is probably not shorter than 500μsec.

Table 8 summarizes the drift mobilities observed for the various ingots obtained from Hall mobilities using the relationship for the Hall factor shown in the table.

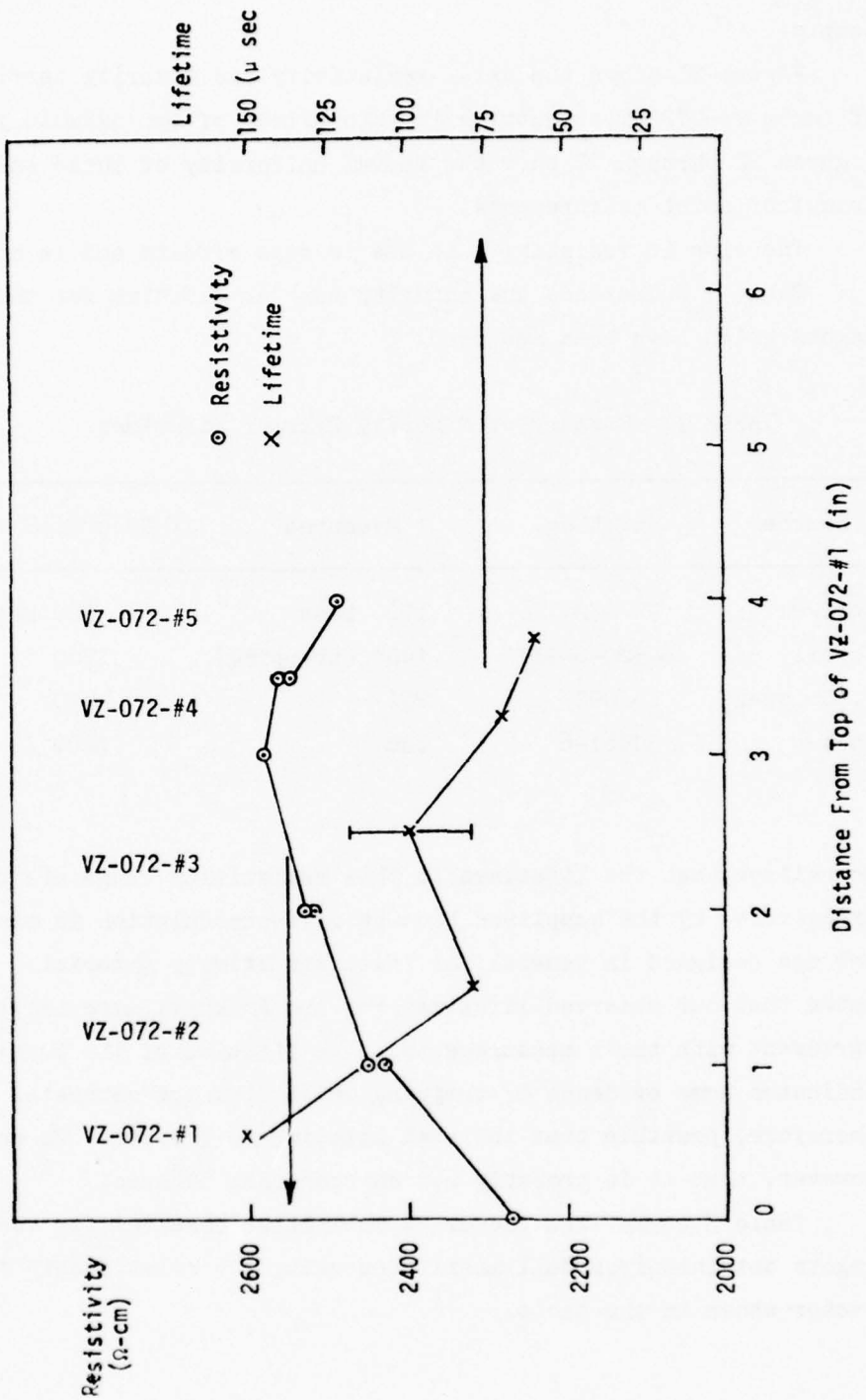


Figure 21. Axial resistivity and axial lifetime of ingot VZ-072.

TABLE 8. Summary of Drift Mobilities

Source	Ingot No.	Type	μ_D (cm^2/V-sec)
Rockwell	VZ-072	P	465
Rockwell	VZ-082	P	525-528
Topsil	36-520-0-III	P	460
T. I. Lopex	L1092	P	444
Wacker	30661-6	P	427
Monsanto FZ	-	N	1383-1473
Typical from Table 3		P	494
		N	1396

$r_p = \mu_H/\mu_D = 0.77$

$r_N = 1.3$

We conclude, based on the data in Tables 7 and 8 that the materials from these sources is of comparable crystal quality. The Rockwell material is slightly inferior, however, the material was pulled in a (100) direction which is more difficult. Apparently, a (111) Rockwell pull would be of comparable crystal quality. In addition, the Rockwell material has the added advantage of extremely uniform boron distribution as evidenced by Figures 22-27.

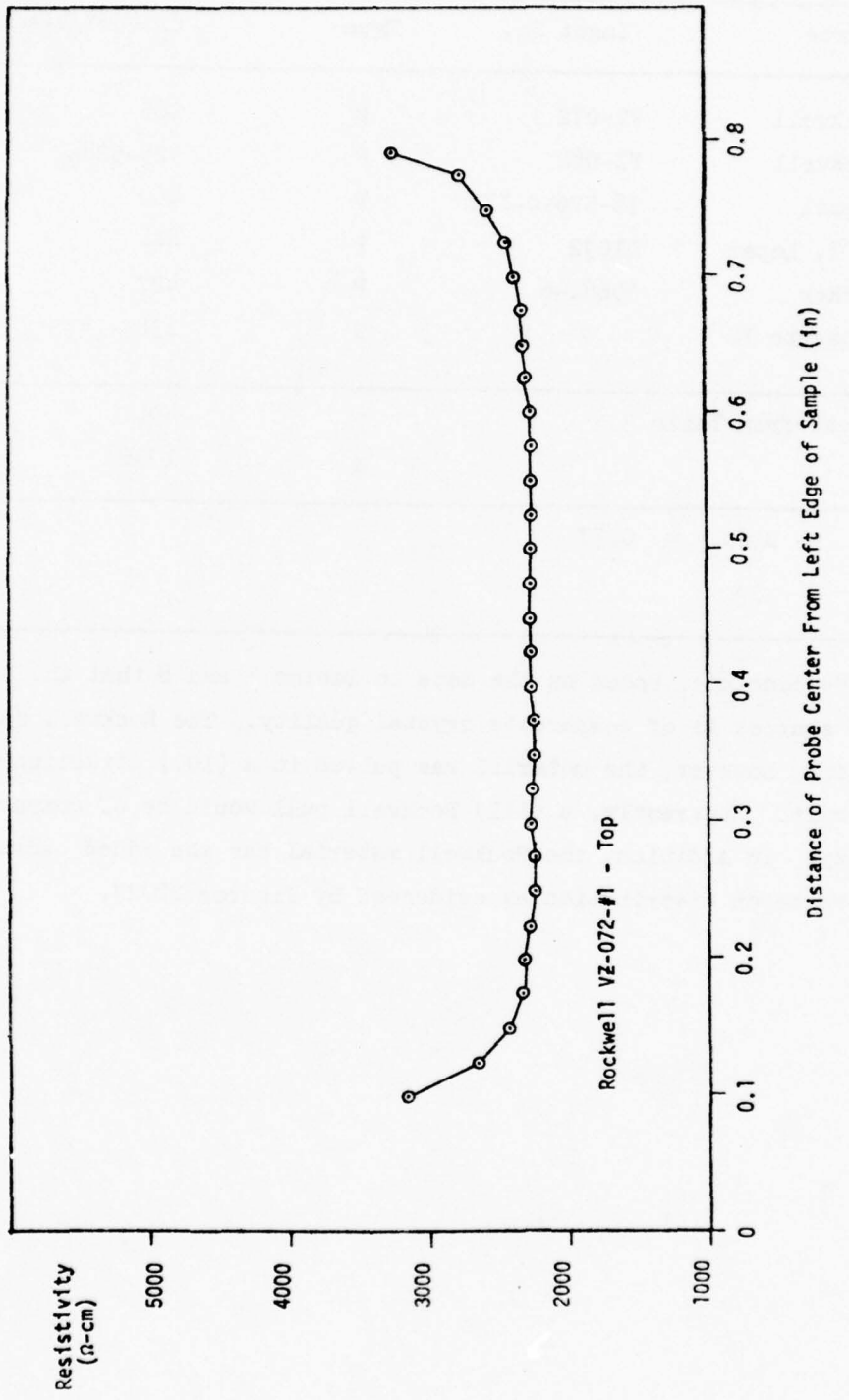


Figure 22. Radial resistivity of VZ-072-1-top.

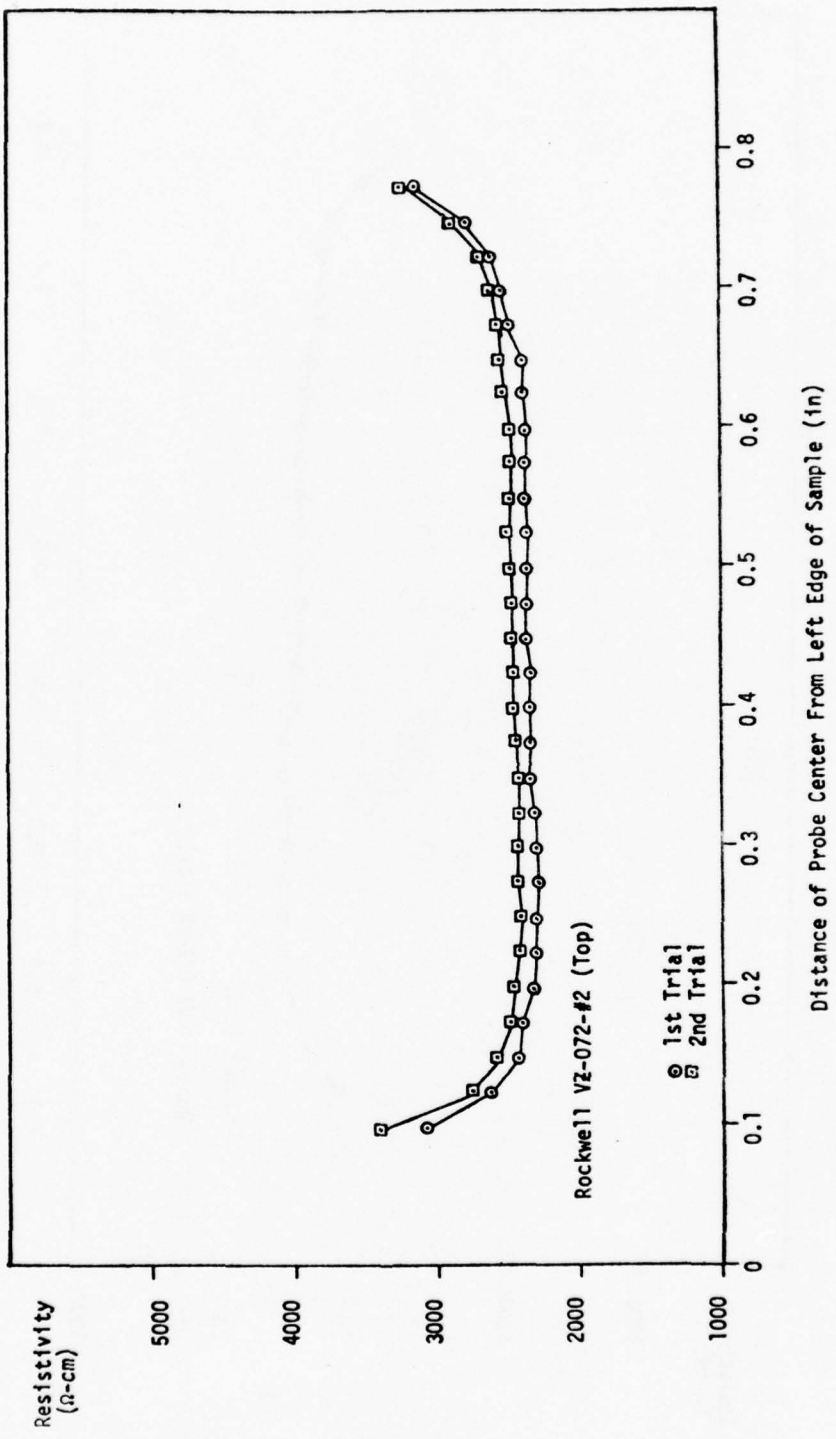


Figure 23. Radial resistivity of VZ-072-2-top.

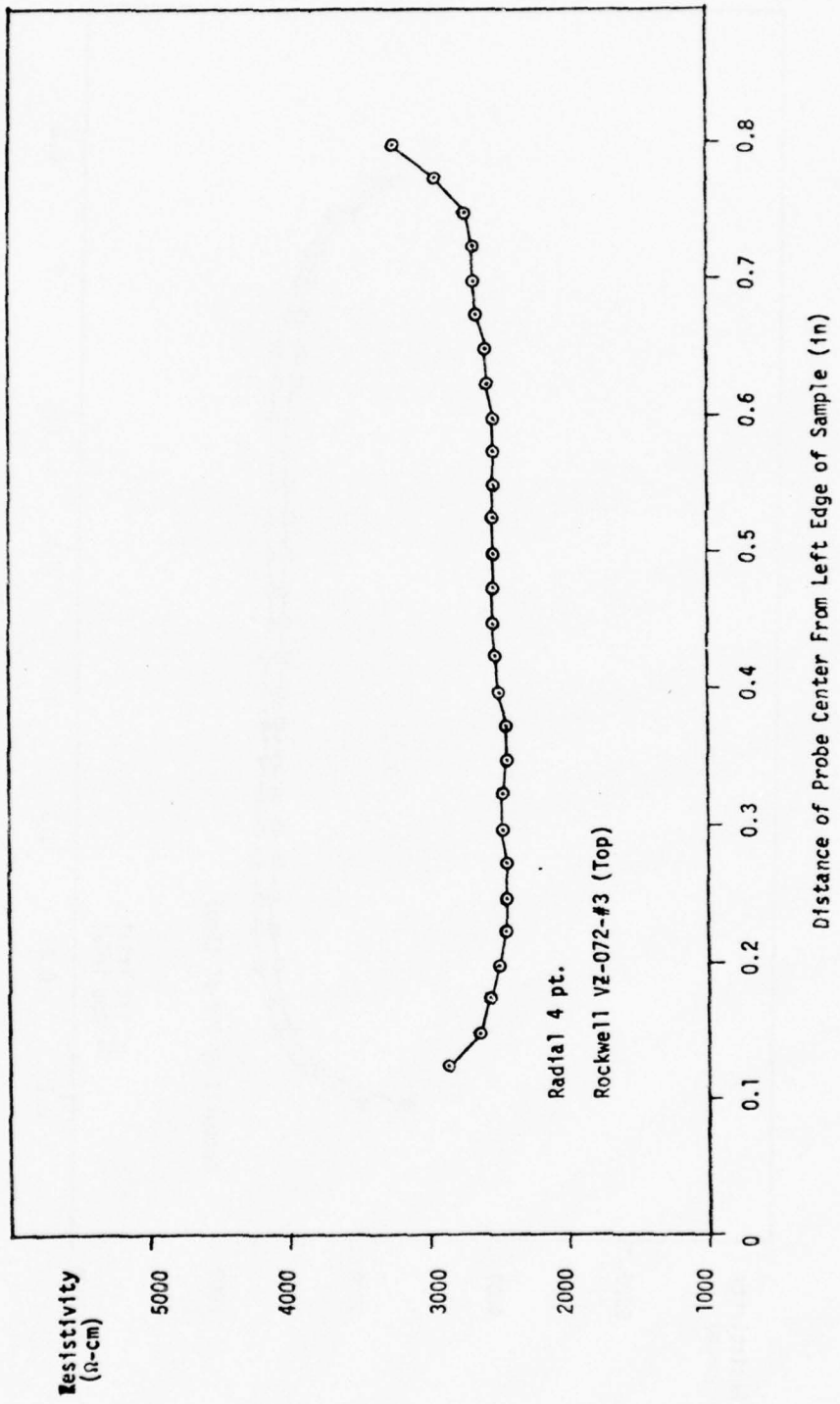


Figure 24. Radial resistivity of VZ-072-3-top.

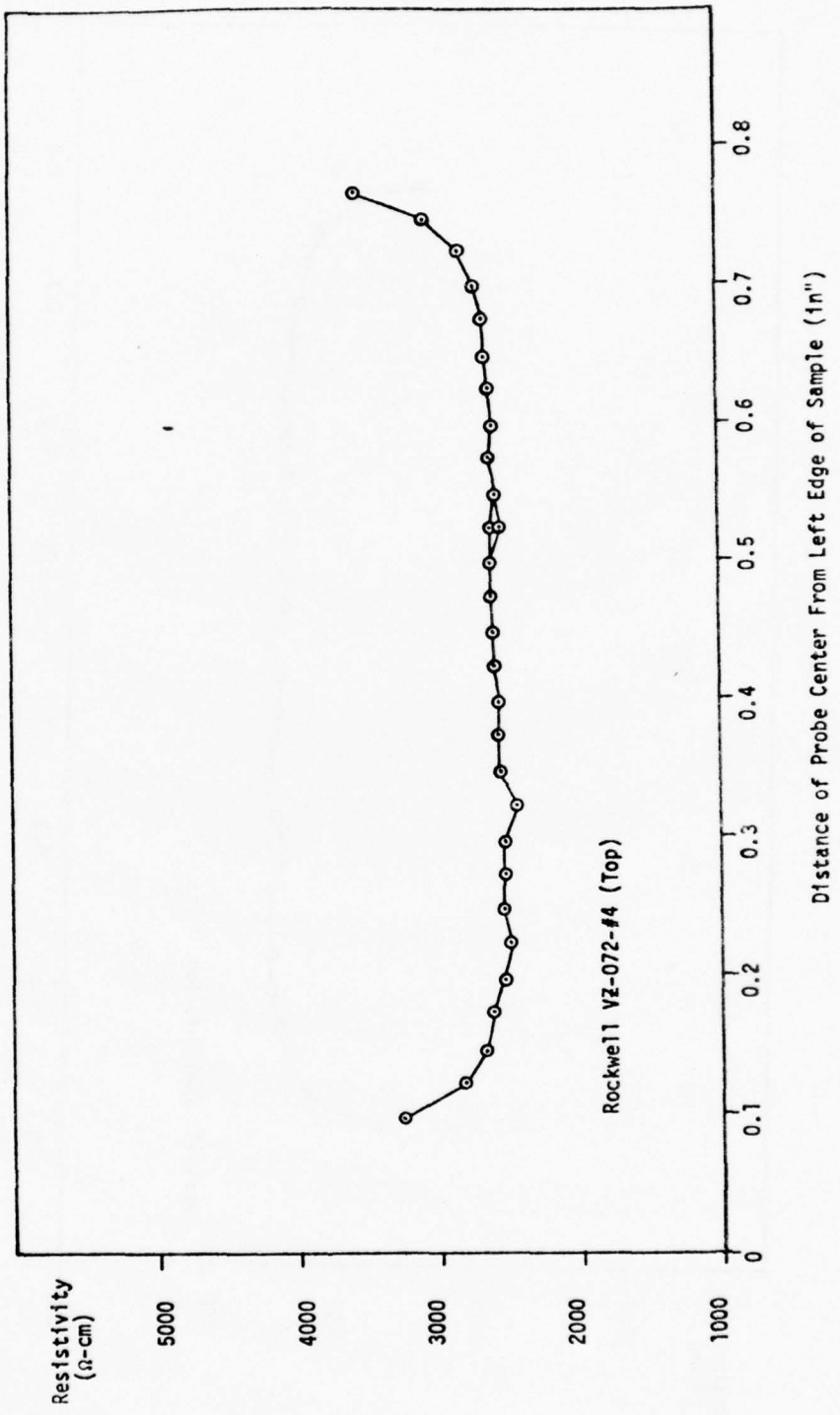


Figure 25. Radial resistivity of VZ-072-4-top.

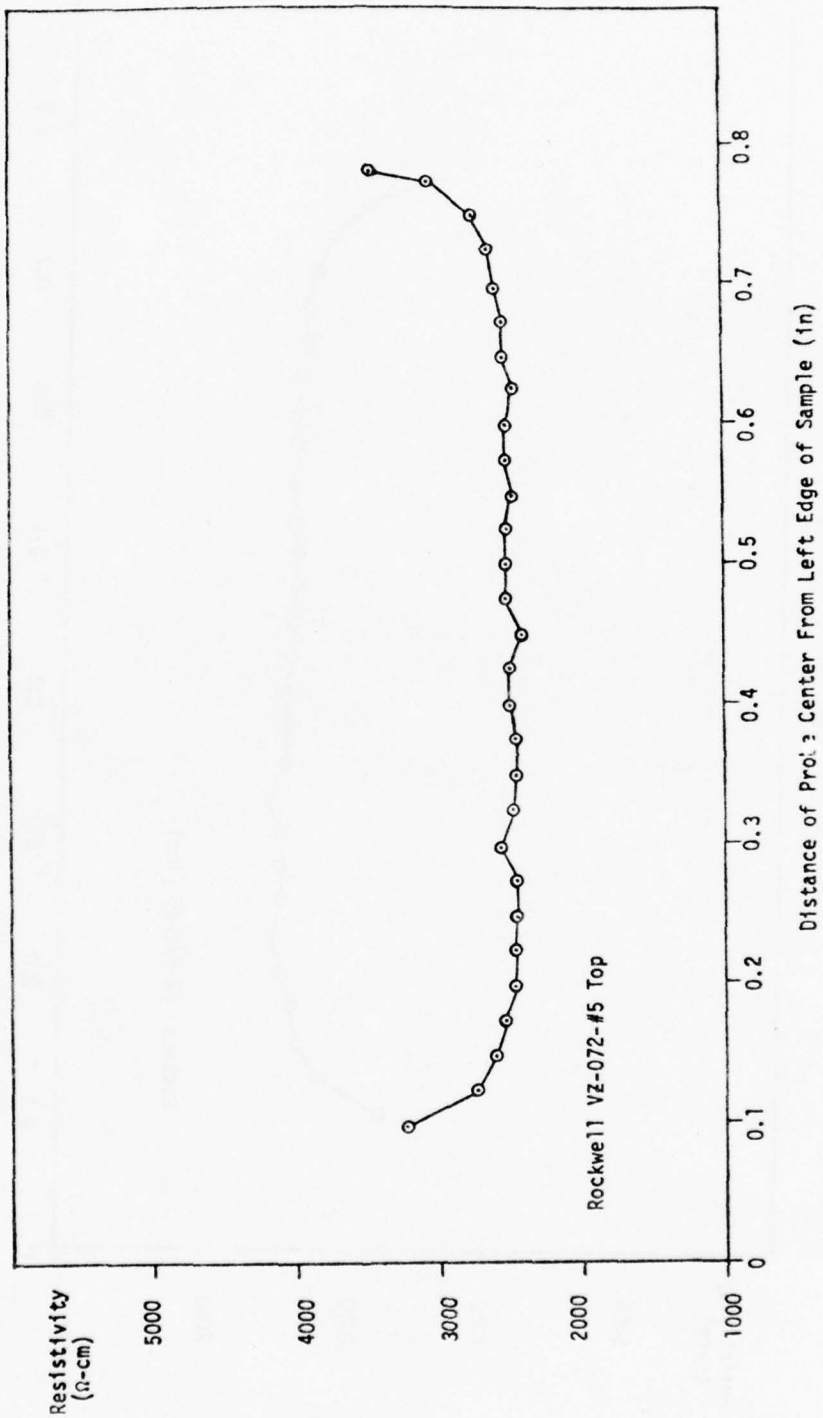


Figure 26. Radial resistivity of VZ-072-5-top.

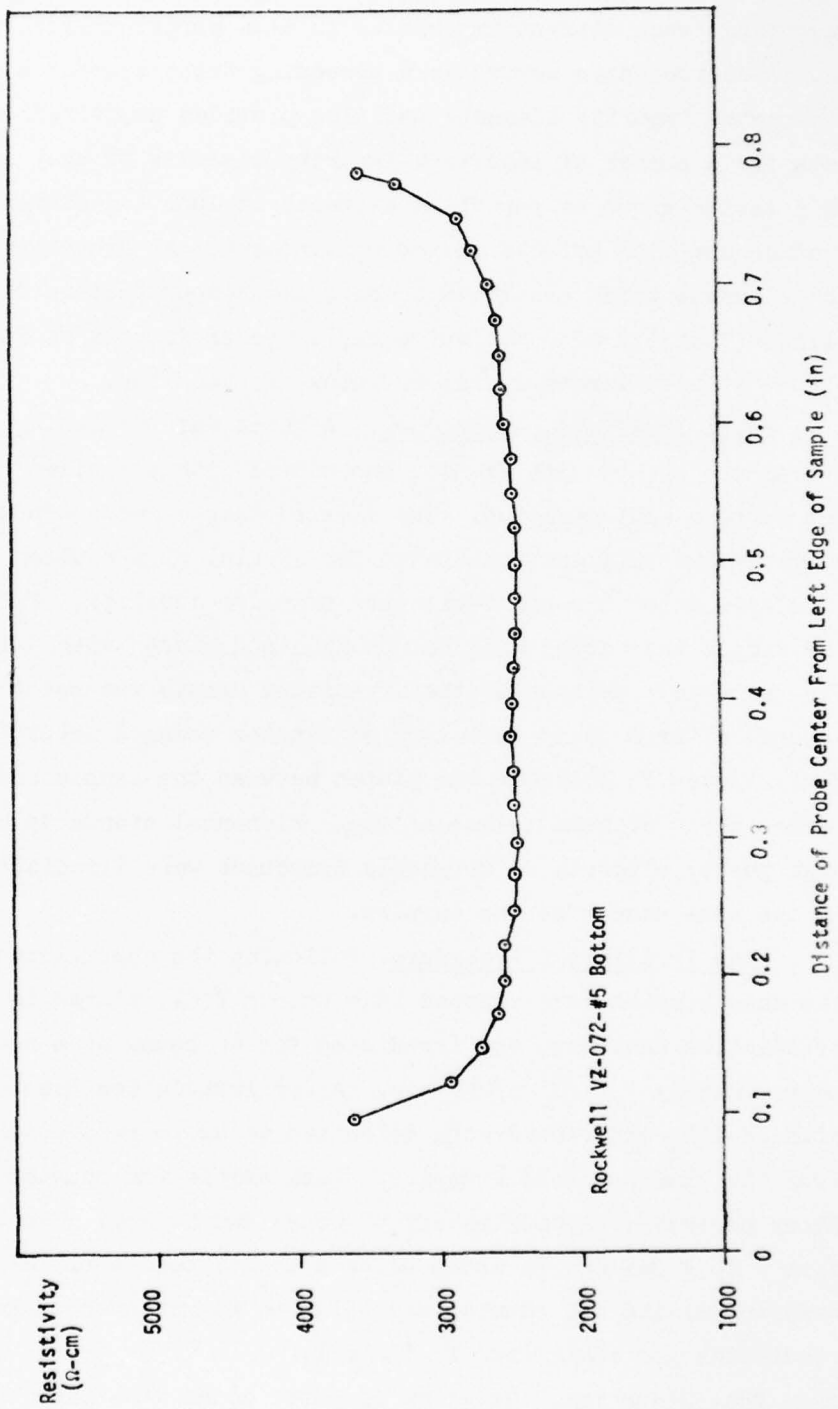


Figure 27. Radial resistivity of VZ-072-5-bottom.

B. Neutron Activation Analysis

An instrumental neutron activation analysis (INAA) procedure for measuring trace element impurities in high purity silicon was established. This INAA procedure serves as a screening technique for a wide variety of unexpected impurity elements and also provides quantitative upper limit data for a number of important impurity elements if they are not observed. This latter group of important elements include (a) elements known to produce striking effects on the physico-chemical properties of silicon, (b) elements which are known to be common impurities in technical grade silicon, and (c) elements which may serve as indicators for contamination of the silicon ingots during refining and handling.

Short Irradiation Procedure. A thick wafer weighing approximately 1 gram was etched with HF-HNO_3 and rinsed with deionized water to remove any surface contamination. The cleaned sample was wrapped in a precleaned polyethylene bag, and irradiated for 20 min. at a neutron flux of 8×10^{13} n/cm^2-sec using the pneumatic tube transfer facility. Following irradiation the sample was washed with hot 8N HNO_3 and rinsed with deionized water. The gamma-ray spectrum of the irradiated sample was recorded for 2000 seconds after a decay period of 60 minutes using a Ge(Li) detector. A 3 millimeter Pb absorber was placed between the sample and detector to reduce the ^{31}Si beta bremstrahlung. Elemental standards prepared from high purity elements or weighable compounds were irradiated and counted in the same manner as the samples.

Long Irradiation Procedure. Following the short irradiation procedure, the same samples were wrapped in aluminum foil, placed in a reflector irradiation canister, and irradiated for 40 hours at a neutron flux of approximately 1×10^{14} n/cm^2-sec. After irradiation the samples were etched with HF-HNO_3 and rinsed with deionized water to remove surface contamination from the aluminum foil wrapping. Each sample was counted for 2000 sec after decay periods of approximately 40 hours and 5 days. The gamma-ray spectra from 0 to 4 MeV was recorded using a Ge(Li) detector. Elemental standards were irradiated and counted according to the same schedule. The analytical conditions are summarized in Table 1.

Data Reduction. Existing computer codes were used to reduce the gamma-ray spectral data for both samples and standards to peak energies and peak areas for all observed gamma-rays. Isotope assignments were

based on calculated energies and, where necessary, half-life measurements. Elemental concentrations for observed impurities were calculated by comparison of sample and standard peak areas after proper normalization of differences in irradiation exposure and decay time, if necessary. Minimum detectable peak areas for isotopes not observed were estimated as three times the statistical deviation of the spectral base line in the peak region. Detection limits for the elements measured are given in Table 9 for a 1 gram silicon sample using a value of 2.34 gm/c.c. for the density of silicon.

Results. Silicon ingots obtained from four different suppliers were analyzed. Elemental concentration values are given in Table 10 as atoms of impurity per c.c. of silicon assuming that the impurity is homogeneous in the matrix. The values given for sodium probably represent surface contamination derived from the ^{27}Al (n, α) ^{24}Na reaction occurring in the aluminum foil encapsulation.

Figure 28 illustrates a sawing contamination which was detected on VZ-072. This sample was cut on a glass cut-off tool outside our laboratories. It is apparent that gold surface contamination was present and was difficult to remove by etching. The etching procedure apparently tends to selectively etch around the gold spots and undercut until the gold is removed.

TABLE 9. Summary of Analytical Conditions and Detection Limits for Neutron Activation Analysis of Silicon

Element	Isotope	Eγ(keV)	Half-life	Detection Limit* (atoms/cc)
	20 min. Irradiation - 60 min. Decay - 2000 sec Count			
In	^{116m}In	1293.1		1×10^{11}
Mn	^{56}Mn	1812		1.5×10^{12}
	40 hour Irradiation - 40 hour Decay - 2000 sec Count			
Mo	^{99}Mo	140.6	66.6 h	4×10^{12}
Cu	^{64}Cu	511	12.75 h	7×10^{11}
Ga	^{72}Ga	834.1	14.1 h	3×10^{11}
Au	^{198}Au	411.8	64.7 h	2×10^{9}
W	^{187}W	685.7	23.9 h	1×10^{11}
As	^{76}As	559.2	26.4 h	1×10^{11}
Sb	^{122}Sb	564	65.8 h	6×10^{10}
Yb	^{175}Yb	396.1	101 h	8×10^{10}
Na	^{24}Na	1368.4	15.0 h	2×10^{12}
Eu	^{152m}Eu	841.6	9.3 h	5×10^{10}
	40 hour Irradiation - 5 day decay - 2000 sec Count			
Cr	^{51}Cr	320.0	27.8 d	9×10^{12}
Th	^{233}Pa	311.8	27.0 d	1.5×10^{11}
Sc	^{46}Sc	889.4	83.8 d	1.5×10^{11}
Hf	^{181}Hf	482.0	42.4 d	3×10^{11}
Co	^{60}Co	1173.1	5.25 y	8×10^{12}
Ag	^{110m}Ag	657.8	253 d	3×10^{12}
Ta	^{182}Ta	1121.2	115 d	1.5×10^{12}

*3σ detection limit estimated for a 1 gram sample assuming a density value of 2.34 grams/c.c. for silicon.

TABLE 10. Elemental Concentrations Measured in Four Silicon Ingots

	Impurity level measured in atoms of impurity/c.c.*			
Element	Rockwell VZ-072	Topsil 36-520	Wackers 30661-6	TI Lopex L1092
In	n.d.	n.d.	n.d.	n.d.
Mn	n.d.	$\sim 2 \times 10^{12}$	n.d.	n.d.
Mo	$\sim 4 \times 10^{12}$	n.d.	n.d.	n.d.
Cu	2.9×10^{12}	$\sim 7 \times 10^{11}$	1.1×10^{12}	1.3×10^{12}
Ga	n.d.	n.d.	n.d.	n.d.
Au	4.7×10^{9}	n.d.	5.3×10^{9}	$\sim 3 \times 10^{9}$
W	n.d.	n.d.	n.d.	n.d.
As	n.d.	n.d.	n.d.	n.d.
Sb	n.d.	n.d.	n.d.	n.d.
Yb	n.d.	n.d.	n.d.	n.d.
Na	8.9×10^{13}	2.0×10^{13}	1.8×10^{13}	1.9×10^{13}
Eu	n.d.	n.d.	n.d.	n.d.
Cr	n.d.	n.d.	n.d.	n.d.
Th	n.d.	n.d.	n.d.	n.d.
Sc	n.d.	n.d.	n.d.	n.d.
Hf	n.d.	n.d.	n.d.	n.d.
Co	n.d.	n.d.	n.d.	n.d.
Ag	n.d.	n.d.	n.d.	n.d.
Ta	n.d.	n.d.	n.d.	n.d.

* n.d. indicates not detected concentrations above the background. Detection limits are given in Table 9.

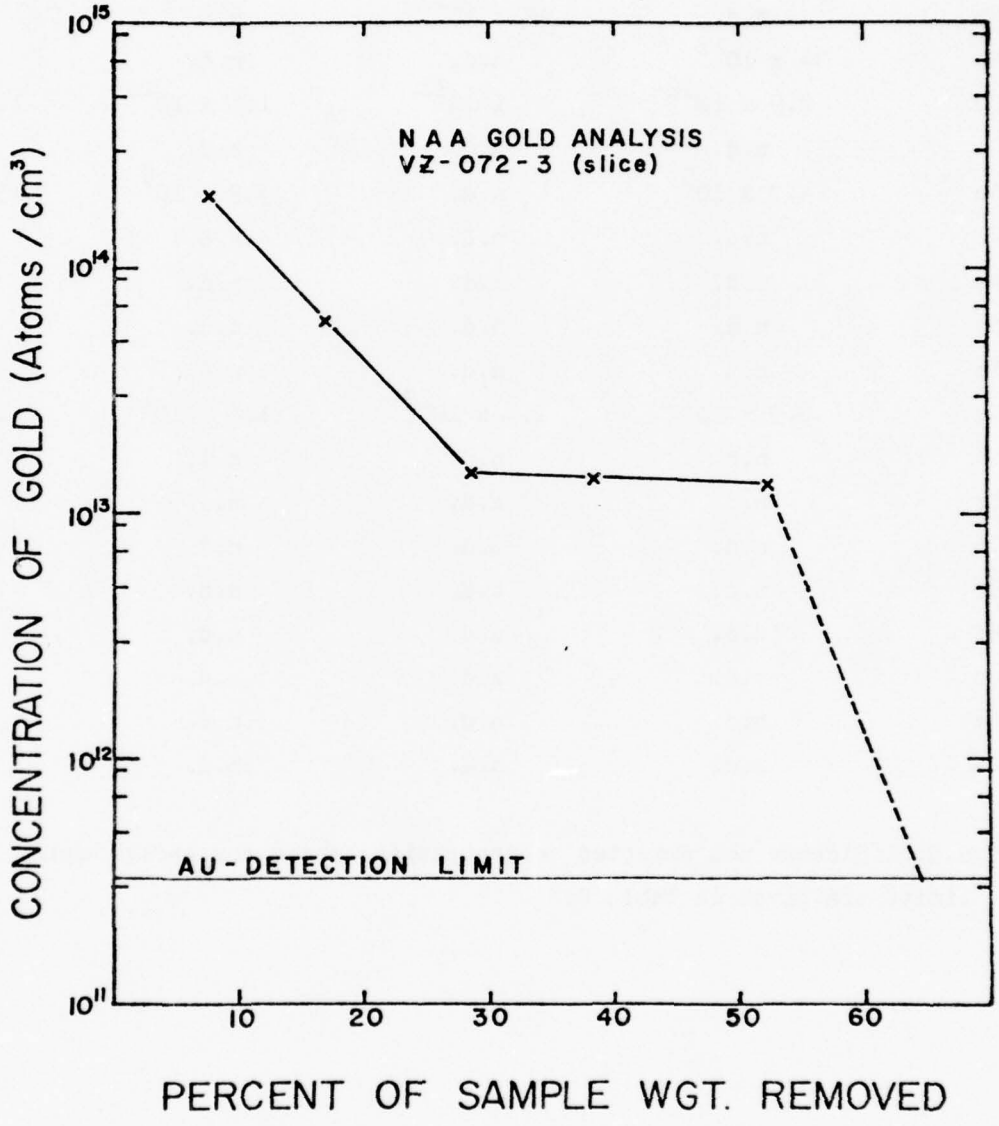


Figure 28. Concentration of gold vs. percent of sample weight removed.

C. Irradiation and Anneal Experiments

It is instructive at this point to consider the types and amounts of radiation damage which result from a typical neutron transmutation irradiation. We will consider the following sources of damage:

- Fast neutron damage for a graphite moderated neutron energy spectrum (this case will be an approximation to our sample irradiation position).
- Fast neutron damage from a fission neutron energy spectrum (this case will approximate in pile irradiations found in the literature).
- Gamma damage from fission gammas from the reactor pile.
- Gamma recoil damage (this damage occurs as a result of conservation of momentum when a gamma is emitted from an excited Si nucleus after thermal neutron capture).
- Beta recoil damage (this damage occurs as a result of conservation of momentum when the beta is emitted in the deexcitation of $^{30}Si \rightarrow {}^{31}P + \beta^-$.

We will neglect damage from (n, p), (n, α), and (γ, n) etc. , reactions because of their low cross sections for neutron energies of interest. Although (n, γ) reactions with boron have large cross sections, the boron concentration in our samples is negligible compared to the silicon concentration. Also, we estimate that the damage from the β emitted during ^{31}P production will produce about the same number of displacements as the recoil.

Although the estimates of the number of displacements due to each of these processes is very approximate, it is instructive to make a rough calculation to estimate the magnitude of each of these effects.

The number of displaced atoms per unit volume per sec is calculated from the equation

$$\frac{dN_D}{dt} = N_T \sigma \phi \nu \qquad (21)$$

where N_D is the number of displacements per unit volume, N_T the number of target atoms per unit volume, ϕ is the flux of damaging particles (# particles/ cm^2/sec) and ν is the number of displacements per incident damaging particle. We will estimate ν from the Kinchin-Pease model.[21] In this model

$$\nu(E_R) = \bar{E}_{R/2E_d} \qquad (22)$$

for $\overline{E}_R \geq 2E_d$ where $\overline{E}_R$ is the average kinetic energy of the recoiling lattice atom and E_d is the displacement threshold in silicon which we take as about 12 eV.[22] The maximum recoil kinetic energy of a target atom struct by a neutron of energy E_n is given by

$$E_R(\max) \cong \frac{4E_n}{A} \tag{23}$$

when A is the target material atomic weight.[23]

For a fission neutron spectrum, the average recoil kinetic energy is given by [23]

$$\overline{E}_R \text{ (fission neutron)} = \frac{E_R(\max)}{2} \tag{24}$$

while for a graphite moderated spectrum

$$\overline{E}_R \text{ (moderated neutron)} = \frac{1/2\ E_R(\max)}{\ln\left[\frac{E_R(\max)}{E_d}\right]} \tag{25}$$

We shall assume that the average neutron energy to be used in equation (23) is 1.5 MeV. Then we find from (23), (24), and (25) that

$$E_R(\max) = \frac{4(1.5\text{ MeV})}{28} = 214\text{ keV},$$

$$\overline{E}_R \text{ (fission neutron)} = \frac{214\text{ keV}}{2} = 107\text{ keV}$$

and

$$\overline{E}_R \text{ (moderated neutron)} = \frac{1/2(214\text{ keV})}{\ln\left[\frac{214 \times 10^3\text{ eV}}{12\text{ eV}}\right]} = 10.9\text{ keV}.$$

We find, using (22), that the number of displacements per neutron is much higher for a fission spectrum than for a moderated spectrum, i.e.,

$$\nu \text{ (fission)} = \frac{107\text{ keV}}{2(12\text{ eV})} = 4458\text{ displacements/neutron} \tag{26}$$

and

$$\nu \text{ (moderated)} = \frac{10.9\text{ keV}}{2(2\text{ eV})} = 455\text{ displacements/neutron.} \tag{27}$$

Furthermore, in our bulk pool facility, assuming a Cd ratio of about 30:1, the fast flux is about $(5 \times 10^{11}\text{n/cm}^2\text{/sec})/30 = 1.67 \times 10^{10}\text{n/cm}^2\text{/sec}$. For an in-core irradiation, the Cd ratio is about 1:1 and a typical fast flux is, therefore, $5 \times 10^{13}\text{n/cm}^2\text{/sec}$. Using these fluxes and assuming that the displacement cross section is approximately equal to the scattering cross section[23], which we will assume is $3 \times 10^{-24}\text{cm}^2$, we find using (21) and (26)

$$\frac{dN_D}{dt}\text{(fast neutron in core)} = (5 \times 10^{22})(3 \times 10^{-24})(4458)(5 \times 10^{13})$$

$$= 3.35 \times 10^{16} \text{ displacements/cm}^3\text{/sec.} \quad (28)$$

Using (21) and (27) we find also that

$$\frac{dN_D}{dt}\text{(fast neutron in pool)} = (5 \times 10^{22})(3 \times 10^{-24})(455)(1.67 \times 10^{10})$$

$$= 1.14 \times 10^{12} \text{ displacements/cm}^3\text{/sec.} \quad (29)$$

The gamma flux radiation damage is also quite different since in core the photon flux is about 3×10^6R/sec while in our bulk pool facility it is about 3×10^2R/sec. The cross section, $\sigma(\gamma)$, for displacements is dominated by Compton electron displacements and is nearly independent of photon energy in silicon for typical fission gamma energies.[23, 24] We will assume that this cross section is about 1×10^{-25}cm^2 for 100 keV < E_γ < 2 MeV and that 1 R/sec = 2×10^9 1 MeV photons/cm^2/sec.[25] Then the number of displacements is

$$\frac{dN_D}{dt}\text{ (gamma in pile)} = (5 \times 10^{22})(1 \times 10^{-25})(3 \times 10^6)(2 \times 10^9) \quad (30)$$

$$= 3 \times 10^{13} \text{ displacements/cm}^3\text{/sec}$$

and

$$\frac{dN_D}{dt}\text{ (gamma bulk pool)} = (5 \times 10^{22})(1 \times 10^{-25})(3 \times 10^2)(2 \times 10^9)$$

$$= 3 \times 10^9 \text{ displacements/cm}^3\text{/sec.} \quad (31)$$

The various silicon isotopes after thermal neutron absorption relax from excited states by prompt gamma emission. This imparts a recoil to the silicon isotope in order to conserve momentum. Since

$$p = \frac{E\gamma}{C} \equiv MV,$$

$$E_R = 1/2MV^2 = 1/2 \frac{E\gamma^2}{MC^2} .$$

An average over all silicon isotopes and cross seetions yields an average recoil kinetic energy of 780 eV.[26, 27] Therefore, using (22), we find

$$\bar{\nu} = \frac{780 \text{ eV}}{2(12 \text{ eV})} = 32.5 \text{ displacements/thermal neutron.}$$

The average cross section for these processes[27] is $1.3 \times 10^{-25} cm^2$ and the flux of interest is the thermal neutron flux, therefore

$$\frac{dN_D}{dt} \quad (\gamma\text{-recoil in core}) = (5 \times 10^{22})(1.3 \times 10^{-25})(5 \times 10^{13})(32.5)$$
$$= 1.06 \times 10^{13} \text{ displacements/cm}^3\text{/sec} \quad (32)$$

and

$$\frac{dN_D}{dt} \quad (\gamma\text{-recoil in pool}) = (5 \times 10^{22})(1.3 \times 10^{-25})(5 \times 10^{11})(32.5)$$
$$= 1.06 \times 10^{11} \text{ displacements/cm}^3\text{/sec.} \quad (33)$$

A similar procedure can be applied to beta decay recoil. Assuming the beta energy to be $E_\beta = 1.5$ MeV, and using conservation of momentum, we find

$$P = \frac{\sqrt{E_\beta^2 - (m_o c^2)^2}}{C} = MV$$

$$\overline{E}_R = 1/2MV^2 = 1/2 \quad \frac{E_\beta^2 - (m_o c^2)^2}{MC^2} = 33.2 \text{ eV.}$$

Therefore, using (22),

$$\nu = \frac{33.2 \text{ eV}}{2(12 \text{ eV})} = 2.76 \text{ displacements/neutron absorbed.}$$

Since this occurs for only 3% of the total silicon atoms, with a cross section of $1.1 \times 10^{-25} cm^2$,

$$\frac{dN_D}{dt} \quad (\beta \text{ recoil in core}) = (0.03)(5 \times 10^{22})(1.1 \times 10^{-25})(5 \times 10^{13})(2.76)$$
$$= 2.3 \times 10^{10} \text{ displacements/cm}^3\text{/sec} \quad (34)$$

and

$$\frac{dN_D}{dt} (\beta \text{ recoil in pool}) = (0.03)(5 \times 10^{22})(1.1 \times 10^{-25})(5 \times 10^{11})(2.76)$$
$$= 2.3 \times 10^{8} \text{ displacements/cm}^3\text{/sec.} \quad (35)$$

These numbers must be compared with the rate of producing phosphorus atoms which is

$$\frac{dN_P}{dt} (\text{in core}) = (0.03)(5 \times 10^{22})(1.1 \times 10^{-25})(5 \times 10^{13})$$
$$= 8.25 \times 10^{9} \text{ [P]/cm}^3\text{/sec.} \quad (36)$$

and

$$\frac{dN_P}{dt} \text{ (in pool)} = (0.03)(5 \times 10^{22})(1.1 \times 10^{-25})(5 \times 10^{11})$$

$$= 8.25 \times 10^{7} \text{ [P]/cm}^3\text{/sec.} \qquad (37)$$

We can now compare the number of displacements per phosphorus atom produced by each of these mechanisms. This information is summarized in Table 11.

Although these calculations are quite speculative, several differences between in-core (low Cd ratio) and in-pool (high Cd ratio) irradiations become apparent. It is clear that the fission gamma and beta recoil damage is point-defect like. The annealing characteristics of this damage should be similar to 1 Mev electron irradiation data. It is also clear that the gamma recoil damage is a significant fraction of the radiation damage for in-pool irradiations but is relatively less significant for in-core irradiations.

Chukichev and Vavilov have estimated experimentally that the number of gamma recoil displacements is about equal to the number of fast neutron displacements in a heavy water moderated reactor.[27] Our ratio of fast neutron to gamma recoil displacements is of the order of 10:1 for an in-pool position with a Cd ratio of 30:1. Since the Cd ratio in a heavy water reactor is between 100:1 to 1000:1, our calculations are in reasonable agreement with the experimental data in Ref. 27.

It is not clear whether to treat the gamma recoil radiation damage as point defect like or cluster like. The average number of displacements per neutron is rather large (32.5 displacements/thermal neutron) and suggests at least the production of small clusters. The actual number of displacements per thermal neutron absorbed, however, range from about 10 or 20 up to 80 to 160. There is, therefore, a continuous distribution of cluster sizes which approach the point defect distributions at the lower end. The same cluster size arguments can be made about fast neutron damage from a highly moderated energy spectrum.

We have considered gamma recoil damage both as cluster like and point defect like in Table 11, to calculate the ratio of cluster like displacements to point defect like displacements for our two cases of interest. It seems likely that the in-core irradiations deposit 300 to 3000 more displacements in clusters than in point defects as compared to in-pool

TABLE 11. Number of Displacements per Phosphorus Produced

Position → / Damage Particle ↓	In Core $\phi_{th} = 5 \times 10^{13} n/cm^2 sec$ Cd ratio = 1:1	In Pool $\phi_{th} = 5 \times 10^{11} n/cm^2/sec$ Cd ratio = 30:1
Fast Neutron	4.06×10^6	1.38×10^4
Fission Gamma	1.0	36.4
Gamma Recoil	1.29×10^3	1.29×10^3
Beta Recoil	2.76	2.76
Total Disp./ [P]	4.06×10^6	1.51×10^4
Cluster/Pt. Defect Ratio:		
(If gamma recoil = cluster)	3140	10.4
(If gamma recoil = pt. defect)	1.08×10^6	385

Ratio of Core to Pool Cluster to Pt. Defect Ratios:	
(Gamma recoil = cluster)	302
(Gamma recoil = pt. defect)	2805

irradiations. Such a large difference in the defect spectrum is very likely to produce differences in annealing characteristics for the two cases. We will discuss some of these differences in the following discussion on annealing.

Table 12 is a summary of all the irradiations performed thus far, the sample number, the fluence, the phosphorus concentration calculated from the cross section, and initial resistivity assuming a typical mobility, and the purpose of the irradiation. In this table, Φ_C is the fluence required to take the particular p-type sample from its initial resistivity to intrinsic (or exact compensation of the residual boron by the phosphorus added). An inspection of this table shows immediately the failure to control the resistivity for partial compensation on the p-type side of intrinsic (i.e. $\Phi < \Phi_C$) due to premature type conversion.

Figure 29 shows this premature type conversion effect. This figure compares an isochronal anneal in argon of a wafer of Rockwell float zone, MURR 1, with the annealing in air of a piece of Monsanto Czochralski, and vacuum anneals of float zone and Czochralski by Kharchenko et al.[28,29] The solid bar is the expected p-type resistivity for the Rockwell float zone after the final anneal on the basis of the number of donors added [0.042 ppb]. Instead the final resistivity is about 400 Ω-cm n-type (the type conversion probably occurred between 600 and 800°C) a gain of extra donors of 0.282 ppb (1.41×10^{13} atoms/cm^3) beyond that added by neutron doping [0.042 ppb].

Also shown on this figure is the isochronal annealing of a second unirradiated Rockwell sample from the same wafer. It should be noted that the unirradiated sample shows no adverse effects of the annealing and that the resistivity of the irradiated sample MURR 1 drops below that of the unirradiated sample at 300°C.

The heavily irradiated float zone sample by Kharchenko shows no type conversion peaks, i.e., no rise in resistivity toward intrinsic (230,000 Ω-cm). This is confirmed by their Hall measurements directly after irradiation but before annealing.[29] It should be noted that a drafting error has apparently been made in Figure 1 of Ref. 29 since the final values of $n = 5 \times 10^{13}$cm^{-3} and $\rho = 1$ Ω-cm imply an electron mobility of 125,000 cm^2/V-sec, some two orders of magnitude too high!

TABLE 12. Summary of Irradiations

Irrad. No.	Sample No.	Position	Integrator Counts	Fluence (n/cm^2) Theoretical [P] Added	Purpose/Result
1	Monsanto FZ ρ_o = 749Ω-cm p-type	RSAF 12-16	Counts not recorded (operator error)	$\sim 1.26 \times 10^{16}$ [0.042 ppb]	Calibration of integrator/30 min anneal at 745°C, ρ_f = 763.5 Ω-cm p-type
1A	"	I-2 (wrong position, operator error)			2nd irradiation of previous sample
2A	MURR 1 Rockwell	RSAF 12-16	7000	1.298×10^{16} (fluxwire) [0.0435 ppb]	$\Phi = 0.54\ \Phi_c$ (Φ_c = fluence needed to intrinsic) Argon isochronal anneal - type converted
2B	MURR 2 Rockwell	"	7000	1.315×10^{16} (fluxwire) [0.0441 ppb]	$\Phi = 0.5\ \Phi_c$ Vacuum isochronal anneal type converted
3	MURR 7 Rockwell	"	? can floated	0.931×10^{16} (fluxwire) [0.0313 ppb]	$\Phi \tilde{=} 0.5\ \Phi_c$, argon isochronal anneal to measure minority carrier lifetime
4	MURR 8 Rockwell	"	2181	4.004×10^{15} [0.0134 ppb]	$\Phi \tilde{=} 0.4\ \Phi_c$, argon anneal type converted
5	MURR 9 Rockwell	"	2144	3.363×10^{15} [0.0113 ppb]	$\Phi = 0.366\ \Phi_c$, activation analysis
7	Fluxwires	"	2000	3.733×10^{15}	Comparison of NBS and Cohn flux wires
8A	MURR 16 Topsil	"	3899	6.116×10^{15} [0.0205 ppb]	$\Phi = 0.384\ \Phi_c$, argon anneal type converted
8B	MURR 18 T.I.	"	3899	6.116×10^{15} [0.0205 ppb]	$\Phi = 0.373\ \Phi_c$, argon anneal type converted
9A	MURR 19 Topsil	"	3899	6.116×10^{15} [0.0205 ppb]	$\Phi = 0.400\ \Phi_c$, vacuum anneal type converted

TABLE 12. Summary of Irradiations (Cont.)

Irrad. No.	Sample No.	Position	Integrator Counts	Fluence (n/cm^2) Theoretical [P] Added	Purpose/Result
9B	MURR 20 T.I.	RSAF 12-16	3899	6.116×10^{15} [0.0205 ppb]	$\Phi = 0.421\ \Phi_c$, vacuum anneal type converted
10A	MURR 16 Topsil	I-2	6880	[0.7893 ppb]	2nd irradiation to produce 114.06 Ω-cm argon anneal, final observed value = 115.64 Ω-cm
10B	MURR 3 Rockwell	I-2	6880	[0.7893 ppb]	2nd irradiation to produce 122.84 Ω-cm argon anneal, final observed value = 134.03 Ω-cm
11	MURR 22 Wacker	RSAF 12-16	1266	1.986×10^{15} [0.00666 ppb]	$\Phi = 0.538\ \Phi_c$, vacuum annealed type converted
12	MURR 27 Topsil	"	10085	1.582×10^{16} [0.0531 ppb]	$\Phi = 1.02\ \Phi_c$, argon anneal, expected and final resistivities are equal
13	MURR-28 Monsanto FZ	I-2		Approx 20 Ω-cm(N)	n-type wafer; to check type after irradiation. (not completed)
14	MURR-30 Rockwell	RSAF 12-16	19530	Approx 1000 Ω-cm(N)	To establish limits on n-type side
15	MURR 29		6955	Approx 5000 Ω-cm(N)	To establish limits on n-type side

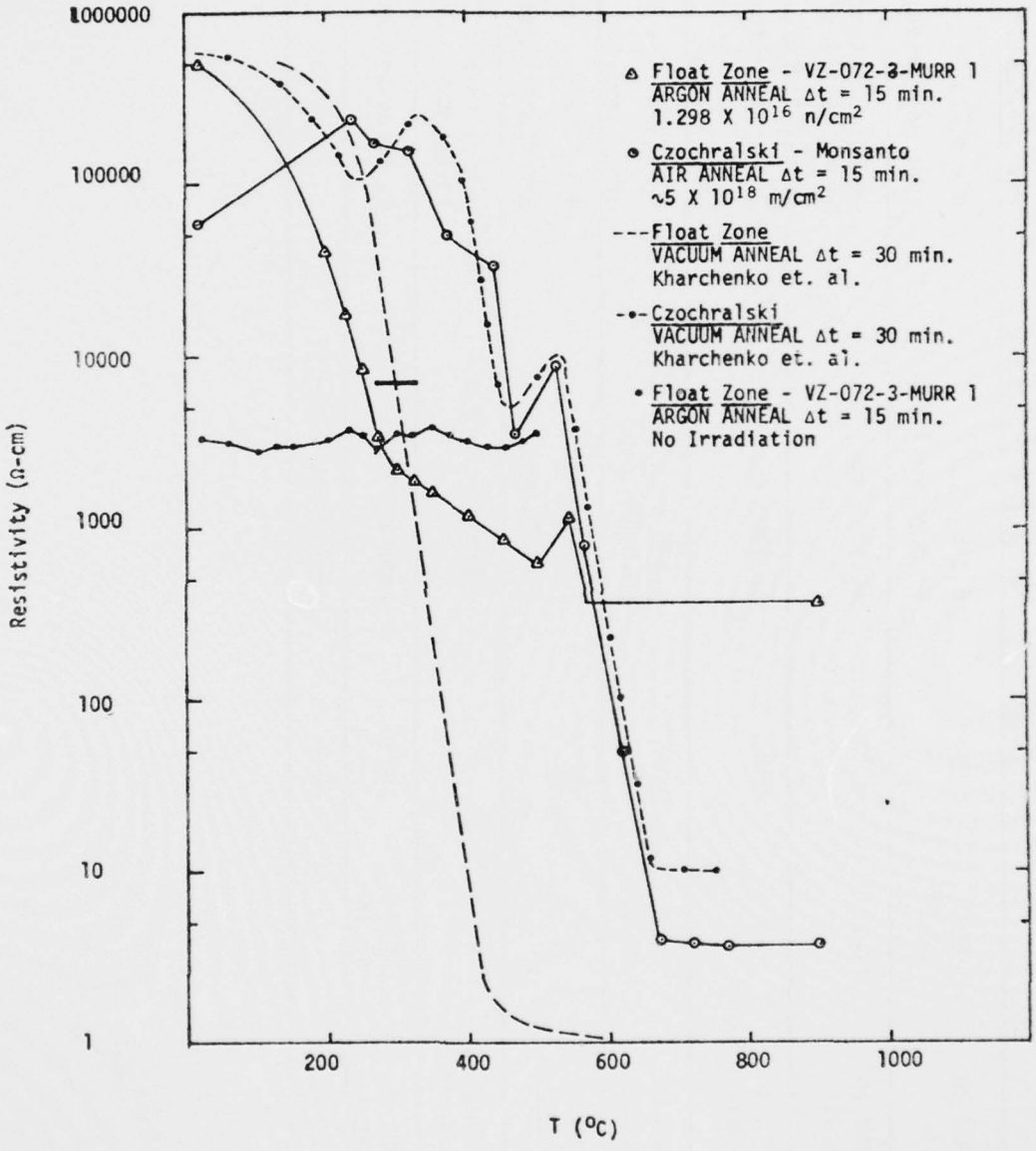


Figure 29. A comparison of isochronal annealing of transmutation doped float zone and Czochralski silicon.

Their sample was irradiated to a fluence of about $2.68 \times 10^{19} n/cm^2$ compared to the Rockwell sample fluence of $1.30 \times 10^{16} n/cm^2$. Therefore, their sample experienced a fluence of some 2000 times that of most of the samples listed in Table 12. Furthermore, their sample was irradiated in core while ours was irradiated in pool (see Table 11). Because of the fluence differences and position differences, it is estimated that the number of displacements going into clusters is 6×10^5 to 6×10^6 times greater than for our samples. The number of point defects is about 2000 times greater.

It is instructive to compare the radiation damage in the float zone sample by Kharchenko, et al. with the damage produced by a P^+ ion implanted sample. The neutron fluence for a 1 Ω-cm n-type final resistivity and 1000 Ω-cm p-type starting resistivity can be calculated from (7) to be 2.68×10^{19} n/cm^2. The number of displacements is then, using $\Phi = \phi t$, and equation (21),

$$N_D = (5 \times 10^{22})(3 \times 10^{-24})(2.68 \times 10^{19})(4458)$$

$$= 1.79 \times 10^{22} \text{ displacements/cm}^3. \qquad (37)$$

Since silicon contains only 5×10^{22} atoms/cm^3, it is clear that the radiation damage in the Kharchenko sample is approaching the amorphorus condition.

To produce an amorphorus layer by P^+ ion implantation, a dose of about 5×10^{14} ions/cm^2 at 40 keV is required.[30] The number of displacements per ion can be calculated from (22) to yield

$$\nu = \frac{E}{2E_d} = \frac{40 \text{ keV}}{2(12 \text{ eV})} = 1.666 \times 10^3 \text{ disp./ion.}$$

Since the depth of a 40 keV P^+ implant is about 2×10^{-5} cm, because of enhanced diffusion (see Figure 2.27, p. 56 in Ref. 30), the number of displacements is

$$N_d = \frac{(5 \times 10^{14} \text{ ions/cm}^2)(1.667 \times 10^3 \text{ displacements/ion})}{2 \times 10^{-5} \text{cm}}$$

$$= 4 \times 10^{22} \text{ displacements/cm}^2. \qquad (38)$$

We can conclude from a comparison of (37) and (38) that the Kharchenko

float zone sample is nearly amorphorus as a result of fast neutron damage.

This condition has interesting consequences. In ion-implanted silicon, annealing up to temperatures of about 800°C are required for complete electrical activity of the implanted ion in cases where an amorphorus layer is not formed.[31] The recovery of the electrical activity of an amorphorus layer is completed by about 600°C and is closely related to the formation of crystalline films of Si during vacuum evaporation and to epitaxial regrowth.[33]

Figure 29 also shows, for comparison, the isochronal annealing of two Czochralski silicon samples ($[O] \sim 10^{18} cm^{-3}$). The data for the Kharchenko sample is taken from Ref. 29. The reverse annealing peaks are evident in both Czochralski samples and are apparently related to the high oxygen concentration in these samples and not to neutron fluence.

Evidence for this point of view is shown in Figure 30. These float zone samples were irradiated to a fluence sufficient to produce ∿ 100 Ω-cm n-type. The expected final resistivity values calculated from the starting resistivity are shown on the figure. The Topsil sample came to within 1% of the expected donor concentration while the Rockwell sample was only slightly worse. It should be noted that the fluences for these two samples are similar to the fluences for the Czochralski samples in the previous figure, however, the annealing peaks and dips between 200 and 500°C do not appear in the float zone material at this fluence. Furthermore, dislocation density does not appear to have a direct correlation with the lack of the reverse annealing peaks shown in Figure 29 since the Rockwell sample in Figure 30 is highly dislocated while the Topsil sample is not. We conclude then, on the basis of circumstantial evidence, that the reverse annealing peaks are a result of the concentration of oxygen relative to the level of phorphorus. (The oxygen concentration is thought to be between 10^{13} to 10^{15} cm^{-3} in float zone silicon).

Kharchenko et al. also state that their Czochralski samples were p-type up to 600°C and n-type thereafter.[29] (Their Czochralski samples are apparently irradiated in-pool). We conclude from our data in Figure 30 that electrical activity of the phosphorus begins at about 600°C in agreement with their conclusions. The large reverse annealing peak from

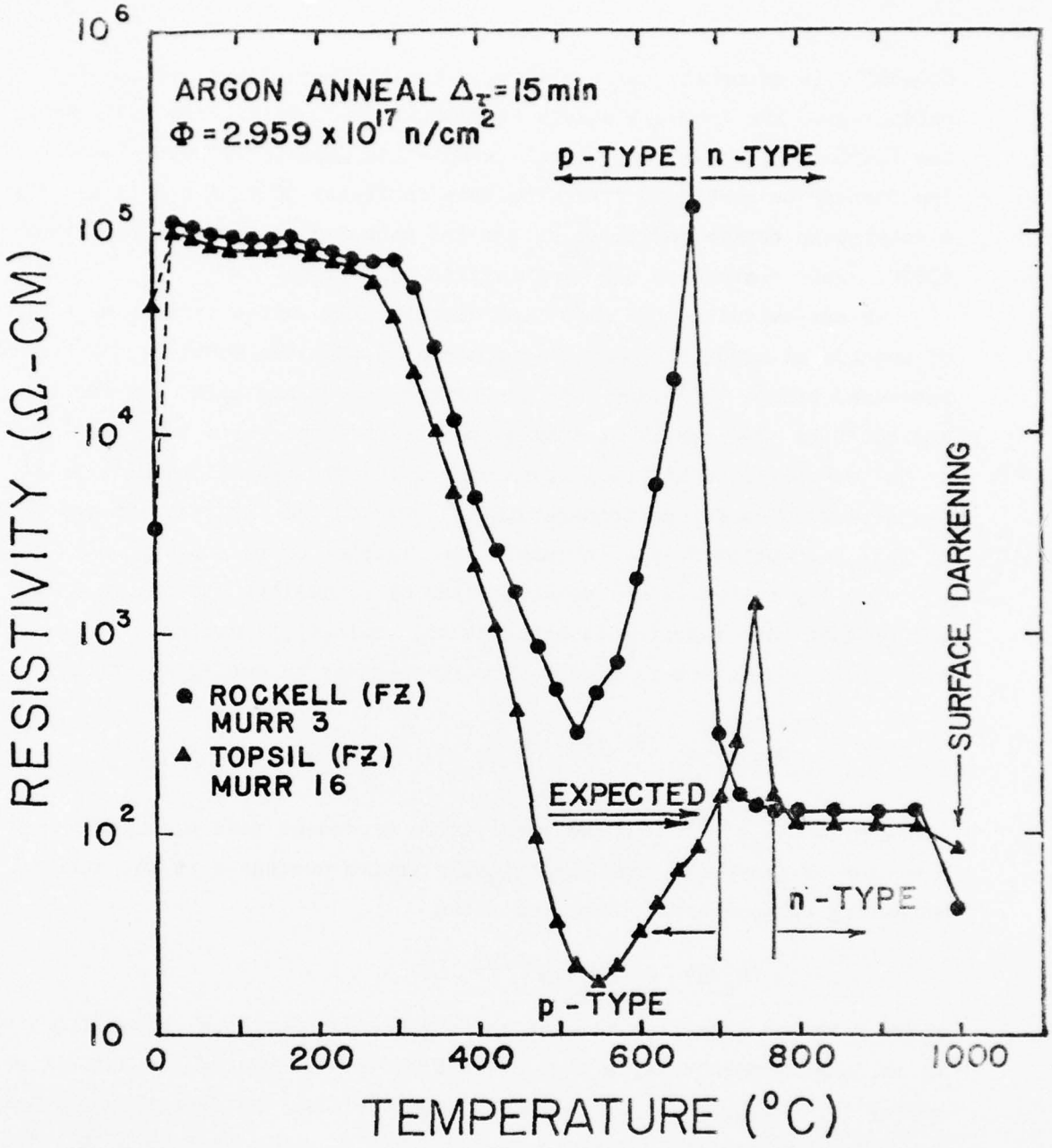


Figure 30. Isochronal annealing of two float zone samples irradiated to produce ∿100 Ω-cm N-type.

600-800°C is primarily associated with the electrical activation of phosphorus. The Rockwell sample resistivity is intrinsic at 700°C while the intrinsic peak in the Topsil sample has apparently been missed. It can further be concluded from the data in Figure 30 that nearly all the electrically active radiation damage has annealed at temperatures below 600°C. This contention can be justified as follows.

We can calculate the number of electrically active donors as a function of isochronal annealing temperature assuming that the mobility has completely recovered before 600°C and that the reverse annealing peak between 600 and 800°C is the result of a type conversion from p-type to n-type due to the electrical activation of phosphorus. (The thermal probe type as a function of annealing temperature is shown on the figure). On the basis of this assumption we can calculate the fraction of phosphorus which is not electrically active (N/N_o) as a function of annealing temperature. We assume that this fraction is unity at the resistivity minimum. Then if the electrical activation is governed by first order annealing kinetics,

$$\frac{d(N/N_o)}{dt} = -K(T)(N/N_o)$$

where $K(T) = N_o e^{-E/kT}$ is the temperature dependent rate at which the fraction of phosphorus not electrically active decreases at the various annealing temperatures. From the above

$$\ln (N_o/N) = (N_o t)e^{-E/kT}$$

where t is the annealing time at temperature T. For equal annealing times at various temperatures, a plot of $\ln N_o/N$ vs. $1/T$ yields the activation energy for the process while the intercept yields the defect jump frequency.

The result of this first order analysis is shown in Figure 31. It is clear that the first order annealing assumption is reasonable and that the first order annealing occurs throughout the type conversion peak in Figure 30. To have obtained this result, the two assumptions mentioned previously must be valid, i.e., a lack of electrically active damage at temperatures above 600° and the complete recovery of carrier mobility before 600°C.

The first order annealing analysis suggests that the activation energy

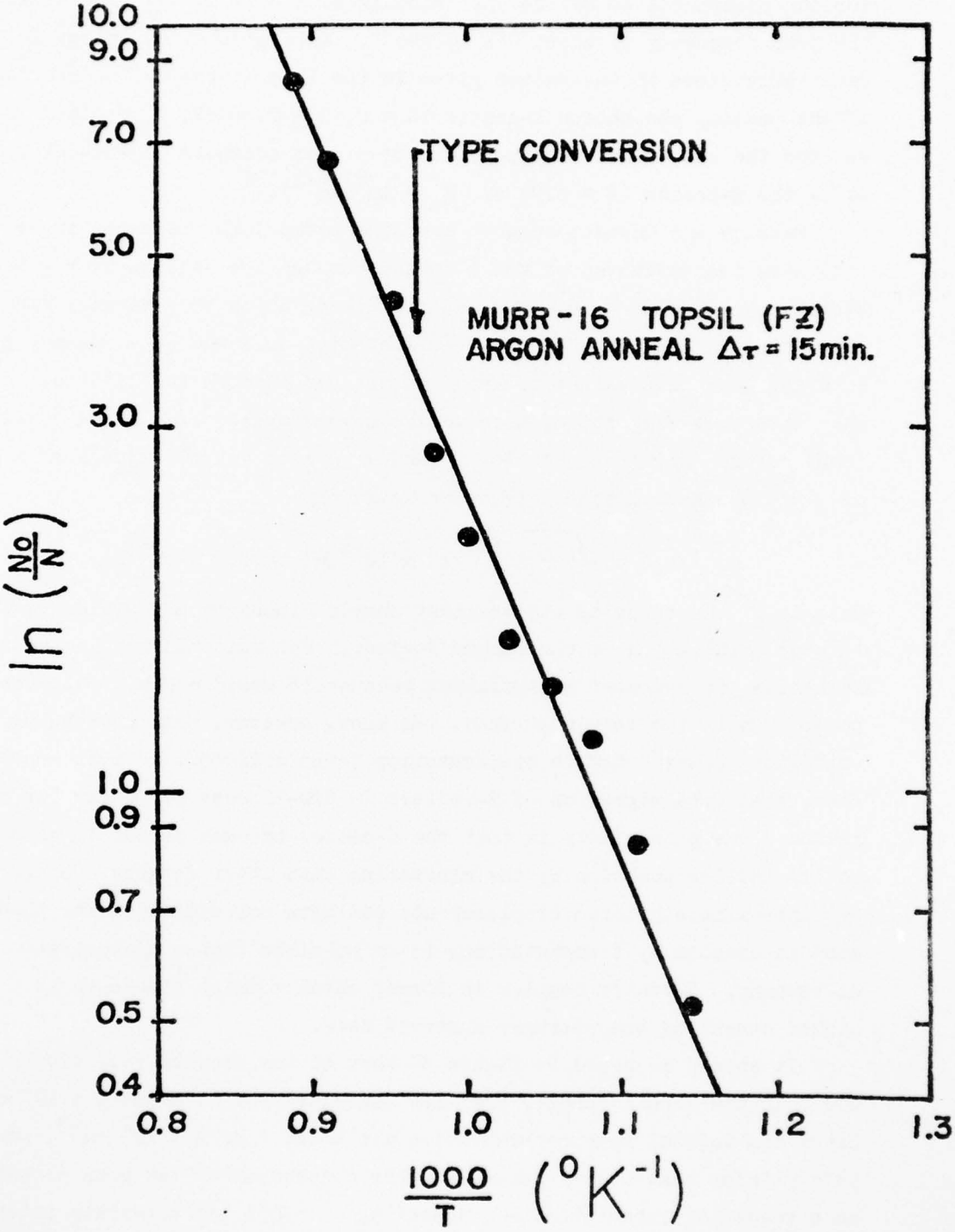


Figure 31. Semilog plot of the log of the reciprocal of the fraction of phosphorus not electrically active vs. reciprocal annealing temperature for the Topsil sample shown in Figure 30.

for the phosphorus to become electrically active is 0.96 $\pm$ 0.05 eV while the jump frequency is about $2 \times 10^{2} sec^{-1}$. This activation energy is remarkably close to the values given in the literature for the reorientation of the vacancy phosphorus E-center ($E = 0.93 \pm 0.05$ eV, $\nu_o = 1.6 \times 10^{13} sec^{-1}$)[34] and for the electrical disappearance of a deep acceptor (E_c-0.4)eV thought to be the E-center ($E = 0.94$ eV, $\nu_o = 10^{8} sec^{-1}$).[35]

Watkins and Corbett suggest that the lower jump frequency in Ref. 35 indicates the diffusion of the E-center through the lattice over great distances ($10^{13}/10^{8} = 10^{5}$ jumps before dissociation at a vacancy sink). They point out that an E-center reorientation followed by a vacancy phosphorus interchange is equivalent to an E-center jump through the lattice. If we make this same assumption, then we are observing $10^{13}/2 \times 10^{2} = 5 \times 10^{10}$ jumps before annihilation! For a random walk of 5×10^{10} jumps of a distance of $\sim$ 2Å, the mean distance traveled would be

$$L_o = \sqrt{5 \times 10^{10}} \; (2 \times 10^{-8} cm) = 4.5 \times 10^{-3} cm.$$

This is of the order of the smallest sample dimension and would suggest vacancy anihilation at the sample surface. But this can not be the correct mechanism for E-center annihilation because it would deposit all the phosphorus at the sample surface. We know, however, that phosphorus is uniformly distributed in transmutation doped silicon. We must conclude, then, that free migration of E-centers in NTD-Si does not occur for some reason. One possibility is that the E-center becomes pinned in some way to its lattice position by the clustering with other defects. Since there are approximately three displacements per beta emission when the phosphorus atom is created by transmutation, it is possible that a di-interstitial or di-vacancy, E-center complex is formed which remains stable up to the higher annealing temperatures observed here.

It should be noted in Figure 30 that at the minimum resistivity near 600°C in the Topsil sample, the hole concentration is about $6 \times 10^{14} cm^{-3}$. Since the initial hole concentration was about 2 or $3 \times 10^{11} cm^{-3}$, we can safely infer that a very large acceptor concentration has been created as a result of irradiation and annealing to 550°C (an alternate interpretation would be the destruction of $6 \times 10^{14} cm^{-3}$ donors but this would imply a

compensation ratio of 0.9996 before irradiation which is very unlikely).

It will be shown shortly that similar acceptor defect concentrations have been observed in all float zone studied to date and that this defect concentration is independent of irradiation fluence over a fluence range of 50:1. We conclude, therefore, that the magnitude of this concentration is dependent on the properties of the silicon before irradiation. The most likely impurity to be found in highly zone refined silicon in a concentration range of $3 \times 10^{13} cm^{-3}$ (Rockwell, Wacker) to $5 \times 10^{14} cm^{-3}$ (Topsil and T.I.) is oxygen. We, therefore, suggest that these acceptor defects are single or multiple defect-oxygen complexes, i.e., the oxygen impurity concentration is decorated as a result of the process of radiation damage and annealing to 550°C.

Figure 32 shows the recovery of resistivity and minority carrier lifetime on a Rockwell sample 1" dia x 1" long. The fluence for this irradiation was 50% of that necessary to produce type conversion. The annealing shows several unusual features which are found only in the Rockwell samples and which could possibly be related to the dislocation density. The resistivity between 200°C ans 800°C is multivalued. Shortly after removal from the annealing furnace and quenching to room temperature in trichloroethylene, the resistivity is a minimum but rises to the second higher value while storing the sample in the dark. Upon illumination from a tungsten light, the resistivity returns to its t = o value. The resistivity can be cycled any number of times. The reciprocal of the minority carrier lifetime follows the resistivity in general. Very heavy trapping is observed in the same region as the largest change in resistivity. This sample type-converts at about 800°C. It should also be noted that a plateau in the recovery around 300°C is similar to the Czochralski sample annealing seen previously.

In an attempt to determine if sample contamination is responsible for the unexpected type conversion, a series of isochronal anneals were performed in argon and a vacuum of 5×10^{-7} torr. The fluences for these irradiations were in the range of $\Phi = 0.36\ \Phi_c$ to $\Phi = 0.56\ \Phi_c$ where Φ_c is the fluence required for exact compensation. The results are shown in Figures 33 through 39. A comparison of a pair of vacuum and argon anneals are shown in Figures 40 and 41. It can be seen that all of these

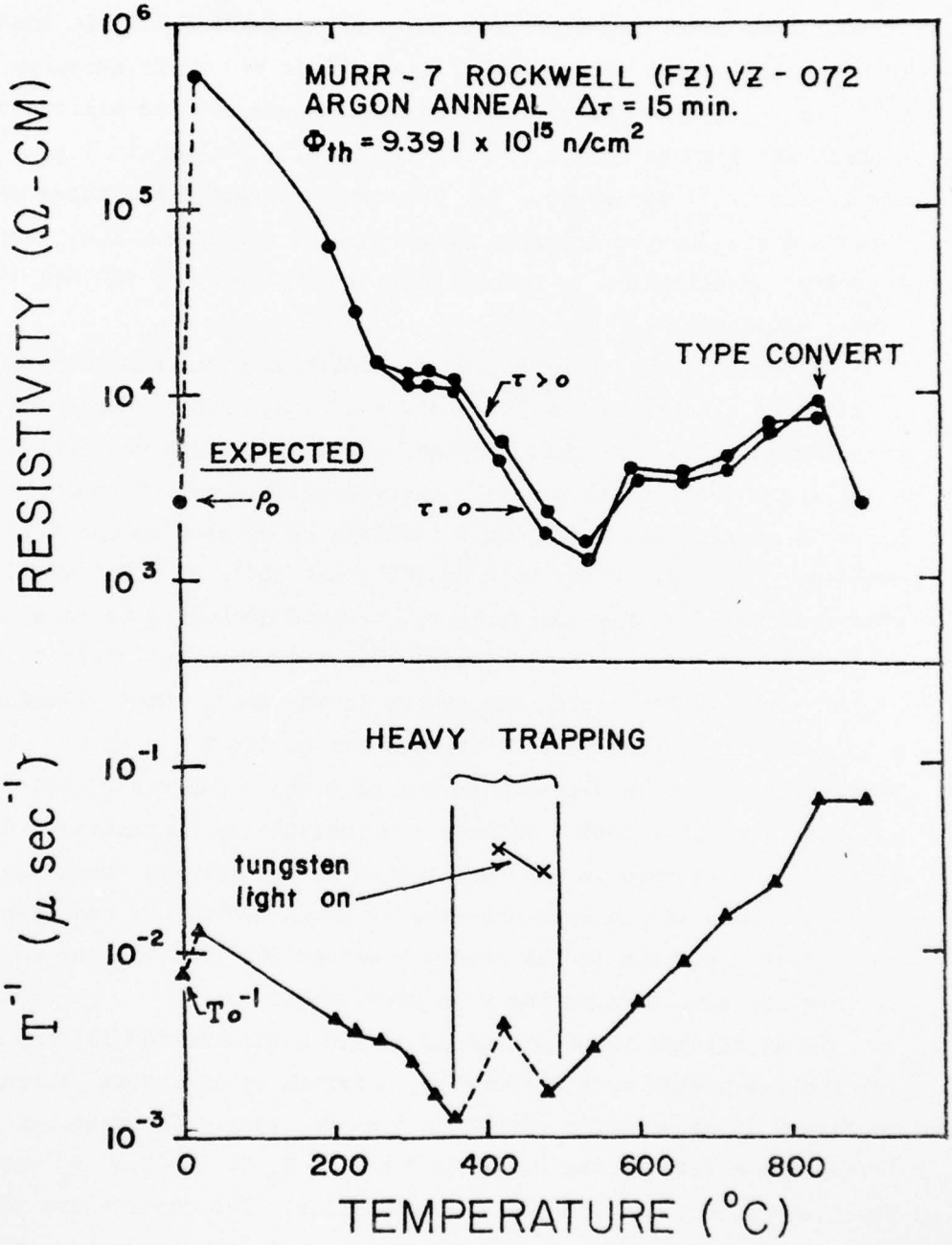


Figure 32. Isochronal annealing of resistivity and minority carrier lifetime of Rockwell float zone (argon anneal) - bulk sample.

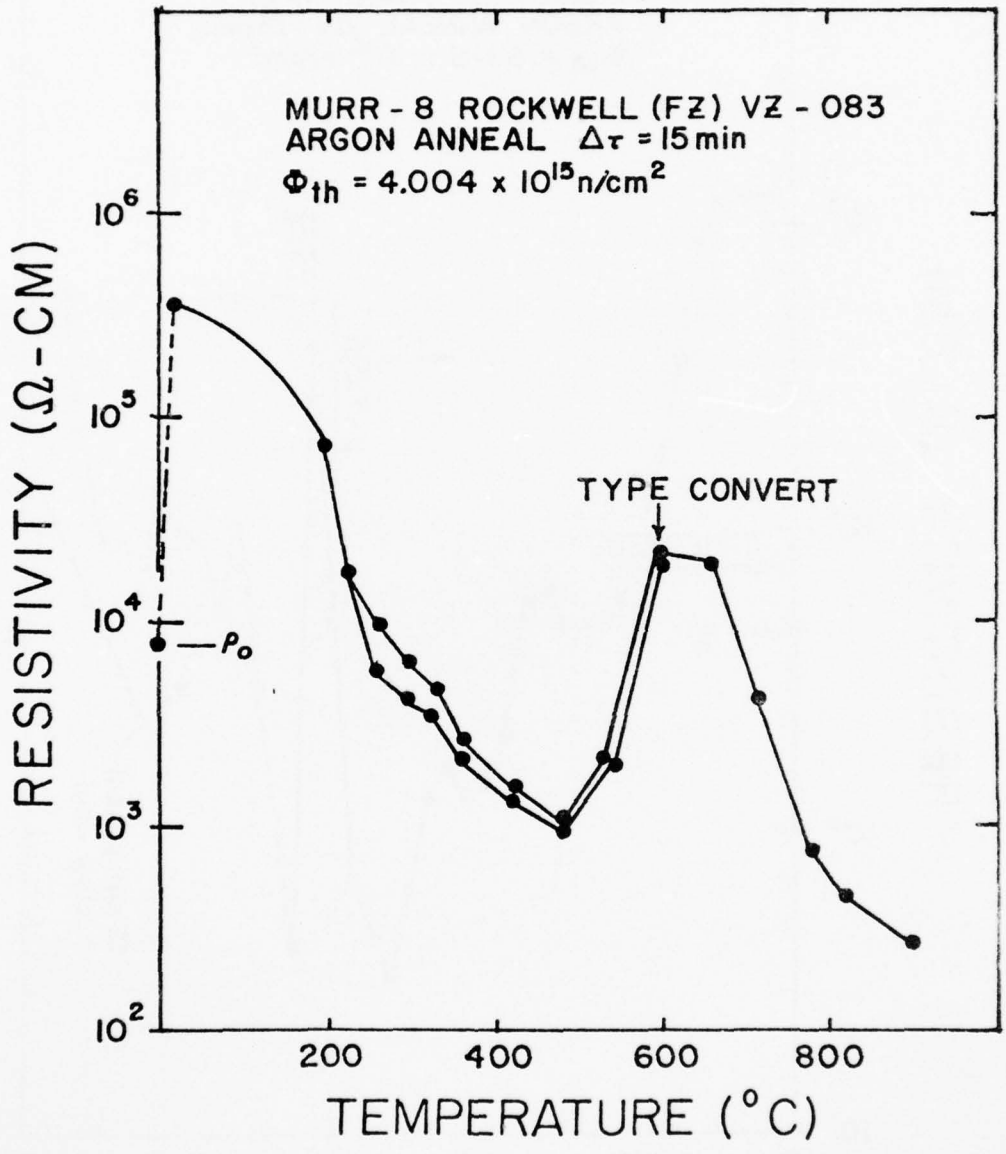


Figure 33. Argon isochronal anneal of resistivity of Rockwell float zone wafer.

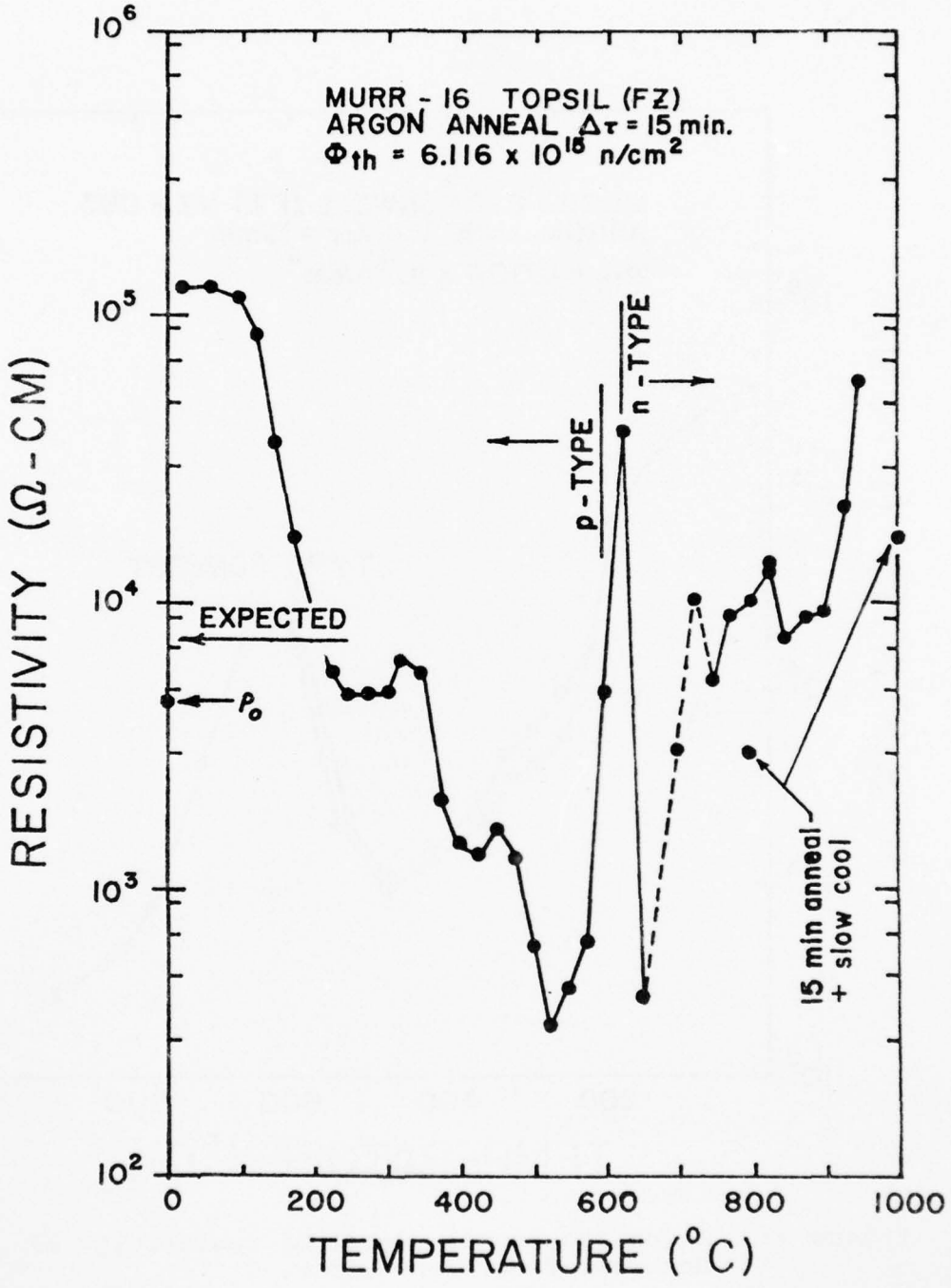


Figure 34. Argon isochronal anneal of Topsil wafer.

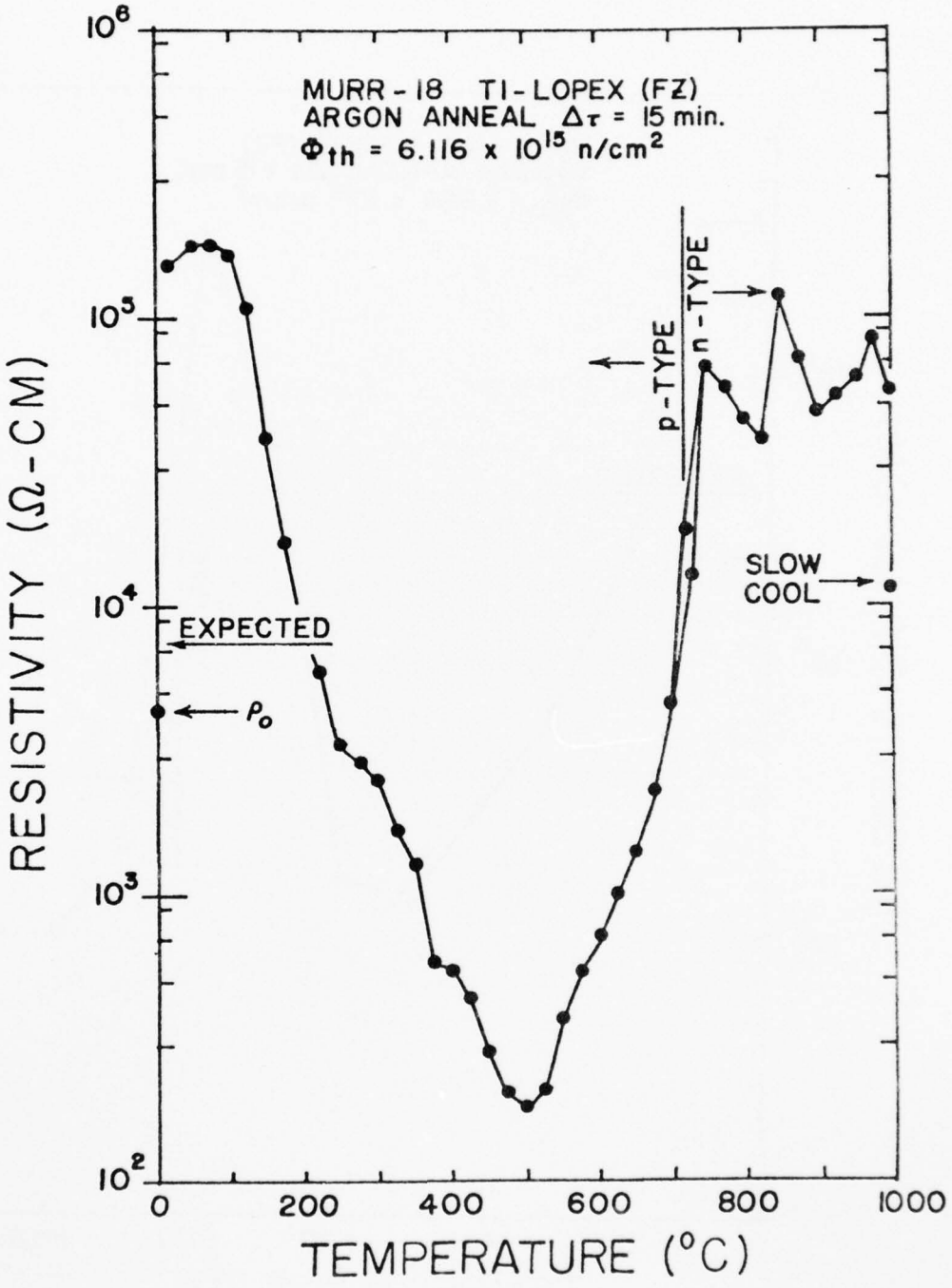


Figure 35. Argon isochronal anneal of T. I. Lopex wafer.

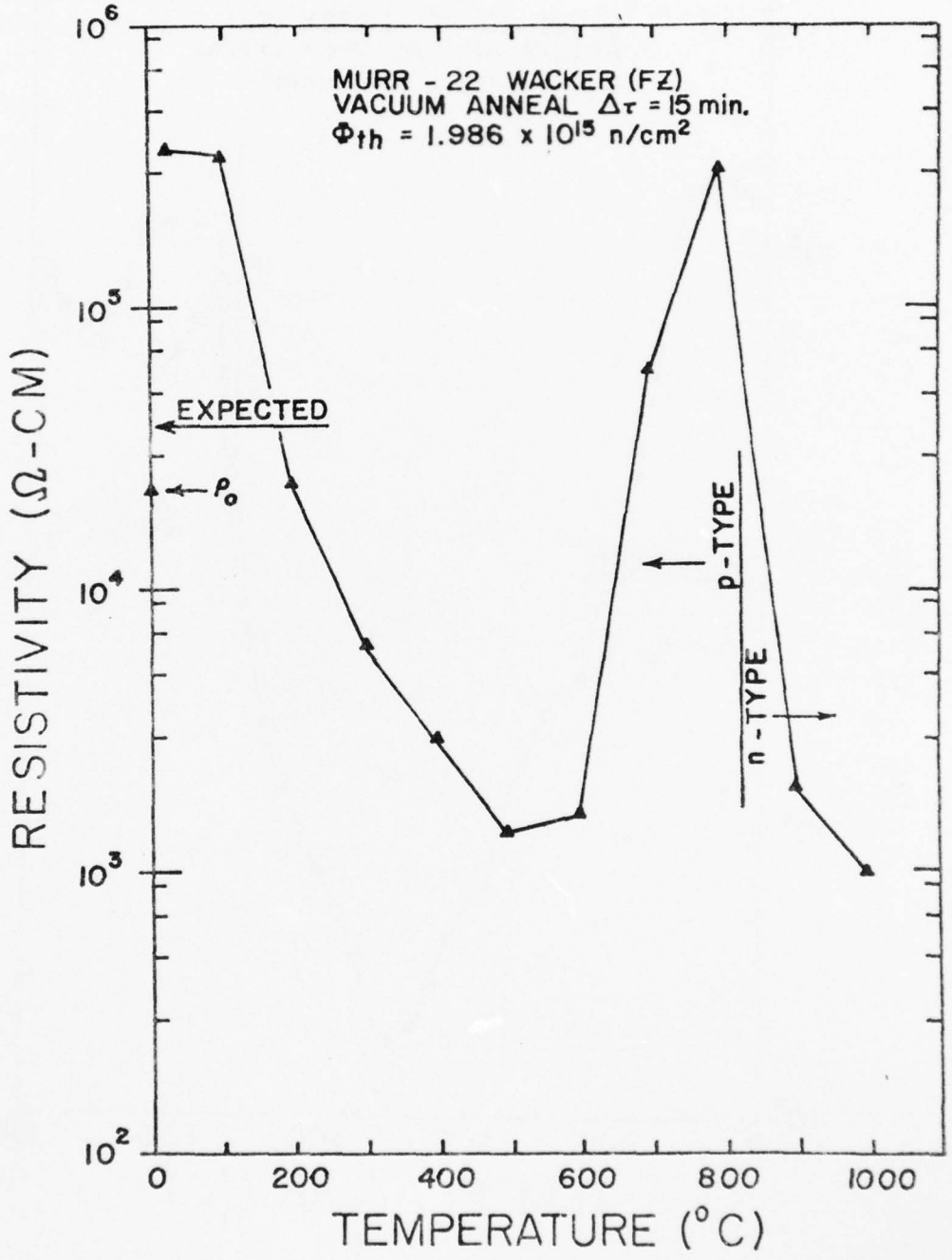


Figure 36. Vacuum isochronal anneal of Wacker wafer.

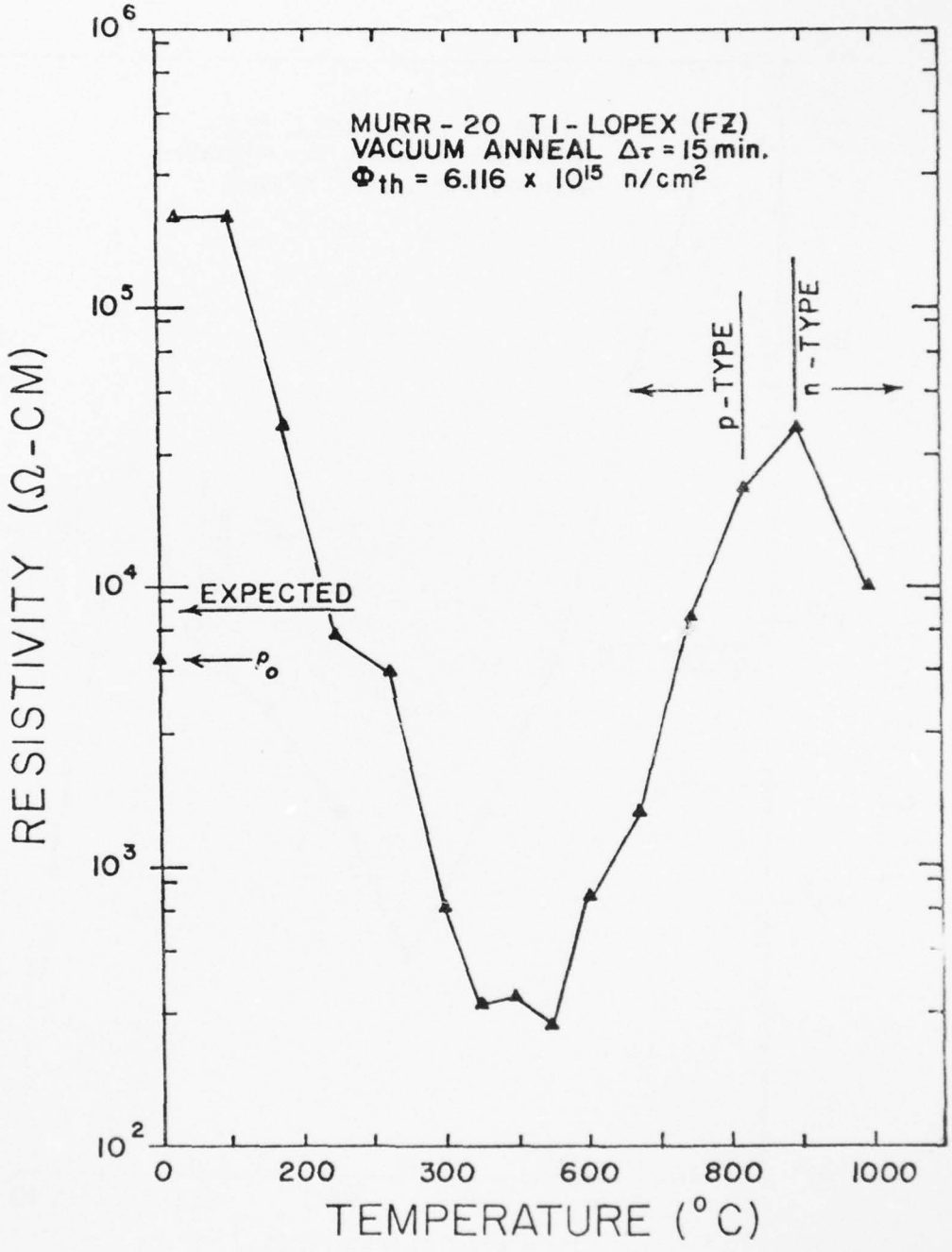
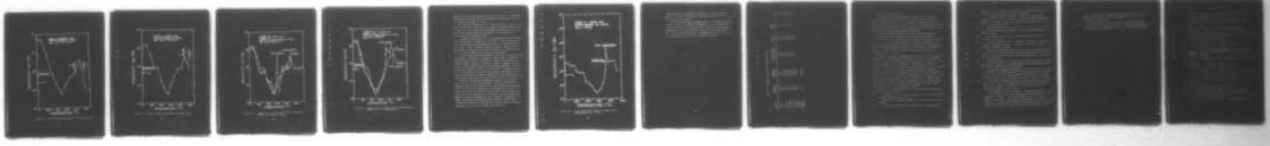


Figure 37. Vacuum isochronal anneal of T. I. - Lopex wafer.

AD-A038 471 MISSOURI UNIV-COLUMBIA RESEARCH REACTOR FACILITY F/G 20/12
SILICON DETECTOR COMPENSATION BY NUCLEAR TRANSMUTATION.(U)
FEB 77 J M MEESE F33615-76-C-5230
NL

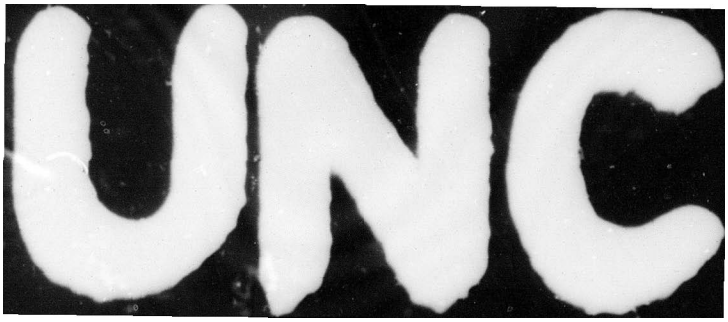
UNCLASSIFIED

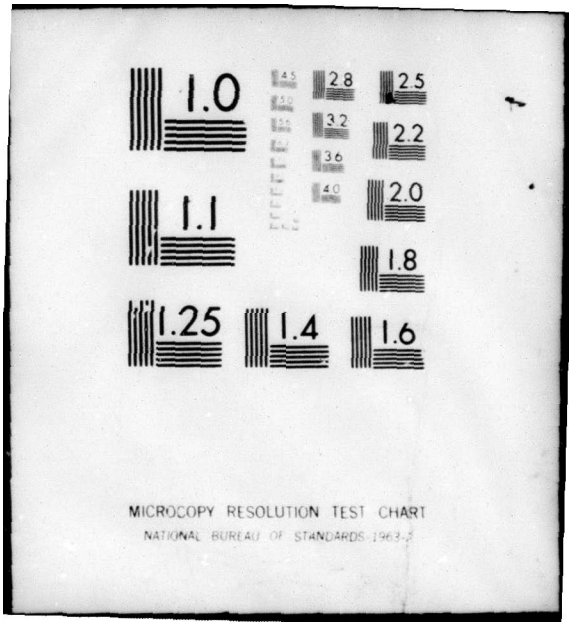
2 OF 2
AD
A038471



END

DATE
FILMED
5-77


UNC


1.0
1.1
1.25
1.4
1.6
1.8
2.0
2.2
2.5
2.8
3.2
3.6
4.0
4.5
5.0
5.6
MICROCOPY RESOLUTION TEST CHART
NATIONAL BUREAU OF STANDARDS-1963-A

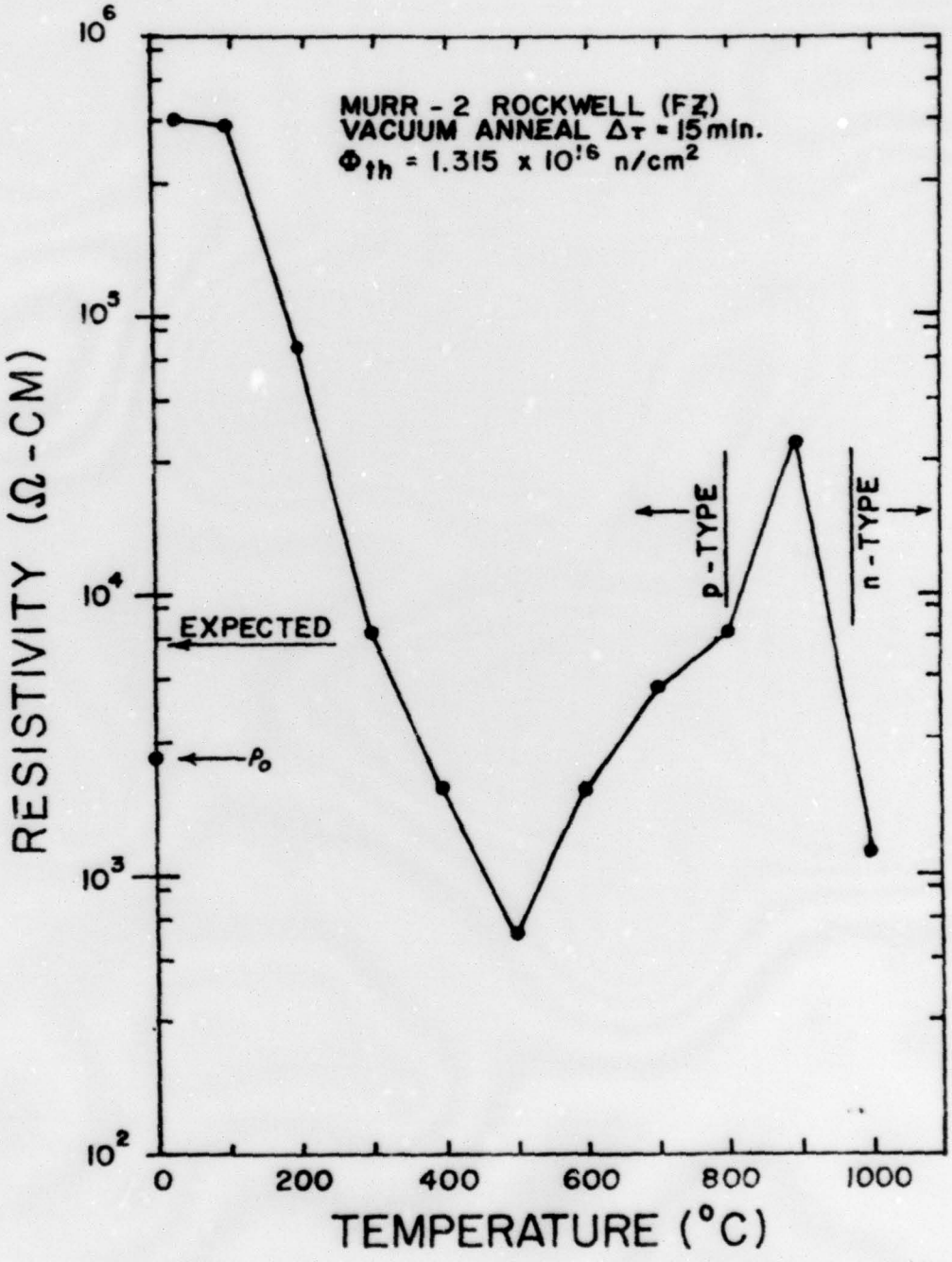


Figure 38. Vacuum isochronal anneal of Rockwell wafer.

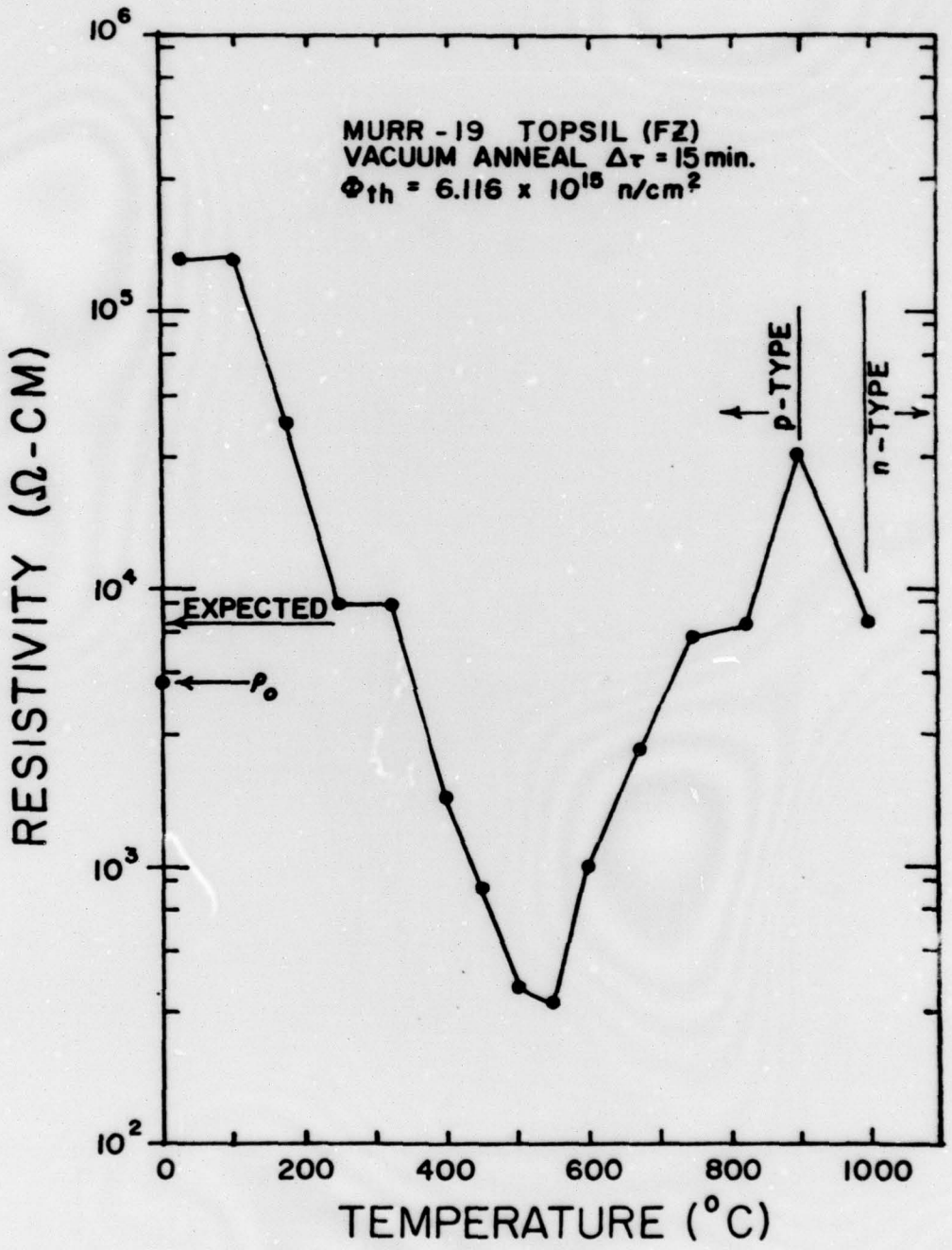


Figure 39. Vacuum isochronal anneal of Topsil wafer.

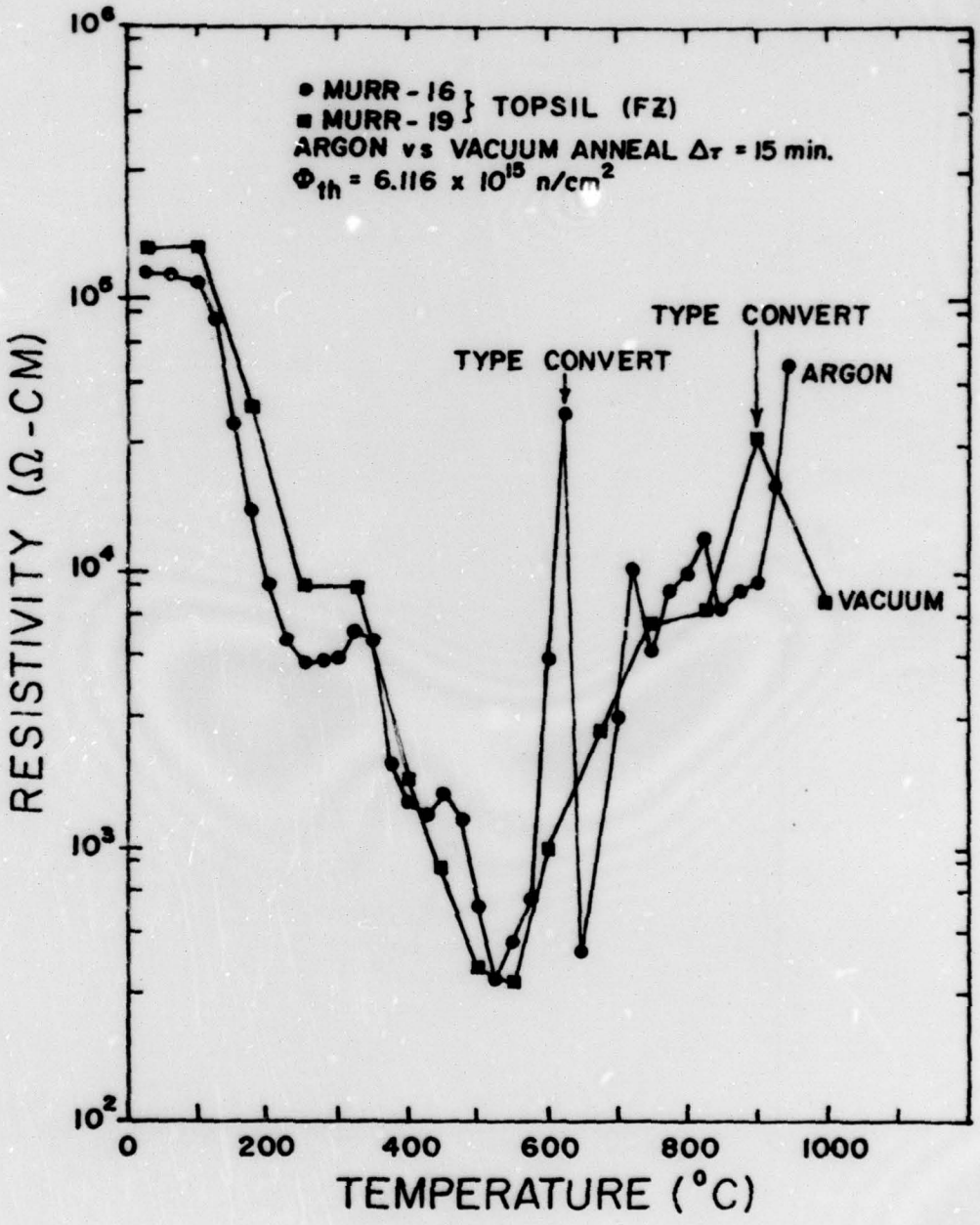


Figure 40. Comparison of vacuum and argon isochronal anneals for Topsil wafers.

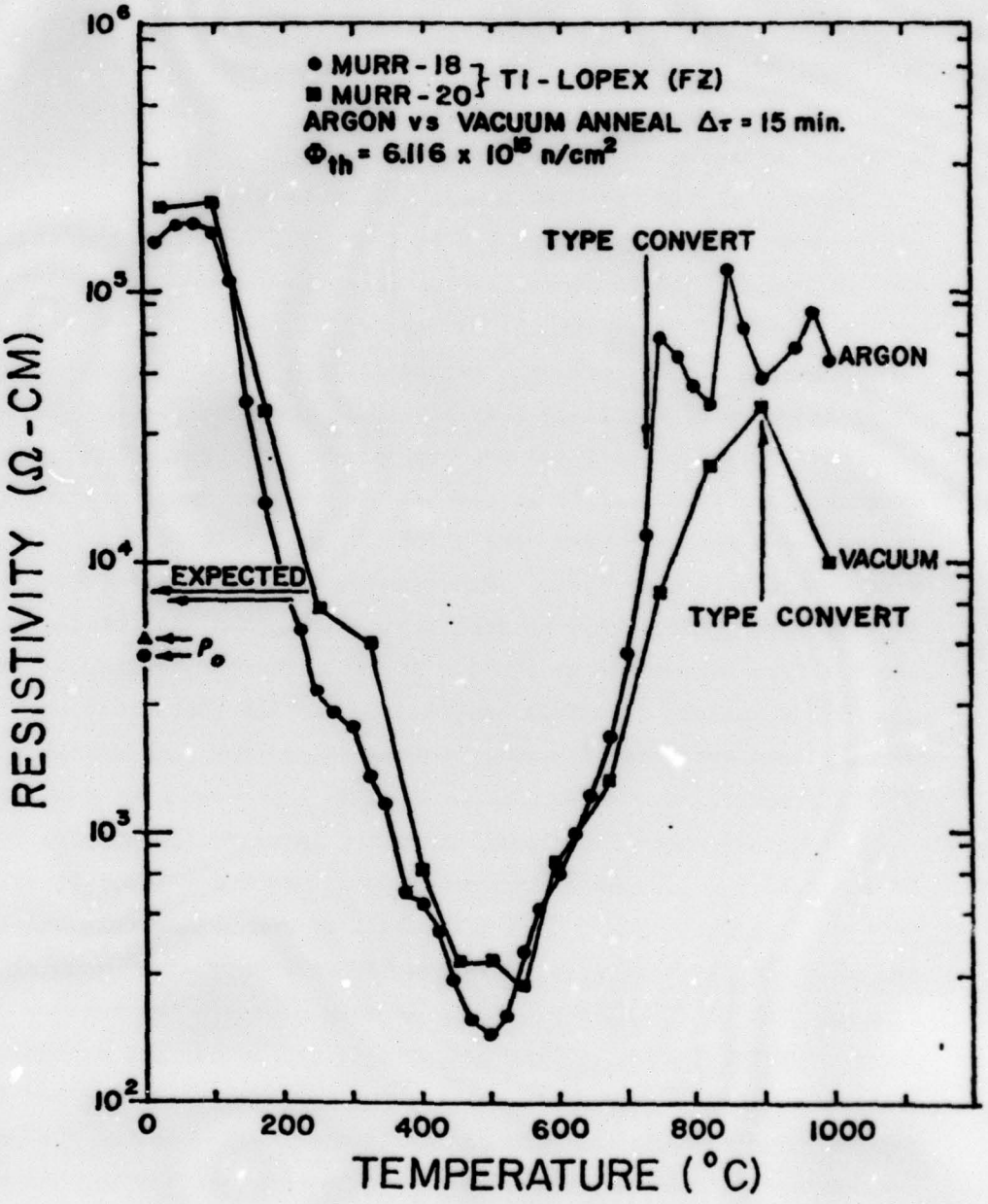


Figure 41. Comparison of vacuum and argon isochronal anneal of T. I. Lopex wafer.

samples type convert at temperatures between 600 and 900°C. The expected resistivities calculated from the concentration of phosphorus added is also shown on this series of figures.

Note that the minimum occurs at the same temperature in all of these anneals and that it is identical to the heavily irradiated samples shown in Figure 30. This minimum resistivity varies between 200 to 2000 Ω-cm in all these samples justify our estimates of the concentration of acceptor defects discussed previously.

An unusual feature seen in most of these anneals are the Czochralski like reverse anneals at temperatures below 600°C. These reverse anneals are most pronounced in those samples which show the lowest minimums at 550 to 600°C. This is evident in Figures 34 and 35. They are much less pronounced in the Rockwell and Wacker silicon which we suspect indicates about an order of magnitude less oxygen in these samples.

The final resistivities are completely uncontrollable for these light irradiations. Although it is tempting to suspect sample contamination during the anneal, we have been unable to detect any contamination by neutron activation analysis. Furthermore, Figure 41 suggests that there is very little difference between argon and vacuum annealing. Figure 34 shows a type conversion at 600°C. It is difficult to imagine diffusing 3×10^{12} atoms/cm^3 into this sample from surface contamination at 600°C. We have seen evidence of surface contamination for some anneals above 950°C, however, impurity diffusion is much more likely at this temperature.

Figure 42 shows isochronal annealing in argon for an irradiation of $\Phi = 1.02\ \Phi_c$, i.e. 2% overcompensation. The low resistivities at temperatures below 300°C were the result of remounting this sample with wax on a hot plate after irradiation for relapping after etching. It is seen that the final resistivity is very close to the expected value except for the last annealing point which may be surface contamination. Because of slight overcompensation, type conversion is expected in this sample. The etching and lapping may have removed a sodium surface contamination, however, the same procedure on other samples has made no improvement in our ability to prevent type conversion.

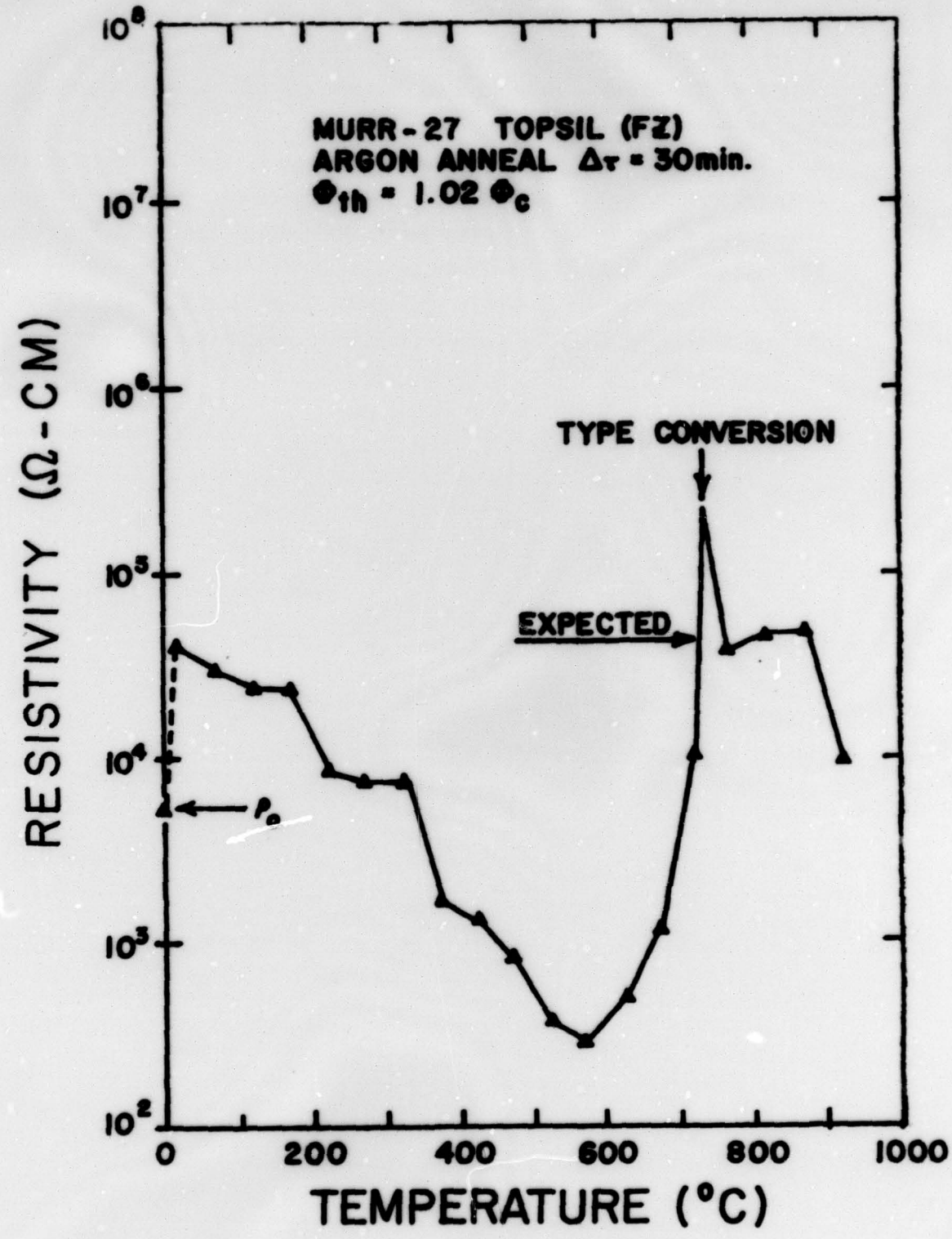


Figure 42. Argon isochronal anneal of Topsil Wafer irradiated to $\Phi = 1.02\Phi_c$.

Perhaps the additional phosphorus concentration, the extra radiation damage or the final charge type has suppressed the unknown donor which causes type conversion in some way.

In the following table, we summarize some of the prominent annealing features common to all samples investigated to date. The parameters listed below are the two "Czochralski-like" peaks, the first annealing temperature at which the resistivity equals the before irradiation resistivity, the minimum resistivity temperature and the ratio of the minimum resistivity to the before irradiation resistivity.

TABLE 13. Summary of Prominent Annealing Features

Sample	Temp. of 1st Peak	Temp. of 2nd Peak	Temp. at which $\rho_o = \rho$ anneal	Temp. of ρmin	$\frac{\rho min}{\rho_o}$	ρ_o
Topsil	330°C	450°C	360°C	520°C	.07	4000
T.I.	330°C	400°C	220°C	500°C	.04	4000
VZ-072-2	330°C	missing	430°C	540°C	.48	2500
VZ-083-4	320°C	missing	260°C	480°C	.13	8000
VZ-072-3	300°C	missing	280°C	500°C	.20	2500
Wacker	310°C?	missing	210°C	480°C	.07	20000
Monsanto Czoch.	310°C	420°C?				
Russian Czoch.	320°C	missing				

V. PROGRESS AND ACCOMPLISHMENTS

The object of this research program is to develop the technique of neutron transmutation doping in silicon to the point that the compensation ratio can be controlled to a very high precision. Significant success in this task will allow much better control over the boron compensation in silicon used for extrinsic IR detection. This in turn should provide a better control over detector detectivity and temperature dependence.

Although considerable unexpected difficulty has been encountered in controlling the impurity concentrations in silicon with any degree of certainty below 0.1 ppb, we feel that real progress has been made in achieving this goal. It has also become evident that a better understanding of the radiation damage, the oxygen concentration of the samples and the interaction between the defects and residual impurities in silicon before irradiation are needed in order to establish control over the entire doping process in concentrations below 0.1 ppb.

We believe that neutron transmutation doping has removed one of the major difficulties in achieving exact compensation in silicon, i.e., the precise control over phosphorus concentration which is improved by a factor of at least 50:1 over conventional doping techniques. Unfortunately, other residual impurity problems have been detected for the first time as a result of achieving this control. Because of these difficulties, we are behind schedule in compensating the boron in the presence of a very high Ga or In concentration. We feel, however, that a much better understanding of the limitations involved in this problem have resulted from our concerted effort on undoped material where impurity concentrations can be determined with a much higher precision. We also believe that we now have evidence to support the contention that compensation control in n-type material is possible.

The following is an abbreviated list of the significant accomplishments achieved during this program.

- Construction of the Bulk Pool Variable Flux Facility and demonstration of fluence reproducibility to $\pm$ 0.5%.
- Demonstration of doping concentration control to $\pm$ 1% for 100 Ω-cm material.
- No significant impurity problems detectable by neutron activation

analysis down to concentrations of better than 0.1 ppb with the exception of sodium in concentrations of 1 to 8 x 10^{13} atoms/cm^3.

- Pre-irradiation materials analysis of ρ, μ, and τ and activation analysis indicate that silicon from all sources are roughly compariable in quality. The largest exception is in minority carrier lifetime, τ, which is not as large as advertised.
- Theoretical analysis of the behavior on n, R_H, μ, and ρ versus fluence has been developed to evaluate results of neutron doping compensation of undoped materials.
- The theoretical cross section for phosphorus production has been verified to about $\pm$ 1%.
- Estimates have been made on the number of displacements as a function of fast to thermal neutron ratio. Importance of gamma recoil damage calculations have been verified.
- Several differences have been discovered between our annealing results and those found in the literature. These have been explained in terms of fast to thermal neutron ratio and carrier type immediately after irradiation but before annealing.
- Have related in core 1 Ω-cm radiation and subsequent annealing results discussed in literature to a radiation damage produced amorphous condition which alters annealing kinetics drastically.
- The activation energy and frequency factor for the electrical activation of transmutation produced phosphorus during annealing has been determined for the first time. This analysis suggests that vacancy-phosphorus pairs (E-centers) are related to the process of recovery of electrical activity.
- "Czochralski-like" annealing has been observed in lightly irradiated silicon ($\Phi \sim 0.5\ \Phi_C$) which suggests that clustering of radiation defects with residual oxygen is a problem which must be solved in float zone doped to concentrations below 0.1 ppb.
- The production of an acceptor defect in concentrations between 5 x 10^{13} to 5 x 10^{14} cm^{-3} by irradiation and annealing has been demonstrated to be independent of fluence. This strongly suggests that this acceptor is related to an intrinsic residual impurity concentration in the silicon before irradiation. We propose that oxygen, which has been decorated with defects to make it electrically active, is the source of these acceptors. This

result is exciting since it suggests that oxygen detection in silicon can easily be extended to lower than present day detection limits by several orders of magnitude.

- We have been able to produce a slightly overcompensated sample in at least one case where the ratio of donor to acceptor concentration is 1.02, i.e., a control of compensation ratio close to 2% of exact compensation.

REFERENCES

1. M. Tanenbaum and A.D. Mills, J. Electrochem. Soc. 108, 171 (1961).
2. M. L. Schultz, Infrared Phys. 4, 93 (1964).
3. J. Messier and J. M. Flores, J. Phys. Chem. Solid 24, 1539 (1963).
4. W. Shockley, "Electrons and Holes in Semiconductors", (Van Nostrand, N.Y. 1950), p. 217.
5. Keithley Instruments, Inc., 28775 Aurora Rd., Cleveland, Ohio 44139.
6. Hewlett-Packard, 1820 Embarcadero Rd., Palo Alto, Calif. 94303.
7. Alessi Industries, 3195 Airport Loop Drive, Bldg. C, Costa Mesa, Calif. 92626.
8. Signatone Corporation, 3012 Lawrence Expressway, Santa Clara, Calif. 95051.
9. L. B. Valdes, Proc. I.R.E. 42, 420 (1954).
10. A. Uhlir, Jr., Bell System Tech. J. 34, 105 (1955).
11. A.S.T.M. Standard F84-73, 1916 Race Street, Philadelphia, Pa. 19103.
12. L. J. Van der Pauw, Philips Res. Repts. 13, 1 (1958).
13. J. R. Ehrstein, ed., Semiconductor Measurement Technology, Spreading Resistance Symposium, NBS Special Publication 400-10, U.S. Dept. of Commerce, December 1974.
14. S. M. Rynkin, Photoelectric Effects in Semiconductors, (Consultants Bureau, N.Y., 1964).
15. General Radio, 300 Barker Ave., Concord, Mass. 01742
16. Tektronix, Inc., P.O. Box 500, Beaverton, Oregon 97077.
17. S. M. Rynkin, Ibid., p. 19-23. The equation (8.8) in this reference is incorrect. This expression should be written $V_m = V(\Delta\sigma/\sigma_o)[1 + (1 + \Delta\sigma/\sigma_o)]^2$. This error does not change the conclusions drastically, however, the correct expression has been used to obtain Eq. (20) in this report.
18. Air Products and Chemicals, Inc., Advanced Products Div., 1919 Vultee Street, Allentown, Pa. 18103.
19. Patrick M. Hemenger, Rev. Sci. Instrum., 44, 698 (1973).
20. Varian Instrument Division, 611 Hansen Way, Palo Alto, Calif. 94303.
21. G. H. Kinchin and R. S. Pease, Repts. Prog. in Phys. 18, 1(1955).
22. J. J. Loferski and P.P. Rappaport, Phys. Rev. 98, 1861 (1955); Ibid, 111, 432 (1958); J. Appl. Phys. 30, 1296(1959).
23. D. S. Billington and J. H. Crawford, Jr., Radiation Damage in Solids,

Princeton University Press, Princeton, N.J., (1961), Chapter 2.

24. J. J. Kalwaski and R. K. Thatcher, TREE Handbook, Defense Atomic Support Agency, DASA1420, p. E-26.
25. Ibid., p. E-28.
26. H. C. Schweinler, J. Appl. Phys. 30, 1125 (1959).
27. M. V. C[illegible]kichev and V. S. Vavilov, Sov. Phys. Semicond. 3, 1103 (1961).
28. V. A. Kharchenko and S. P. Solov'ev, Sov. Phys. Semicond. 5, 1437 (1972).
29. V. N. Mordkovich, S. P. Solov'ev, E. M. Temper, V. A. Kharchenko, Sov. Phys. Semicond. 8, 139 (1974).
30. J. W. Mayer, L. Eriksson and J. A. Davis, Ion Implantation in Semiconductors, Academic Press, New York (1970), p. 100.
31. Ibid, p. 7.
32. Ibid. p. 6.
33. Ibid. pp. 114-115.
34. G. D. Watkins and J. W. Corbitt, Phys. Rev. 134, A1359 (1964).
35. H. Saito, M. Hirata, and T. Horiuchi, J. Phys. Soc. Japan 18, Suppl III, 246 (1963).

